2013

# Challenges and Rewards of Single Crystal Flux Growth: Physical Properties of Structurally Related Ln-Ru-Al Intermetallics

Gregory Morrison
*Louisiana State University and Agricultural and Mechanical College*

# CHALLENGES AND REWARDS OF SINGLE CRYSTAL FLUX GROWTH: PHYSICAL PROPERTIES OF STRUCTURALLY RELATED Ln-Ru-Al INTERMETALLICS

A Dissertation

Submitted to the Graduate Faculty of
Louisiana State University and
Agricultural and Mechanical College
in partial fulfillment of the
requirements for the degree of
Doctor of Philosophy

in

The Department of Chemistry

by
Gregory Morrison
B.S., University at Buffalo, 2009
August 2013

## Acknowledgements

There have been many people whose support and guidance have been instrumental in my educational journey. First and foremost, I would like to thank my graduate advisor, Prof. Julia Y. Chan. Her constant attention and availability have helped me grow as a scientist and a writer.

As a graduate student I have had the opportunity to work with many great collaborators. Prof. David P. Young and his graduate student Dr. Neel Haldolaarachchige, Prof. Shane Stadler and his graduate student Joe Prestigiacomo, Prof Satoru Nakatsuji and his post-doc Dr. Kentaro Kuga, and Prof. Emilia Morosan and her graduate student Chih-Wei Chen have all proven invaluable resources in helping me learn condensed matter physics, a subject I had no exposure to prior to graduate school. I would also like to thank Prof. Jayne C. Garno and her graduate student Lauren E. Englade-Franklin. Our close collaboration over the past 4 years has greatly increased my breadth of knowledge as a scientist. Finally, I would like to thank Dr. Frank Fronczek and Dr. Gregory McCandless for all the help that they have provided me with X-ray crystallography.

Along with the great collaborators I have had, my graduate career has also been graced with wonderful group mates. I would especially like to acknowledge Dr. Brenton L. Drake for being my initial mentor in the group and Drs. Michael J. Kangas, William A. Phelan, and Devin C. Schmitt for their extensive help as mentors and in editing manuscripts.

While the above people were instrumental in my graduate career, none of it would have been possible without the many sources of funding that helped support my education. I am so grateful for the graduate fellowship provided by the Louisiana Board of Regents. Furthermore, the research I conducted was funded by the National Science Foundation through DMR-1063735 (J.Y.C.), DMR-1005764 (D.P.Y.), DMR-0545728 (S.S.), DMR-0847681 (E.M.), and CHE-0847291 (J.C.G.).

Finally, I would like to thank all the people whose mentoring and support lead me to become a graduate student. My advance placement chemistry teacher Mr. James Starr's passion for chemistry and chemistry demonstrations initially sparked my love for chemistry and my undergraduate advisor, Prof. Kenneth Takeuchi, provided me with a love for research. Lastly, I must thank my parents, Tim and Diane, and my brothers, Dan and Andrew, for instilling me with a love for learning and for the motivation and support they have given me throughout my educational career.

## Table of Contents

## Abstract

The availability of single crystals is vital for understanding the intrinsic properties of crystalline materials. The flux growth method is a versatile technique which may be used to grow single crystals. However, their synthesis can often be challenging, especially when a competing phase is very robust. Herein, we study the growth competition between structurally related compounds in the *Ln*-Ru-Al phase space. We demonstrate the benefits of single crystals and suggest methods to grow competing phases.

$CeRu_2Al_{10}$ has garnered interest due to its higher ordering temperate than expected from de Gennes scaling and its metal-to-insulator transition at the same temperature. Here, we report the magnetic and transport properties of three sets of compounds which are structurally related to $CeRu_2Al_{10}$: $LnRu_2Al_{10}$ (*Ln* = Pr, Gd, Yb), $CeRu_4(Al,Si)_{15.58}$, and $Ln_2Ru_3Al_{15}$ (*Ln* = Ce, Gd, Tb). We find that despite the structural similarities, none of these compound display properties similar to those of $CeRu_2Al_{10}$. Our extensive study of these structurally related compounds allows us to draw conclusions about the structure-property relationships in these systems.

## Chapter 1.[†] Introduction

Intermetallics exhibit many properties which can be useful for applications.[1.1] Aluminides have found use in high-temperature structural applications[1.2, 3] and silicides are used in electronics.[1.4] Rare earth intermetallics, such as $Nd_2Fe_{14}B$, are used as permanent magnets in devices such as hybrid cars and wind turbines.[1.5] Other intermetallics offer possible energy applications such as thermoelectrics,[1.6, 7] magnetocalorics,[1.8] and superconductivity.[1.9, 10] On the nanoscale, intermetallics can potentially be used in magnetic data storage devices,[1.11] for biomedical applications,[1.12] and as catalysts.[1.13]

One class of materials which are of particular interest are strongly correlated electron systems, systems whose properties arise as the result of electron-electron interactions.[1.14-16] These materials exhibit many properties which are both useful for current applications as well as offer potential for future applications. RKKY interactions, through which the conduction electrons couple magnetic moments,[1.17-19] can lead to long range magnetic ordering. The Kondo effect, a mechanism in which the conduction electrons screen the magnetic moments, competes with the RKKY interaction and can lead to heavy fermion behavior, where the conduction electrons appear to have an enhanced mass.[1.20] Additionally, electron-electron interactions can give rise to metal-to-insulator transitions where a small temperature change can result in an orders of magnitude change in the resistivity.[1.21] Perhaps the epitome of strongly correlated systems, is high-$T_c$ superconductivity, where electron-electron interactions within pairs of electrons reduces the resistivity to zero.[1.22]

[†]Partially reproduced with permission from Morrison, G. W.; Menard, M. C.; Treadwell, L. J.; Haldolaarachchige, N.; Kendrick, K. C.; Young, D. P.; Chan, J. Y., *Philos. Mag.* **2012,** *92*, 2524-2540. Copyright 2012 Taylor & Francis.
http://www.tandfonline.com/doi/full/10.1080/14786435.2012.669063
and Morrison, G.; Haldolaarachchige, N.; Chen, C.-W.; Young, D. P.; Morosan, E.; Chan, J. Y., *Inorg. Chem.* **2013,** *52*, 3198-3206. Copyright 2013 American Chemical Society.

Despite the technological demand for crystalline materials, the United States' solid state community is grappling with a shortage of high quality crystalline samples for physical property studies.[1.23] The synthesis of crystalline material within the US has fallen behind the efforts in other countries. In response to this, the National Academy of Sciences released a report highlighting the need for increased growth of crystalline materials. The report laid out three grand challenges: the synthesis of crystalline materials for energy applications, the synthesis of crystalline materials for new technologies, and the design of crystalline materials through the use of computational methods.[1.24]

The research described within this document is in line with the first two grand challenges. Two main methods are used in selecting materials to be studied. First, structure types with specific motifs can be targeted. For example, compounds with triangular arrangements of lanthanides or 3rd row transition metals, such as kagome lattices, may exhibit magnetic frustration.[1.25] Likewise, layered materials sometimes show large magnetoresistance.[1.26] In Chapters 2-6 of this document, compounds of three structure types will be studied due to their similarities to $CeRu_2Al_{10}$, whose properties will be discussed in Chapter 2. Second, specific structure types which display desired properties can be targeted. By substituting one element with another, these physical properties can be tuned. In Chapter 7 of this document, a doping studies of $YbAl_{1-x}Fe_xB_4$ will be discussed. Using these two techniques, structurally similar materials can be compared in order to reveal trends such as how structural motifs, metal coordination, or valence electron concentrations are correlated to desired behavior.

When studying new materials, single crystals offer many advantages over polycrystalline materials. Single crystals allow for structure determination using single crystal X-ray diffraction (XRD). Furthermore, single crystals allow for the measurement of the intrinsic properties of a

material. In polycrystalline samples, the properties can be affected by grain boundaries between crystallites and by impurities trapped in the grain boundaries. Finally, single crystals allow for the measurement of anisotropic properties, properties down a specific orientation of a crystal. Anisotropic properties are useful for elucidating a compounds magnetic structure and for studying crystalline electric field effects, which will be discussed at the end of this chapter. For the above reasons, single crystals are initially targeted for all studies in this document. Only when single crystals cannot be obtained are polycrystalline samples used.

One challenge to crystal growth is obtaining a single phase within a growth, as multiple phases often grow in a single batch. For this reason, investigation of the competition between phases by systematically varying the reactant ratio and heating profile is required in order to determine the optimal growth conditions of one phase with respect to another. This is especially important when one compound in a phase space is considerably more stable than the others. In such a case, the growth of the other phases can be very difficult. Several examples of the competition between the growth of two compounds can be found in the *Ln*:Ru:Al and *Ln*:Ru:Al:Si (*Ln* = lanthanide) phase spaces. The competition between the growth of $CeRu_4(Al,Si)_{15.58}$ and $Ru_{23}(Al,Si)_{97}$ will be discussed in Chapter 3 and the competition between the growth of $Ce_2Ru_3Al_{15}$ and $CeRu_2Al_{10}$ will be discussed in Chapter 4.

Many techniques are available for the growth of crystalline materials, and each technique offers certain advantages and disadvantages. Often, phase pure compounds tend to prefer a specific growth technique. In this document, three different solid state synthesis techniques, flux growth, radio frequency induction heating, and arc melting, will be used in attempt to grow physical property measurement quality samples.

The first technique, flux growth, uses a low melting metal as a solvent, or flux, in order to dissolve metals with higher melting points. The reactant metals are heated in a high temperature muffle furnace which allows for fine-tuned temperature control. Typically, flux growth reactions are quickly heated (~100 °C/h) to a high temperature (1000-1200 °C) at which the reaction is dwelled for ~24 h in order to ensure homogeneity. The reaction is then slowed cooled (1-15 °C/h) to a temperature above the melting point of the flux. By inverting and centrifuging the sample, the excess flux can be spun off. The slow cooling often results in the growth of single crystals. Furthermore, the high degree of control over reaction conditions can allow for the growth of congruently melting, incongruently melting, and even metastable phases. However, in order to prevent the reactant metals from oxidizing, flux growth reactions are typically sealed in an evacuated fused-silica tube. As fused-silica begins to become molten at ~1250 °C, the maximum temperature available to flux growth is about 1250 °C.

A second technique, radio frequency (RF) induction heating, applies an alternating current to a coil, creating an alternating magnetic field. An alumina crucible wrapped with tantalum foil is placed in an argon environment in the center of the coil. The magnetic field creates eddy currents in the tantalum foil which leads to resistive heating of the foil and, in turn, heats the crucible. Because the sample is in an inert environment, higher temperatures can be reached than in the flux method. Furthermore, by changing the amplitude of the applied current or partially raising the sample out of the coil, the temperature can be controlled. However, because an alumina crucible is used, the maximum temperature is limited by the melting point of alumina, 2053 °C.[1.27]

A third technique, arc melting, uses an arc of electricity in order to melt the reactant metals under an inert atmosphere. This technique heats the reaction to ~3000-4000 °C.

However, arc melting provides little temperature control, and the rapid heating and cooling involved results in a polycrystalline sample. Furthermore, in order to obtain phase pure material, arc melted samples typically have to be annealed at lower temperatures (500 - 1200 °C) for extended time periods (often 1 - 4 weeks).

During the course of this dissertation, several physical phenomena will be mentioned. One reoccurring phenomena, crystalline electric field (CEF) effects, will be discussed in detail here. CEF effects occur when a non-spherical electron density surrounding a lanthanide breaks the degeneracy of the *f*-orbitals. The way in which these orbitals are split is dependent on the point symmetry of the lanthanide site. CEFs can strongly affect the magnetic properties of crystalline materials.[1.28]

One effect of crystalline electric fields which is most common in Pr, Tb and Tm containing compounds is the existence of a non-magnetic ground state. In Pr compounds, CEF splitting can lead to two possible non-magnetic ground states, a singlet ground state and a non-magnetic doublet ground state. For example, under cubic point symmetry, the *f*-electron multiplet of a $Pr^{3+}$ ion is split into a singlet, a non-magnetic doublet and two triplets.[1.29] Which of these states is the ground state depends on the electrostatic interaction between the *f*-electrons and the aspherical electron density surrounding the lanthanide.[1.28] In systems with a non-magnetic ground state, the system is magnetic at temperatures sufficiently above the splitting energy between the ground state and first excited state. At these temperatures, both states are equally populated. When the thermal energy becomes too small to excite electrons from the ground state, the system becomes non-magnetic. This is characterized by the magnetic susceptibility becoming nearly temperature independent, as is observed in $PrTi_2Al_{20}$[1.30] and $PrOs_2Al_{10}$.[1.31]

A second effect of crystalline electric fields is anisotropic magnetism. The CEF can dominate over the applied field and polarize the magnetic moments in one direction.[1.32] This can lead to anisotropic magnetic susceptibility, such as with $HoNi_2B_2C$[1.33] and $Tb_{30}Ru_4Sn_{31}$.[1.34] This anisotropy can be used to calculate the CEF splitting energies, as was done for $CeRu_2Al_{10}$.[1.35]

One final effect that crystalline electric fields can have on magnetic properties, which will be discussed, here is their effect on the Weiss temperature. Along with leading to anisotropic susceptibility, the pulling of the magnetic moments by the CEF contributes to $\theta_W$. The CEF contribution to the Weiss temperature, $\theta_{CF}$, can be determined by doping a non-magnetic lanthanide onto the rare earth site as this doping has little effect on $\theta_{CF}$ but reduces the portion of the Weiss temperature due to the exchange interaction.[1.32] Such studies have been performed on $Nd_{2-x}La_xTi_2O_7$[1.32] and $Ho_{1-x}Lu_xNi_2B_2C$[1.33]. Not only can CEF affect the Weiss temperature, they can also enhance the ordering temperature. When the CEF pulls the magnetic moment in the same direction as the exchange interaction, the ordering temperature can be increased.[1.36] As the *f*-electrons in Gd are spherically symmetric, there are no CEF effects on Gd ions. As a result, when the CEF enhances the ordering temperature, a deviation from the expected RKKY ordering temperatures is observed. An example of this deviation is observed in the $LnRh_4B_4$ system.[1.36]

The synthesis of large single crystals focuses on crystal growth while minimizing nucleation. On the other end of the size scale, the synthesis of nanoparticles focuses on maximizing nucleation while keeping growth low. Like with the synthesis of bulk crystals, the synthesis of nanoparticles offers many challenges. When considering large single crystals, the stability of a phase is almost entirely dependent on the energetics of the bulk. However, for nanoparticles, the surface energy of the particle becomes important due to the large percentage of

atoms on the surface of a nanoparticle.[1.37] For example, nanoparticles which are smaller than 10 nanometers have over 50% of their atoms on the surface.[1.38] One direct results of this is the importance of surfactants on nanoparticle morphology. The use of surfactants allows for the stabilization of certain faces over others, thereby controlling nanoparticles morphology.[1.39] For example, CTAB preferentially binds to the (100) face of gold allowing for the growth of nanorods.[1.40] Likewise, the addition of amine surfactants to PbTe nanoparticles reactions stabilizes Pb rich (111) faces leading to the formation of cuboctahedra or octahedra instead of cubes, depending on the Pb:Te ratio.[1.41] A second result of the large surface area to volume ratio of nanoparticles is Oswald ripening. Smaller nanoparticles have a higher chemical potential than larger nanoparticles and as a result, dissolve at a faster rate. For this reason, over time, when monomer concentrations are low, smaller nanoparticles will become smaller and larger nanoparticles will become larger, thereby increasing the size distribution of the nanoparticles.[1.37] A similar effect is the aggregation of nanoparticles upon heating.[1.42]

## 1.1 References


1.1. Stoloff, N. S.; Liu, C. T.; Deevi, S. C., *Intermetallics* **2000,** *8*, 1313-1320.

1.2. Deevi, S. C.; Sikka, V. K., *Intermetallics* **1996,** *4*, 357-375.

1.3. Sauthoff, G., *Intermetallics* **2000,** *8*, 1101-1109.

1.4. Reader, A. H.; Ommen, A. H. v.; Weijs, P. J. W.; Wolters, R. A. M.; Oostra, D. J., *Rep. Prog. Phys.* **1993,** *56*, 1397.

1.5. Kramer, D., *Phys. Today* **2010,** *63*, 22-24.

1.6. Riffat, S. B.; Ma, X., *Appl. Therm. Eng.* **2003,** *23*, 913-935.

1.7. Vineis, C. J.; Shakouri, A.; Majumdar, A.; Kanatzidis, M. G., *Adv. Mater.* **2010,** *22*, 3970-3980.

1.8. Pecharsky, V. K.; Gschneidner Jr, K. A., *J. Magn. Magn. Mater.* **1999,** *200*, 44-56.

1.9. Rotter, M.; Tegel, M.; Johrendt, D., *Phys. Rev. Lett.* **2008,** *101*, 107006.

1.10. Nagamatsu, J.; Nakagawa, N.; Muranaka, T.; Zenitani, Y.; Akimitsu, J., *Nature* **2001,** *410*, 63-64.

1.11. Nguyen, H. L.; Howard, L. E. M.; Giblin, S. R.; Tanner, B. K.; Terry, I.; Hughes, A. K.; Ross, I. M.; Serres, A.; Burckstummer, H.; Evans, J. S. O., *J. Mater. Chem.* **2005,** *15*, 5136-5143.

1.12. Tran, N.; Webster, T. J., *J. Mater. Chem.* **2010,** *20*, 8760-8767.

1.13. Ghosh, T.; Leonard, B. M.; Zhou, Q.; DiSalvo, F. J., *Chem. Mater.* **2010,** *22*, 2190-2202.

1.14. Phelan, W. A.; Menard, M. C.; Kangas, M. J.; McCandless, G. T.; Drake, B. L.; Chan, J. Y., *Chem. Mater.* **2012,** *24*, 409-420.

1.15. Thomas, E. L.; Millican, J. N.; Okudzeto, E. K.; Chan, J. Y., *Comments Inorg. Chem.* **2006,** *27*, 1-39.

1.16. Morosan, E.; Natelson, D.; Nevidomskyy, A. H.; Si, Q., *Adv. Mater.* **2012,** *24*, 4896-4923.

1.17. Ruderman, M. A.; Kittel, C., *Phys. Rev.* **1954,** *96*, 99-102.

1.18. Kasuya, T., *Prog. Theor. Phys.* **1956,** *16*, 45-57.

1.19. Yosida, K., *Phys. Rev.* **1957,** *106*, 893-898.

1.20. Edelstein, A. S., *J. Magn. Magn. Mater.* **2003,** *256*, 430-448.

1.21. Imada, M.; Fujimori, A.; Tokura, Y., *Rev. Mod. Phys.* **1998,** *70*, 1039-1263.

1.22. Capone, M.; Fabrizio, M.; Castellani, C.; Tosatti, E., *Science* **2002,** *296*, 2364-2366.

1.23. Feder, T., *Phys. Today* **2007,** *60*, 26-28.

1.24. *Frontiers in crystalline matter: From discovery to technology*. The National Academies Press: 2009.

1.25. Moessner, R., *Ca. J. Phys.* **2001,** *79*, 1283-1294.

1.26. Argyriou, D. N.; Mitchell, J. F.; Radaelli, P. G.; Bordallo, H. N.; Cox, D. E.; Medarde, M.; Jorgensen, J. D., *Phys. Rev. B* **1999,** *59*, 8695-8702.

1.27. Lide, D. R., *CRC Handbook of Chemistry and Physics*. 86 ed.; Taylor & Francis: New York, 2005.

1.28. Luong, N. H., *Physica B* **2002,** *319*, 90-104.

1.29. Guertin, R. P., Pressure induced changes in the magnetism of crystal field split systems. In *Crystalline electric field effects in f-electron magnetism*, Guertin, R. P.; Suski, W.; Zołnierek, Z., Eds. Plenum Press: New York, 1982; pp 25-39.

1.30. Sakai, A.; Nakatsuji, S., *J. Phys. Soc. Jpn.* **2011,** *80*, 063701.

1.31. Muro, Y.; Kajino, J.; Onimaru, T.; Takabatake, T., *J. Phys. Soc. Jpn.* **2011,** *80*, SA021.

1.32. Xing, H.; Long, G.; Guo, H.; Zou, Y.; Feng, C.; Cao, G.; Zeng, H.; Xu, Z.-A., *J. Phys. Condens. Matter* **2011,** *23*, 216005.

1.33. Cho, B. K.; Harmon, B. N.; Johnston, D. C.; Canfield, P. C., *Phys. Rev. B* **1996,** *53*, 2217-2220.

1.34. Prestigiacomo, J.; Schmitt, D. C.; Chan, J. Y.; Young, D. P.; Adams, P. W., *In Preparation* **2013**.

1.35. Hanzawa, K., *J. Phys. Soc. Jpn.* **2011,** *80*, 023707.

1.36. MacKay, H. B.; Woolf, L. D.; Maple, M. B.; Johnston, D. C., *J. Low Temp. Phys.* **1980,** *41*, 639-651.

1.37. Park, J.; Joo, J.; Kwon, S. G.; Jang, Y.; Hyeon, T., *Angew. Chem. Int. Ed.* **2007,** *46*, 4630-4660.

1.38. Herrera-Becerra, R.; Zorrilla, C.; Ascencio, J. A., *J. Phys. Chem. C* **2007,** *111*, 16147-16153.

1.39. Tao, A. R.; Habas, S.; Yang, P., *Small* **2008,** *4*, 310-325.

1.40. Murphy, C. J.; Sau, T. K.; Gole, A. M.; Orendorff, C. J.; Gao, J.; Gou, L.; Hunyadi, S. E.; Li, T., *J. Phys. Chem. B* **2005,** *109*, 13857-13870.

1.41. Mokari, T.; Zhang, M.; Yang, P., *J. Am. Chem. Soc.* **2007,** *129*, 9864-9865.

1.42. Li, D.; Kaner, R. B., *J. Am. Chem. Soc.* **2005,** *128*, 968-975.

## Chapter 2.† Magnetic and Transport Properties of Single Crystal $LnRu_2Al_{10}$ (*Ln* = Pr, Gd, Yb)

### 2.1 Introduction

As part of our effort to grow single crystals of *Ln*-M-Al (M = Transition metal) systems to study the interplay of magnetism in rare earth and transition metal sublattices,[2.1] we have chosen to work with compounds of the Fe triad. This effort is motivated by our interests in understanding the mechanism of magnetism, especially the competition between itinerant and localized moments. We have previously reported a series of lanthanide analogues of $Ln_4FeGa_{12}$ where the magnetic rare earth compounds order with magnetism due to the rare earth ions. However, the nonmagnetic rare earth analogue $Y_4FeGa_{12}$ seems to exhibit itinerant magnetism.[2.2] A competition between itinerant and localized magnetism has also been observed in $(La_{1-x}Y_x)Mn_4Al_8$ ($0 \leq x \leq 1$) of the $CeMn_4Al_8$ structure type, an ordered derivative of $ThMn_{12}$ type. In these compounds, the spin pseudogap is continuously tunable between 200 K and 500 K by varying *x*.[2.3]

Compounds consisting of *Ln*-M-Al (*Ln* = Lanthanide; M = Fe, Ru, Os) can adopt a wide variety of structure types including $YbFe_2Al_{10}$ [2.4], $CeRu_{3-x}Al_{10+x}$,[2.5] $Ce_2Ru_3Al_{15}$,[2.6] $Gd_3Ru_4Al_{12}$,[2.7] CeRuAl,[2.8] $La_{11}Ru_2Al_6$,[2.9] $La_5Ru_3Al_2$,[2.10] and $Gd_4RhIn$.[2.11] These structure types include many structural motifs, some of which can be observed in more than one structure type. The $YbFe_2Al_{10}$ structure type, a substitutional and stacking variant of the $ThMn_{12}$ structure type [2.4] is adopted by $LnFe_2Al_{10}$ (*Ln* = Y, La-Nd, Sm, Gd-Lu), $LnRu_2Al_{10}$ (*Ln* = Y, La-Nd, Sm, Gd, Tb, Ho-Yb),[2.12] $LnOs_2Al_{10}$ (*Ln* = La-Nd, Sm, Gd),[2.12, 13] and $UM_2Al_{10}$ (M = Fe, Ru, Os).[2.14-16] Despite the pervasiveness of the $YbFe_2Al_{10}$ structure type for M = Fe, Ru, Os, it has only been reported for the Fe triad. $LnM_2Al_{10}$ (*Ln* = Y, La-Nd, Sm, Gd-Dy, Yb; M = Mn, Re) instead prefers to adopt

the $ThMn_{12}$ or $CaCr_2Al_{10}$ structure types[2.17, 18] and *Ln*-M-Al (M = Co, Rh, Ir) does not adopt a $LnM_2Al_{10}$ structure.

Several $LnM_2Al_{10}$ (*Ln* = Lanthanide, M = Fe, Ru, Os) compounds of the $YbFe_2Al_{10}$ structure type[2.4] have been extensively studied due to the properties of some of the member compounds. The Ce, Pr, Nd and Yb analogues of $LnFe_2Al_{10}$ were found to be paramagnets with the Ce and Yb analogue containing mixed valent Ce and Yb, respectively. The Sm – Tm analogues are antiferromagnets with $GdFe_2Al_{10}$ ordering at the highest temperature, 15(3) K.[2.12] Notably, $YFe_2Al_{10}$ was found to lie near a quantum critical point where the Fe atoms carry a magnetic moment of 0.45 $\mu_B$ and the quantum criticality was attributed to the magnetic ordering of the Fe moments tuned to T = 0 K by an external magnetic field. Furthermore, the resistivity displays a Kondo upturn near 20 K.[2.19]

$CeRu_2Al_{10}$ is a heavy fermion compound, $\gamma$ = 246 mJ/($K^2$mol), which shows a magnetic transition at 27.3 K, higher than the 16.5 K antiferromagnetic ordering for $GdRu_2Al_{10}$.[2.20] This transition is characterized by a sharp decrease in the magnetic susceptibility as temperature decreases. Furthermore, below this transition the resistivity, which shows semiconducting behavior at high temperatures, begins to rapidly increase to a maximum at 23 K. After this maximum, $CeRu_2Al_{10}$ displays metallic resistivity.[2.21] Based on heat capacity and Knight shift experiments, the transition is a second order phase transition which is accompanied by the opening of a gap at the Fermi surface.[2.22] Single crystal neutron diffraction indicates that $CeRu_2Al_{10}$ is an antiferromagnet with a (1,0,0) propagation vector.[2.23] However, it is still unclear what mechanism leads to the higher ordering than $GdRu_2Al_{10}$.[2.24]

The properties of $LnOs_2Al_{10}$ (*Ln* = Ce, Pr, Nd, Sm, and Gd) have also been reported. The Ce analogue displays similar properties to $CeRu_2Al_{10}$ except with an ordering temperature of 28.7

K.[2.20] The Pr analogue shows no magnetic ordering down to 0.4 K, whereas the other three analogues show antiferromagnetic ordering. Following the magnetic ordering, the Sm analogue has two further magnetic transitions, and the Gd has one. Below the initial antiferromagnetic ordering, the resistivities of the Sm and Gd analogues increase before decreasing again at even lower temperatures.[2.13]

Due to the properties of $CeRu_2Al_{10}$ and $LnOs_2Al_{10}$ (*Ln* = Ce, Nd, Sm, Gd), it is of interest to grow other lanthanide analogues of $LnRu_2Al_{10}$ to determine the role of the lanthanide on the physical properties of this family of compounds. Herein, we report the synthesis, structure, and physical properties of $LnM_2Al_{10}$ (*Ln* = Pr, Gd and Yb).

## 2.2 Experimental

### 2.2.1 Synthesis

Pr (Chunks- 99.9% metal basis excluding Ta), Gd (Chunks- 99.9% metal basis excluding Ta), Yb (chunks- 99.9% REO), Al (Shot- 99.999%), and Ru (Powder- 99.9%) were used as received. No evidence for the incorporation of Ta into the crystals was seen for either the Pr or Gd analogues. For all syntheses except $PrRu_2Al_{10}$, the lanthanide, ruthenium, and aluminum were combined in a 1:1:20 atomic ratio in an alumina crucible. For the Pr analogue, a ratio of 1:2:40 was used in order to prevent the growth of $Pr_3Al_{11}$. A second crucible was inverted on top of the first, and the two crucibles were sealed in an evacuated fused-silica tube. For the synthesis of $PrRu_2Al_{10}$ and $GdRu_2Al_{10}$, the sealed tube was rapidly heated to 1150 °C and dwelled at this temperature for 24 h. The tube was then cooled to 720 °C at a rate of 15 °C/h. After cooling, the samples were inverted and spun to remove excess flux. For the synthesis of $YbRu_2Al_{10}$, a similar heating scheme was utilized except that the dwell temperature was lowered to 1050 °C due to the higher vapor pressure of ytterbium compared to the other lanthanides. After spinning, the

remaining aluminum flux was removed from the surface of the crystals using dilute HCl so that physical properties could be obtained on clean single crystals.

Figure 2.1 shows crystals typical of each growth. Crystals of the Pr and Gd analogues were about 3 mm on each side, while crystals of $YbRu_2Al_{10}$ were typically 1 mm on each side or smaller. In an attempt to grow larger crystals of the Yb analogue, a cooling rate of 5 °C/h was attempted. However, there was no noticeable increase in crystal size.

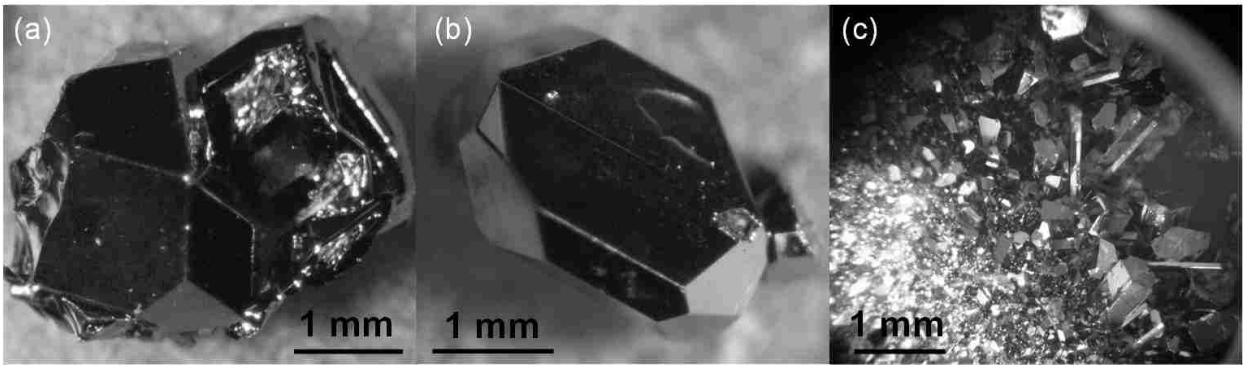


**Figure 2.1** Crystals typical for the growth of the (a) Pr, (b) Gd, and (c) Yb analogues of *Ln*$Ru_2Al_{10}$.

### 2.2.2 Structure

Single crystals were characterized by single crystal X-ray diffraction using an Enraf Nonius KappaCCD diffractometer with a Mo $K_\alpha$ source ($\lambda$ = 0.71 Å). An initial structural model was obtained through direct methods using SIR92.[2.25] This model was refined using SHELXL-97.[2.26] Crystallographic data and atomic positions for the refinement of each analogue can be found in Tables 2.1 and 2.2.

The composition of each analogue was confirmed by energy dispersive spectroscopy, EDS, data obtained using an FEI Quanta 200 SEM equipped with an EDAX detector. The compositions of the three analogues, as indicated by EDS, were $Pr_{1.00(7)}Ru_{2.09(16)}Al_{10.6(8)}$, $Gd_{1.00(2)}Ru_{2.03(8)}Al_{9.42(2)}$, and $Yb_{1.00(6)}Ru_{1.36(10)}Al_{8.0(5)}$. To ensure the homogeneity of single crystals, powder X-ray diffraction of ground single crystals was performed using a Bruker AXS D8 Advance

Diffractometer with a Cu Kα source (λ = 1.54 Å) equipped with a Ge incident beam monochromator.

**Table 2.1** Crystallographic Data for $Ln Ru_2Al_{10}$ (*Ln* = Pr, Gd, Yb)

| Formula | **$PrRu_2Al_{10}$** | **$GdRu_2Al_{10}$** | **$YbRu_2Al_{10}$** |
|---|---|---|---|
| Space group | *Cmcm* | *Cmcm* | *Cmcm* |
| *a* (Å) | 9.1232(15) | 9.0930(15) | 9.0850(15) |
| *b* (Å) | 10.2664(10) | 10.218(2) | 10.2150(15) |
| *c* (Å) | 9.1800(15) | 9.1370(15) | 9.1110(15) |
| *V* (Å$^3$) | 859.82(4) | 848.9(3) | 845.5(2) |
| *Z* | 4 | 4 | 4 |
| Crystal dimensions (mm$^3$) | 0.06x0.06x0.12 | 0.07x0.10x0.13 | 0.02x0.07x0.10 |
| Temperature (K) | 298(3) | 298(3) | 298(3) |
| Density (g cm$^{-3}$) | 4.734 | 4.923 | 5.067 |
| $\theta$ Range (°) | 2.99-31.04 | 3-30.98 | 3-30.02 |
| $\mu$ (mm$^{-1}$) | 9.988 | 12.189 | 15.455 |
| *Data Collection and Refinement* | | | |
| Collected reflections | 1328 | 1313 | 1181 |
| Unique reflections | 760 | 750 | 672 |
| $R_{int}$ | 0.0164 | 0.0223 | 0.0253 |
| *h* | $-13 \le h \le 13$ | $-13 \le h \le 13$ | $-12 \le h \le 12$ |
| *k* | $-14 \le k \le 14$ | $-14 \le k \le 14$ | $-14 \le k \le 14$ |
| *l* | $-13 \le l \le 13$ | $-13 \le l \le 13$ | $-12 \le l \le 12$ |
| $\Delta\rho_{max}$ (e Å$^{-3}$) | 2.059 | 2.914 | 1.608 |
| $\Delta\rho_{min}$ (e Å$^{-3}$) | -1.511 | -1.255 | -0.932 |
| GoF | 1.149 | 1.161 | 1.075 |
| Extinction coefficient | 0.0131(4) | 0.0230(5) | 0.0177(4) |
| [a] $R_1(F)$ for $F_o^2 > 2\sigma(F_o^2)$ | 0.0191 | 0.0207 | 0.0191 |
| [b] $R_w(F_o^2)$ | 0.0441 | 0.0415 | 0.0392 |

[a] $R_1 = \Sigma||F_0| - |F_c||/\Sigma|F_0|$

[b] $wR_2 = [\Sigma w(F_o^2 - F_c^2)^2/\Sigma w(F_0^2)^2]^{1/2}$; $P = (F_o^2 + 2F_c^2)/3$; $w = 1/[\sigma^2(F_o^2) + (0.0232P)^2 + 1.7949P]$, $w = 1/[\sigma^2(F_o^2) + (0.0116P)^2 + 0.0000P]$, and $w = 1/[\sigma^2(F_o^2) + (0.0078P)^2 + 0.0000P]$ for Pr, Gd and Yb analogues, respectively

**Table 2.2** Atomic Coordinates and Atomic Displacement Parameters for *Ln*$Ru_2Al_{10}$ (*Ln* = Pr, Gd, Yb)

| Atom | Wyckoff site | *x* | *y* | *z* | $U_{eq}$ (Å$^2$)[a] |
|---|---|---|---|---|---|
| Pr(1) | 4*c* | 0 | 0.12424(2) | ¼ | 0.00703(11) |
| Ru(1) | 8*d* | ¼ | ¼ | 0 | 0.00522(10) |
| Al(1) | 8*g* | 0.22436(13) | 0.36401(10) | ¼ | 0.0083(2) |
| Al(2) | 8*g* | 0.35026(13) | 0.13025(10) | ¼ | 0.0085(2) |
| Al(3) | 8*f* | 0 | 0.16051(10) | 0.60094(12) | 0.0078(2) |
| Al(4) | 8*f* | 0 | 0.37721(10) | 0.44980(13) | 0.0093(2) |
| Al(5) | 8*e* | 0.22681(14) | 0 | 0 | 0.0083(2) |
| | | | | | |
| Gd(1) | 4*c* | 0 | 0.12674(3) | ¼ | 0.00777(12) |
| Ru(1) | 8*d* | ¼ | ¼ | 0 | 0.00548(12) |
| Al(1) | 8*g* | 0.22231(16) | 0.36405(12) | ¼ | 0.0088(3) |
| Al(2) | 8*g* | 0.34965(15) | 0.13058(11) | ¼ | 0.0086(3) |
| Al(3) | 8*f* | 0 | 0.15748(12) | 0.60019(13) | 0.0082(2) |
| Al(4) | 8*f* | 0 | 0.37660(11) | 0.45121(14) | 0.0094(3) |
| Al(5) | 8*e* | 0.22564(16) | 0 | 0 | 0.0088(3) |
| | | | | | |
| Yb(1) | 4*c* | 0 | 0.12507(3) | ¼ | 0.00883(13) |
| Ru(1) | 8*d* | ¼ | ¼ | 0 | 0.00583(13) |
| Al(1) | 8*g* | 0.22192(19) | 0.36322(13) | ¼ | 0.0093(3) |
| Al(2) | 8*g* | 0.34793(17) | 0.12904(12) | ¼ | 0.0094(3) |
| Al(3) | 8*f* | 0 | 0.15537(13) | 0.59921(16) | 0.0091(3) |
| Al(4) | 8*f* | 0 | 0.37544(12) | 0.45334(17) | 0.0098(3) |
| Al(5) | 8*e* | 0.22518(19) | 0 | 0 | 0.0096(3) |

[a] $U_{eq}$ is defined as one-third of the trace of the orthogonalized $U_{ij}$ tensor.

### 2.2.3 Physical Property Measurements

Physical properties of $LnRu_2Al_{10}$ (*Ln* = Pr, Gd, Yb) were measured using a Quantum Design Physical Property Measurement System (PPMS). Magnetization was measured as a function of applied field up to 9 T at 3 K. The temperature dependent DC magnetization was measured under zero-field cooled conditions at 0.1 T, for the Pr and Yb analogues, or 1 T, for the Gd analogue. Resistivity was measured as a function of temperature using the four probe method with an excitation current of 5.13 mA, for the Pr analogue, or 8.21 mA for the Gd and Yb analogues. Magnetoresistance was measured at 3 K.

## 2.3 Results and Discussion

### 2.3.1 Structure

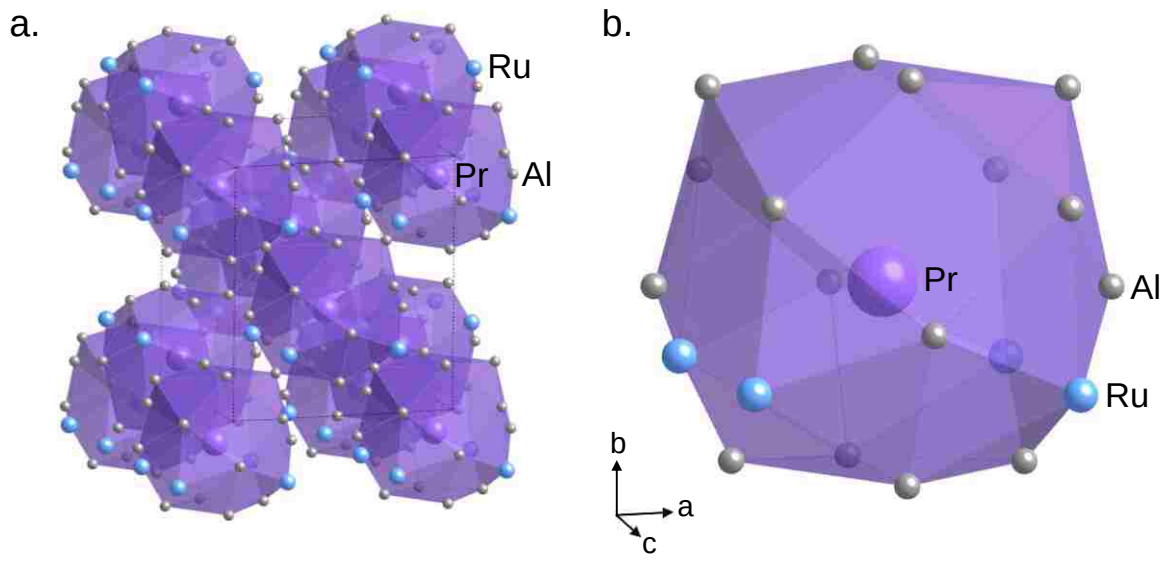


**Figure 2.2** (a) Structure of $PrRu_2Al_{10}$ and (b) the Pr polyhedral environment.

$LnRu_2Al_{10}$ (*Ln* = Pr, Gd, Yb) are members of the $YbFe_2Al_{10}$ structure type[2,4] and crystallize in the orthorhombic space group C*mcm*. Each ruthenium atom is surrounded by 10 aluminum and 2 lanthanide atoms in a distorted icosahedral geometry with point symmetry -1. The Ru-Al distances range from 2.5753(3) - 2.7595(7) Å, 2.5641(5) - 2.7437(8) Å, 2.5637 - 2.7398(8) Å, and

the Ru-*Ln* distances are 3.4837(4) Å, 3.4600(4) Å, and 3.4606(4) Å for the Pr, Gd, and Yb analogues, respectively. These polyhedra are edge-sharing in the *ac* plane and corner-sharing in the *b*-direction. As shown in Figure 2.2b, each lanthanide atom is surrounded by 16 aluminum and 4 ruthenium atoms with point symmetry *m*2*m*. The *Ln*-Al distances range from 3.1794(11) - 3.6690(12) Å, 3.1461(13) - 3.6852(14) Å, and 3.1581(14) - 3.6793(16) Å, for the Pr, Gd, and Yb analogues, respectively. These contact distances are larger than the sum of the covalent radii and may explain why the atomic displacement parameters for the lanthanide atoms are similar in size to those of the Al atoms. The somewhat cage-like environment of the lanthanide atoms allows for increased motion as compared to the closer bound Ru and Al atoms. This increased motion is considerably less pronounced than in caged compounds such as clathrates and skutteridites, where

**Table 2.3** Select Interatomic Distances in *Ln*$Ru_2Al_{10}$ (Å)

| Interaction | $PrRu_2Al_{10}$ | $GdRu_2Al_{10}$ | $YbRu_2Al_{10}$ |
|---|---|---|---|
| *Ln*(1)-Ru(1) (x4) | 3.4837(4) | 3.4600(4) | 3.4606(4) |
| *Ln*(1)-Al(1) (x2) | 3.2014(12) | 3.1569(14) | 3.1596(16) |
| *Ln*(1)-Al(1) (x2) | 3.6690(12) | 3.6852(14) | 3.6793(16) |
| *Ln*(1)-Al(2) (x2) | 3.1961(13) | 3.1796(15) | 3.1612(16) |
| *Ln*(1)-Al(3) (x2) | 3.2278(11) | 3.2106(13) | 3.1771(14) |
| *Ln*(1)-Al(3) (x2) | 3.2431(12) | 3.2151(13) | 3.1967(15) |
| *Ln*(1)-Al(4) (x2) | 3.1794(11) | 3.1461(13) | 3.1581(14) |
| *Ln*(1)-Al(5) (x4) | 3.3430(9) | 3.3324(10) | 3.3174(11) |
| | | | |
| Ru(1)-*Ln*(1) (x2) | 3.4837(4) | 3.4600(4) | 3.4606(4) |
| Ru(1)-Al(1) (x2) | 2.5868(6) | 2.5767(6) | 2.5673(7) |
| Ru(1)-Al(2) (x2) | 2.7595(7) | 2.7437(8) | 2.7398(8) |
| Ru(1)-Al(3) (x2) | 2.6277(6) | 2.6267(7) | 2.6287(8) |
| Ru(1)-Al(4) (x2) | 2.6683(6) | 2.6533(7) | 2.6422(7) |
| Ru(1)-Al(5) (x2) | 2.5753(3) | 2.5641(5) | 2.5637(4) |

the room temperature ADP of the rattler atom is often several times larger than the other atoms.[2.27, 28] The *Ln* polyhedra are face-sharing and form columns in the *c*-direction with the closest lanthanide contacts being 5.2509(8) Å, 5.2516(7) Å and 5.2232(7) Å for the Pr, Gd and Yb analogues, respectively, as shown in Figure 2.2a. Bond distances for the *Ln* and Ru polyhedra can be found in Table 2.3.

The lattice parameters for $YbRu_2Al_{10}$, $a$ = 9.0850 (15) Å, $b$ = 10.2150(15) Å and $c$ = 9.1110(15) Å, are only slightly smaller than the lattice parameters of the Gd analogue, $a$ = 9.0930(15) Å, $b$ = 10.218(2) Å and $c$ = 9.1370(15) Å, and the volume (845.5(2) $Å^3$) is intermediate of Tb (845.6(5) $Å^3$) and Ho (843.7(6) $Å^3$).[2.12]

### 2.3.2 Magnetic Properties

Table 2.4 provides a summary of the magnetic data of the reported $LnM_2Al_{10}$ (M = Ru, Os) analogues from this work and previously reported measurements. For the magnetic lanthanides, $\mu H << k_BT$ such that the internal interactions and not the external field should dominate the magnetization. Figure 2.3a shows the magnetic susceptibility of $PrRu_2Al_{10}$ measured at 0.1 T. The high temperature data were fitted using a modified Curie-Weiss law, $\chi = \chi_o + C/(T - \theta)$, where $\chi_o$ is a temperature independent term which accounts for the Pauli paramagnetic and diamagnetic contributions. Fitting down to 50 K yields a paramagnetic Curie-Weiss temperature of -49.8(14) K and a $\mu_{eff}$ of 3.60(3) $\mu_B$/Pr, close to the 3.58 $\mu_B$ expected for $Pr^{3+}$. A kink at 13.2 K is indicative of a non-magnetic singlet ground state for $Pr^{3+}$ caused by crystal electric field (CEF) splitting of the 4*f* orbitals. Similar behavior was also observed in $PrOs_2Al_{10}$[2.13] and other Pr containing compounds such as $PrTi_2Al_{10}$.[2.29] The CEF splitting has previously been calculated for $CeRu_2Al_{10}$, where the first two CEF splittings were found to be 500 K and 760 K. The lack of magnetic ordering in $PrRu_2Al_{10}$ is similar to that of $PrOs_2Al_{10}$[2.13] and $PrFe_2Al_{10}$, the latter of which was

**Table 2.4** Magnetic Properties for Select $LnM_2Al_{10}$ (*Ln* = Lanthanide; M = Fe, Ru, Os)

| | $\chi_o$ | $T_N$ (K) | θ (K) | $\mu_{calc}$ ($\mu_B$) | $\mu_{eff}$ ($\mu_B$) | Fit Range (K) | Ref. |
|---|---|---|---|---|---|---|---|
| $PrFe_2Al_{10}$ | | — | 0 | 3.58 | 3.6(1) | | 2.12 |
| $GdFe_2Al_{10}$ | | 15 | 0 | 7.94 | 7.9(1) | | 2.12 |
| $CeRu_2Al_{10}$ | | 27.3 | -44 | 2.54 | 3.03 | | 2.30 |
| $PrRu_2Al_{10}$ | 0.00122(8) | — | -49.8(14) | 3.58 | 3.60(3) | 50-250 | |
| $GdRu_2Al_{10}$ | 0.00015(4) | 15.5 | -15.45(8) | 7.94 | 8.14(10) | 50-275 | |
| $YbRu_2Al_{10}$ | — | — | — | — | — | — | |
| $CeOs_2Al_{10}$ | | 28.6 | -30 | 2.54 | 2.7 | | 2.31 |
| $PrOs_2Al_{10}$ | | — | -10 | 3.58 | 3.4 | | 2.13 |
| $NdOs_2Al_{10}$ | | 2.2 | -6 | 3.62 | 3.3 | | 2.13 |
| $SmOs_2Al_{10}$ | | 12.5 | -4 | 0.85 | 0.69 | | 2.13 |
| $GdOs_2Al_{10}$ | | 18 | -13 | 7.94 | 7.6 | | 2.13 |

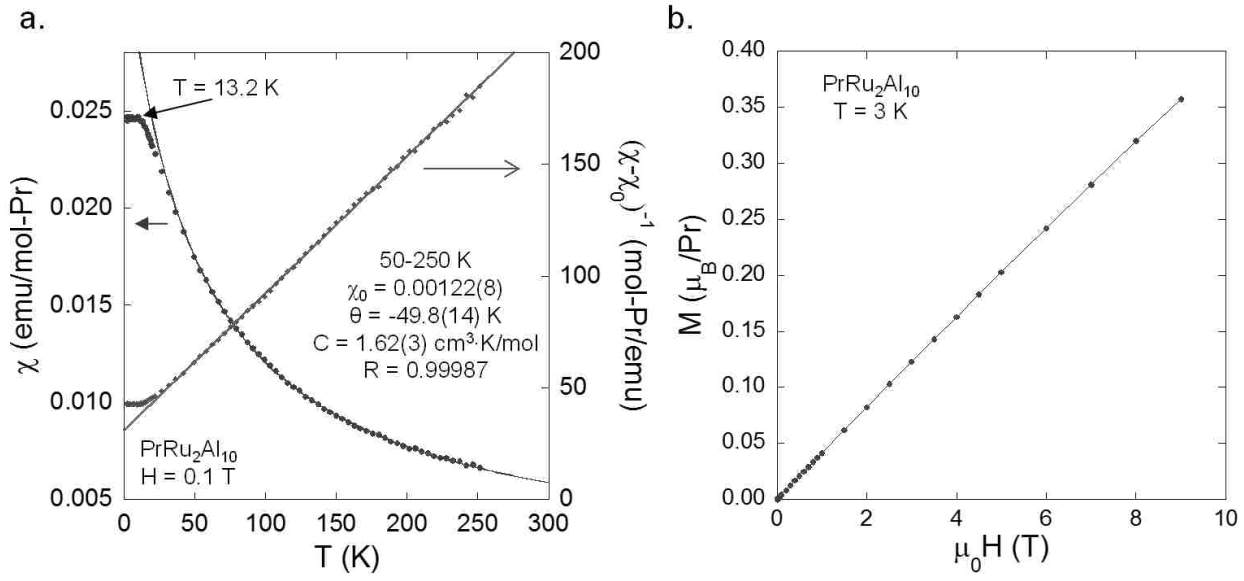


**Figure 2.3** (a) Magnetic susceptibility and inverse susceptibility of $PrRu_2Al_{10}$. (b) Field-dependent magnetization of $PrRu_2Al_{10}$.

found to be paramagnetic down to 3 K.[2.12] However, the paramagnetic Curie-Weiss temperatures for the Fe and Os analogues, 0 and -10 K, respectively, are substantially smaller than that of the Ru analogue.[2.12, 13] While CEF effects can lead to negative paramagnetic Curie-Weiss temperatures, the large $\theta_N$ (-49.8(14) K) of the $PrRu_2Al_{10}$ compared to that of $PrOs_2Al_{10}$, which shows similar CEF splitting, suggests stronger antiferromagnetic correlations in the Ru analogue than the Fe and Os analogues. Magnetization as a function of applied field is shown in Figure 2.3b and no hysteresis or saturation is observed.

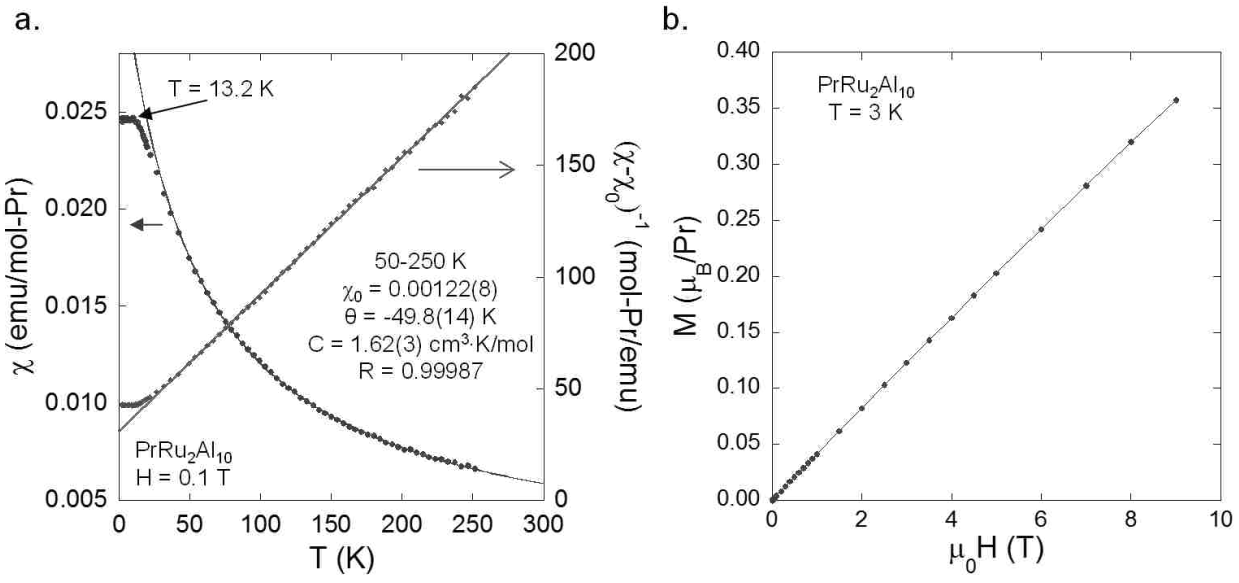


**Figure 2.3** (a) Magnetic susceptibility and inverse susceptibility of $PrRu_2Al_{10}$. (b) Field-dependent magnetization of $PrRu_2Al_{10}$.

Figure 2.4a shows the magnetic susceptibility of $GdRu_2Al_{10}$. This phase orders antiferromagnetically at 15.5 K, which is in agreement with previous work.[2.20] Below the antiferromagnetic transition, a spin reorientation is seen at 7.8 K. Fitting $\chi^{-1}$ down to 50 K using a modified Curie-Weiss law results in a $\theta_N$ of -15.45(8) K and a $\mu_{eff}$ of 8.14(10) $\mu_B$/Gd. While the effective moment is 2.5% higher than the 7.94 $\mu_B$ which is expected for $Gd^{3+}$, it is not believed that the Ru atoms carry a moment, as ruthenium is a 4d transition metal and typically does not

carry a magnetic moment. This is further supported by the fact that no localized moment was observed on the Ru atoms in $YbRu_2Al_{10}$, a Pauli paramagnet in which Yb is divalent. Magnetization as a function of applied field is shown in Figure 2.4b. The magnetic moment does not saturate, only reaching 3.82 $\mu_B$/Gd at 9 T. A change of slope is seen between 1 T and 1.5 T, possibly indicative of a metamagnetic transition.

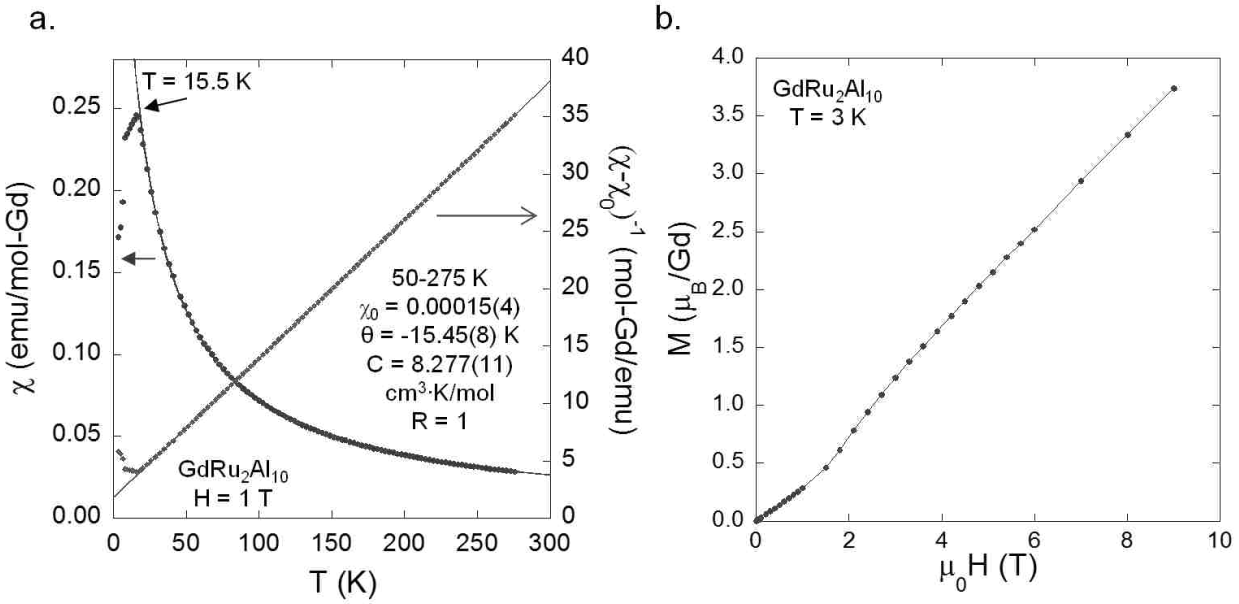


**Figure 2.4** (a) Magnetic susceptibility and inverse susceptibility of $GdRu_2Al_{10}$. (b) Field-dependent magnetization of $GdRu_2Al_{10}$.

The previously reported $GdFe_2Al_{10}$ and $GdOs_2Al_{10}$ were found to order antiferromagnetically at 15(3) K[2.12] and 18 K,[2.13] respectively. The unit cell volumes of the Fe, Ru and Os analogues, 829.9 Å$^3$,[2.12] 848.9(3) Å$^3$, and 856.58 Å$^3$,[2.13] respectively, suggest that the Gd-Gd interaction distances increase down the Fe triad. The increase in ordering temperature with increasing Gd-Gd distances is possibly due to an increase in conduction electron concentration down the triad as $GdRu_2Al_{10}$ was found to have a higher resistivity than $GdOs_2Al_{10}$.[2.13] The trend may also be explained by the cosine dependence of the RKKY interaction.

Magnetization measurements, not shown, suggest that $YbRu_2Al_{10}$ is a Pauli paramagnet, indicating that Yb is in its nonmagnetic 2+ state. The field dependent susceptibility reaches a maximum at 0.4 T before the diamagnetic contribution of the sample holder becomes observable. As shown in Table 2.1, the unit cell volume for the Yb analogue is 3.4(4) $Å^3$ smaller than the Gd analogue. While a unit cell size close to that of the Sm analogue is typically expected for $Yb^{2+}$ containing compounds, due to the polyhedral rare earth environment in $LnRu_2Al_{10}$, the smaller unit cell size is not unexpected. Although the Yb in $YbFe_2Al_{10}$ is mixed valent, $YbFe_2Al_{10}$ and $YbRu_2Al_{10}$ display similar deviations from the expected lanthanide contraction.[2.12] This suggests that the Yb in the Fe analogue may actually be diamagnetic and the observed magnetism arises as a result of an Fe magnetic moment. In many *Ln*TX (*Ln* = lanthanide, T = 3d transition metal, X = p block element) compounds, when the lanthanide is non-magnetic, the transition metal carries a magnetic moment.[2.2]

### 2.3.3 Transport Properties

The resistivities of $PrRu_2Al_{10}$, $GdRu_2Al_{10}$ and $YbRu_2Al_{10}$ are shown in Figure 2.5a-c, respectively. Each analogue displays metallic resistivity, although the Gd analogue is a poor metal with a resistivity on the order of 1 mΩ·cm. The Pr and Yb analogues have similar residual resistivities of 6.60(15) μΩ·cm for $PrRu_2Al_{10}$ and 6.0(2) μΩ·cm for $YbRu_2Al_{10}$. $GdRu_2Al_{10}$, on the other hand, displays a considerably higher residual resistivity of 190(6) μΩ·cm. A similar, although less pronounced, trend was observed in the $LnOs_2Al_{10}$ series with the Gd analogue having a higher resistivity than the Pr analogue.[2.13] While the Pr and Yb analogues have similar residual resistivities, $YbRu_2Al_{10}$ has a higher resistivity at 290 K, 423.18(12) μΩ·cm, than the Pr analogue, 120.5(2) μΩ·cm. As a result, $YbRu_2Al_{10}$ has a residual resistivity ratio ($\rho_{(290\ K)}/\rho_{(3\ K)}$) of 70.5, greater than the RRR for $PrRu_2Al_{10}$, 18.3, and $GdRu_2Al_{10}$, 8.9. This indicates that the $YbRu_2Al_{10}$

sample has a greater crystal quality than the other two analogues. This can be explained by the dwell temperature required to grow each analogue. The Yb analogue was grown with a dwell temperature of 1050 °C while the other two analogues where grown with a dwell temperature of 1150 °C. As the number of defects increases with temperature, a higher growth temperature means the Gd and Pr analogues should have lower crystal qualities than the Yb analogue. Attempts to grow $GdRu_2Al_{10}$ at the lower dwell temperature only resulted in polycrystalline product supporting that this analogue formed at higher temperatures than 1050 °C. The lower crystal quality of the Gd analogue, as compared to the other two, may be the cause of the higher residual resistivity of $GdRu_2Al_{10}$.

At low temperatures, the resistivities of $PrRu_2Al_{10}$, $T \leq 70$ K, and $GdRu_2Al_{10}$, $25\ K \leq T \leq 140$ K, display $T^2$ dependences, which is typical of Fermi liquids, i.e. metallic compounds. This indicates that the dominant factor contributing to the resistivity at low temperatures is electron-electron scattering and not the magnetic contribution to the resistivity. While the Yb analogue also displays a $T^2$ dependence for $65\ K \leq T \leq 150$ K , below 65 K, it displays a $T^3$ dependent resistivity. This dependence can be attributed to scattering by phonon mediated s-d transitions and has been observed in other Pauli paramagnetic compounds.[2.32]

The resistivity of $GdRu_2Al_{10}$ displays a sharp decrease at 15.2 K. This corresponds to the antiferromagnetic ordering and can be attributed to spin-reduced scattering. Prior to the antiferromagnetic transition, the resistivity has a slight upturn at 25.1 K. This upturn is reminiscent of the increase in resistivity at 20 K of $EuB_6$, another compound in which the rare earth adopts a $4f^7$ configuration.[2.33] In $EuB_6$ the upturn in the resistivity is due to the formation of magnetic polarons prior to the magnetic ordering.[2.34] The magnetoresistance of each analogue, not shown, was measured at 3 K and found to remain below 2.5 % up to 9 T.

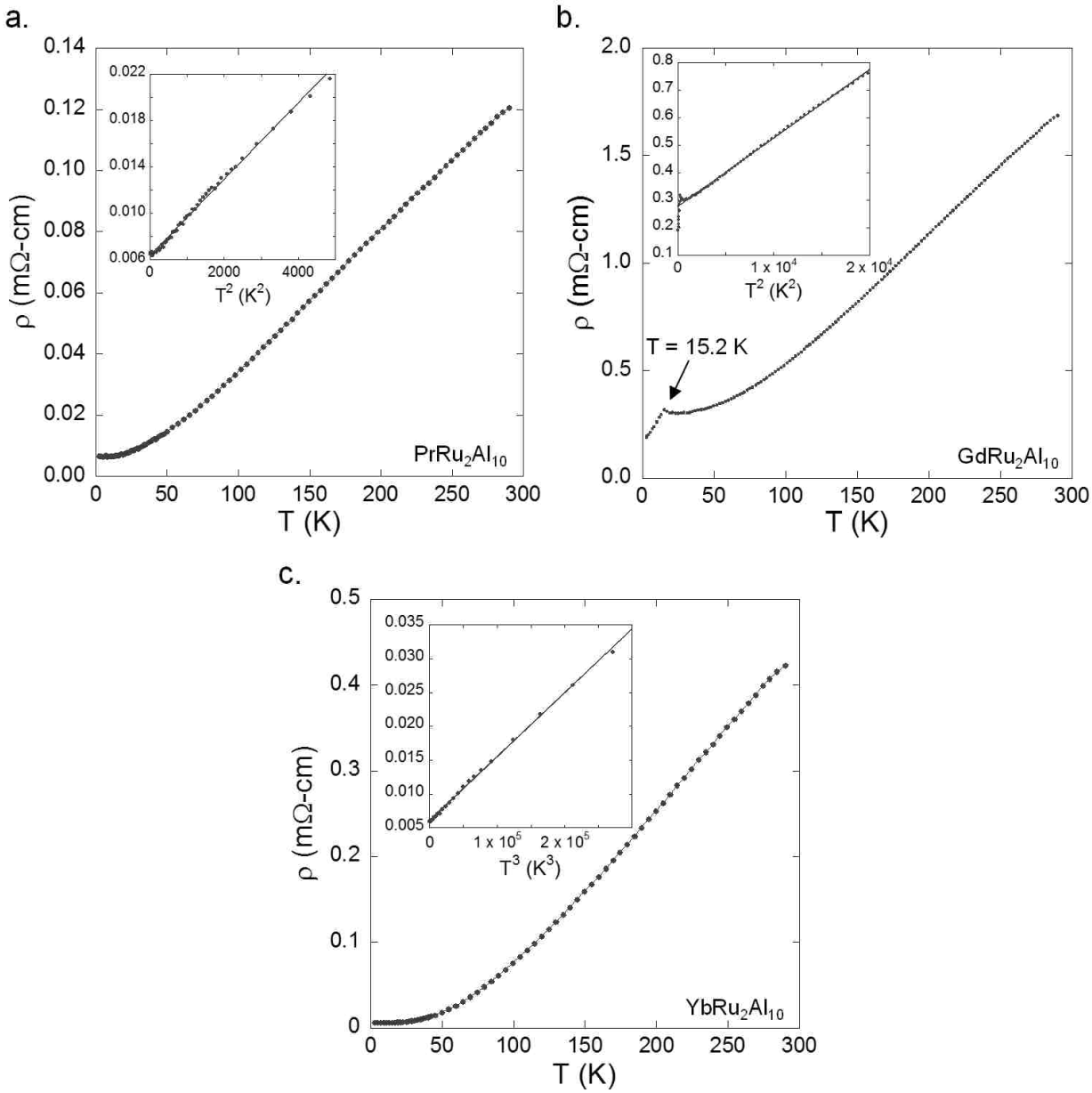


**Figure 2.5** Resistivity of (a) $PrRu_2Al_{10}$, (b) $GdRu_2Al_{10}$, and (c) $YbRu_2Al_{10}$. Insets highlight the low temperature dependence of the resistivity for each analogue.

## 2.4 Conclusion

We report the structure and physical properties of flux grown single crystals of $LnRu_2Al_{10}$ (*Ln* = Pr, Gd, Yb). $GdRu_2Al_{10}$ was found to order antiferromagnetically at 15.5 K with a paramagnetic Curie-Weiss temperature of a similar magnitude. $PrRu_2Al_{10}$, on the other hand, displays no magnetic ordering but has a $\theta_N$ of -49.8(14) K. Crystal electric field splitting leads to

a non-magnetic singlet ground state for $Pr^{3+}$ causing a kink in the susceptibility at 13.2 K and possibly contributing to the large negative paramagnetic Curie-Weiss temperature. $YbRu_2Al_{10}$ was found to be a Pauli paramagnet, indicating the Yb is divalent.

## 2.5 References


2.1. Phelan, W. A.; Menard, M. C.; Kangas, M. J.; McCandless, G. T.; Drake, B. L.; Chan, J. Y., *Chem. Mater.* **2012,** *24*, 409-420.

2.2. Drake, B. L.; Grandjean, F.; Kangas, M. J.; Okudzeto, E. K.; Karki, A. B.; Sougrati, M. T.; Young, D. P.; Long, G. J.; Chan, J. Y., *Inorg. Chem.* **2009,** *49*, 445-456.

2.3. Nakamura, H.; Muro, Y.; Giri, S.; Umemura, J.; Kobayashi, H.; Koyama, T.; Kohara, T., *J. Phys. Soc. Jpn.* **2005,** *74*, 2421-2424.

2.4. Niemann, S.; Jeitschko, W., *Z. Krist.* **1995,** *210*, 338-341.

2.5. Tursina, A. I.; Bukhan'ko, N. G.; Gribanov, A. V.; Noël, H.; Roisnel, T.; Seropegin, Y. D., *J. Alloys Compd.* **2005,** *400*, 194-196.

2.6. Tursina, A. I.; Murashova, E. V.; Nesterenko, S. N.; Chernyshev, I. V.; No; l, H.; Seropegin, Y. D., *Acta Crystallogr. Sect. E* **2004,** *60*, i145-i146.

2.7. Niemann, J.; Jeitschko, W., *Z. anorg. allg. Chem.* **2002,** *628*, 2549-2556.

2.8. Hermes, W.; Matar, S. F.; Pöttgen, R., *Z. Naturforsch.* **2009,** *64b*, 901-908.

2.9. Murashova, E. V.; Tursina, A. I.; Kurenbaeva, Z. M.; Noël, H.; Seropegin, Y. D., *Chem. Met. Alloys* **2010,** *3*, 101-107.

2.10. Murashova, E. V.; Tursina, A. I.; Bukhanko, N. G.; Nesterenko, S. N.; Kurenbaeva, Z. M.; Seropegin, Y. D.; Noël, H.; Potel, M.; Roisnel, T.; Kaczorowski, D., *Mater. Res. Bull.* **2010,** *45*, 993-999.

2.11. Tappe, F.; Schwickert, C.; Linsinger, S.; Pöttgen, R., *Monatsh. Chem.* **2011,** *142*, 1087-1095.

2.12. Thiede, V. M. T.; Ebel, T.; Jeitschko, W., *J. Mater. Chem.* **1998,** *8*, 125-130.

2.13. Muro, Y.; Kajino, J.; Onimaru, T.; Takabatake, T., *J. Phys. Soc. Jpn.* **2011,** *80*, SA021.

2.14. Noël, H.; Gonçalves, A. P.; Waerenborgh, J. C., *Intermetallics* **2004,** *12*, 189-194.

2.15. Troc, R.; Pasturel, M.; Tougait, O.; Potel, M.; Noël, H., *Intermetallics* **2011,** *19*, 913-918.

2.16. Takashi, S.; Yoshinori, H.; Tatsuma, D. M.; Etsuji, Y.; Naoyuki, T.; Fuminori, H.; Rikio, S.; Yoshichika, O., *J. Phys.: Conf. Ser.* **2011,** *273*, 012122.

2.17. Thiede, V. M. T.; Jeitschko, W., *Z. Naturforsch.* **1998,** *53b*, 673-678.

2.18. Fulfer, B. W.; Haldolaarachchige, N.; Young, D. P.; Chan, J. Y., *J. Solid State Chem.* **2012**, In Press.

2.19. Park, K.; Wu, L. S.; Janssen, Y.; Kim, M. S.; Marques, C.; Aronson, M. C., *Phys. Rev. B* **2011,** *84*, 094425.

2.20. Nishioka, T.; Kawamura, Y.; Takesaka, T.; Kobayashi, R.; Kato, H.; Matsumura, M.; Kodama, K.; Matsubayashi, K.; Uwatoko, Y., *J. Phys. Soc. Jpn.* **2009,** *78*, 123705.

2.21. Strydom, A. M., *Physica B* **2009,** *404*, 2981-2984.

2.22. Lue, C. S.; Yang, S. H.; Abhyankar, A. C.; Hsu, Y. D.; Hong, H. T.; Kuo, Y. K., *Phys. Rev. B* **2010,** *82*, 045111.

2.23. Mignot, J.-M.; Robert, J.; André, G.; Bataille, A. M.; Nishioka, T.; Kobayashi, R.; Matsumura, M.; Tanida, H.; Tanaka, D.; Sera, M., *J. Phys. Soc. Jpn.* **2011,** *80*, SA022.

2.24. Kawamura, Y.; Ogane, Y.; Nishioka, T.; Kato, H.; Matsumura, M.; Tanaka, D.; Tanida, H.; Sera, M.; Kondo, A.; Matsubayashi, K.; Uwatoko, Y., *J. Phys. Soc. Jpn.* **2011,** *80*, SA046.

2.25. Altomare, A.; Burla, M. C.; Camalli, M.; Cascarano, G.; Giacovazzo, C.; Guagliardi, A.; Polidori, G., *J. Appl. Crystallogr.* **1994,** *27*, 435.

2.26. Sheldrick, G. M., *Acta Crystallogr. Sect. A* **2008,** *64*, 112-122.

2.27. Chakoumakos, B. C.; Sales, B. C.; Mandrus, D. G., *J. Alloys Compd.* **2001,** *322*, 127-134.

2.28. Sales, B. C.; Mandrus, D.; Chakoumakos, B. C.; Keppens, V.; Thompson, J. R., *Phys. Rev. B: Condens. Matter* **1997,** *56*, 15081-15089.

2.29. Sakai, A.; Nakatsuji, S., *J. Phys. Soc. Jpn.* **2011,** *80*, 063701.

2.30. Takesaka, T.; Oe, K.; Kobayashi, R.; Kawamura, Y.; Nishioka, T.; Kato, H.; Matsumura, M.; Kodama, K., *J. Phys. Conf. Ser.* **2010,** *200*, 012201.

2.31. Muro, Y.; Kajino, J.; Umeo, K.; Nishimoto, K.; Tamura, R.; Takabatake, T., *Phys. Rev. B* **2010,** *81*, 214401.

2.32. Ramesh, R.; Rama Rao, K. V. S., *J. Appl. Phys* **1994,** *76*, 3556-3561.

2.33. Wigger, G. A.; Monnier, R.; Ott, H. R.; Young, D. P.; Fisk, Z., *Phys. Rev. B* **2004,** *69*, 125118.

2.34. Snow, C. S.; Cooper, S. L.; Young, D. P.; Fisk, Z.; Comment, A.; Ansermet, J.-P., *Phys. Rev. B* **2001,** *64*, 174412.

# Chapter 3.[†] Serendipitous Growth of Single Crystals with Silicon Incorporation

## 3.1 Introduction

The availability of single crystals over polycrystalline samples is desirable for many reasons including structural determination via single crystal X-ray diffraction and the measurement of anisotropic physical properties. The self-flux method for the growth of single crystals has several advantages over other solid state growth methods. Arc-melting is not conducive to the growth of single crystals because the very high reaction temperatures (~ 3000 °C) and fast cooling rate typically results in polycrystalline samples. Other single crystal growth methods often require extensive equipment, such as floating zone furnaces, or large reactant amounts, such as in the Czochralski method. In the self-flux method, the solubility of metals in a low-melting flux allows for the synthesis of new materials at lower reaction temperatures. Furthermore, the self-flux growth method can be performed using small amounts of reactant metals, often less than one gram, and can be carried out in a conventional high temperature furnace. Finally, the high degree of control over reaction conditions which the self-flux method provides allows for the synthesis of congruently melting, incongruently melting, and even metastable phases.

While the flux growth method is a very versatile method, growing single crystals of one compound can be challenging when another compound is very stable and robust. An examples of the competition between the growth of two compounds can be found in the *Ln*:M:X:Si (*Ln* = lanthanide; M = transition metal; X = Al, Ga) phase space. In the flux growth method, silica wool is typically used to aid in the separation of crystals from the excess flux. In high temperature (1200 °C) growths involving Al or Ga flux, the wool is very soluble, and can allow silica to enter the

[†]Reproduced with permission from Morrison, G. W.; Menard, M. C.; Treadwell, L. J.; Haldolaarachchige, N.; Kendrick, K. C.; Young, D. P.; Chan, J. Y., *Philos. Mag.* **2012,** *92*, 2524-2540. Copyright 2012 Taylor & Francis.
http://www.tandfonline.com/doi/full/10.1080/14786435.2012.669063

reaction. This silica is then reduced by the molten aluminium flux to produce silicon metal and alumina.[3.1] While this is typically an undesirable result, an insidious entrance of silicon into the reaction can often lead to the serendipitous growth of aluminium silicide phases which may not be stabilized without silicon.[3.2] Herein, the synthesis, structure and properties of two competing metal silicide phases, $Ru_{23}(Al,Si)_{97}$ and $CeRu_4(Al,Si)_{15.5}$ are reported.

### 3.2 Experimental

The reactant metals, in the form of powders, rods, or pellets of 99.9% purity or greater, are used as received and weighed in the desired reaction ratio. The metals are placed in an alumina crucible as per the self-flux method. Several reviews providing detailed descriptions of the flux method are reported elsewhere,[3.3, 4] and therefore, the details of this method will not be discussed here. The reaction ratio and temperature profile are varied to determine the variables affecting phase formation and crystal size. Adjustable variables include the heating/cooling rates, dwell times at high/low temperatures, dwell temperatures, and spin temperatures.

The separation of single crystals from excess flux requires great care in the selection of the etching medium. Dilute HCl is used as the etching which is unusual, as typically NaOH is used as the etching agent, since the base often reacts with aluminium with minimal degradation of the crystals. [3.3, 4] However, in this case of $Ru_{23}(Al,Si)_{97}$, the use of NaOH as an etching agent led to faster degradation of the crystal than did HCl.

Once single crystals are separated, their structures are characterized by single crystal X-ray diffraction (XRD) using a Nonius KappaCCD diffractometer equipped with a Mo $K_\alpha$ source ($\lambda$ = 0.711 Å). The elemental compositions of the crystals are analysed with energy dispersive spectroscopy (EDS) using an EDAX detector equipped to a FEI Quanta 200 or a Hitachi S-3600N scanning electron microscope. Composition, structure and sample homogeneity of polycrystalline

samples are determined via powder XRD using a Bruker AXS D8 Advance diffractometer with a Cu $K_\alpha$ source ($\lambda$ = 1.541 Å).

Temperature-dependent magnetic susceptibility ($\chi$) of single crystals are measured from 3 - 265 K at $H$ = 0.1 T using a Quantum Design Physical Property Measurement System (PPMS). Field-dependent magnetization of samples is generally measured from 0 T - 9 T at 3 K. Specific heat is measured using the thermal relaxation option of the PPMS down to 0.4 K. Temperature-dependent electrical resistance is measured down to 3 K using the four-probe method. Magnetoresistance is measured at 3 K in fields up to 9 T.

### 3.3 $Ru_{23}(Al,Si)_{97}$

$Ru_{23}(Al,Si)_{97}$ is a highly stable phase which grows in a wide range of reactions compositions. Large, phase pure, single crystals were synthesized by using a Ru:Al:Si ratio of 23:400:55.6 (12% Si in Al). The reaction was dwelled at 1050 °C for 24 h before slow cooling at a rate of 10 °C/h to 720 °C, at which temperature the reaction was spun. This reaction profile resulted in two large single crystals, shown in Figure 3.1, each of which was approximately 5 mm on each side. EDS analysis of the crystals indicated an elemental composition of $Ru_{23.0(12)}Al_{83.0(6)}Si_{9.6(12)}$.

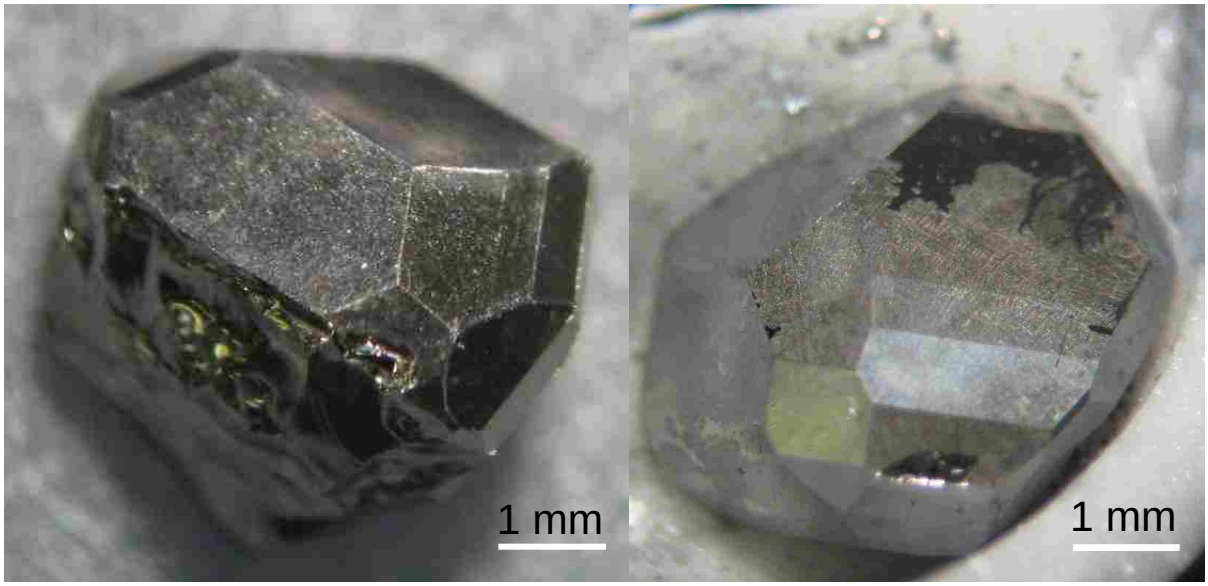


**Figure 3.1** Two crystals of $Ru_{23}(Al,Si)_{97}$.

The percent Si in the compound can be varied by changing the Si to Al ratio in the reaction. When a Ru:Al:Si ratio of 23:400:26 (6% Si in Al) was used with the same heating profile, very poor quality crystals were formed. By dwelling at 1150 °C instead of 1050 °C, single crystals with a stoichiometry, determined by EDS analysis, of $Ru_{23.0(9)}Al_{86.3(4)}Si_{8.6(9)}$ or 9.1(10)% Si were obtained. When a Ru:Al:Si ratio of 23:400:129.2 (24% Si in Al) was used with the original heating profile, single crystals with a stoichiometry of $Ru_{23.0(2)}Al_{83.4(4)}Si_{15.3(4)}$ or 15.5(4)% Si were grown. The large amount of Si used in this reaction led to the growth of Si crystals intermingled with the $Ru_{23}(Al,Si)_{97}$ crystals. However, the two are easily distinguished by morphology, Si grows plates as opposed to polyhedra, and Si is darker grey in colour than $Ru_{23}(Al,Si)_{97}$. While the uncertainty in the EDS data is too high to show clear evidence that different amounts of Si are present in the crystals of each growth, this can be seen by single crystal XRD. As shown in the Table 3.1, when the Si concentration in $Ru_{23}(Al,Si)_{97}$ is increased, the unit cell lattice parameters decrease. This is expected as Si has a smaller covalent radius than Al.

$Ru_{23}(Al,Si)_{97}$ is a new member of the α-(AlFeSi) structure type[3.5] and crystallizes in the hexagonal space group $P6_3/mmc$ with dimensions $a$ = 12.6490(5) Å and $c$ = 26.7560(10) Å. Tables of crystallographic data, atomic positions, interatomic distances, and figures of the structure can be found in Tables 3.1-3 and Figure 3.2, respectively. $Ru_{23}(Al,Si)_{97}$ varies from α-(AlFeSi) in that the latter has three positionally disordered and 15 ordered Al/Si sites, whereas the prior has 17 completely occupied Al/Si sites. Due to the similarity between Al and Si electron densities, the Al and Si atoms could not be distinguished by XRD. Since it is unclear whether Si is statistically distributed across all of the Al sites or is localized on a smaller number of sites, the final structural model was refined with only Al atoms. While single crystals large enough for neutron diffraction

have been grown, recent evidence suggests that Al and Si cannot be distinguished by neutron diffraction either.[3.6]

**Table 3.1** Crystallographic Data of $Ru_{23}(Al,Si)_{97}$

| **Crystal data** | | | |
|---|---|---|---|
| Composition | $Ru_{23}Al_{88.2}Si_{8.8}$ | $Ru_{23}Al_{86.9}Si_{10.1}$ | $Ru_{23}Al_{82.0}Si_{15.0}$ |
| Space group | $P6_3/mmc$ | $P6_3/mmc$ | $P6_3/mmc$ |
| $a$ (Å) | 12.6523(10) | 12.6395(10) | 12.6138(15) |
| $c$ (Å) | 26.752(3) | 26.748(3) | 26.696(4) |
| $V$ (Å$^3$) | 3708.8(6) | 3700.6(6) | 3678.5(8) |
| $Z$ | 2 | 2 | 2 |
| Crystal size (mm$^3$) | 0.05 x 0.10 x 0.13 | 0.05 x 0.013 x 0.013 | 0.03 x 0.07 x 0.07 |
| **Data Collection** | | | |
| Temperature (K) | 298(2) | 298(2) | 298(2) |
| Measured reflections | 11745 | 11649 | 14343 |
| Independent reflections | 2256 | 2250 | 2242 |
| Reflections with I > 2$\sigma$(I) | 1851 | 1841 | 1702 |
| $R_{int}$ | 0.0589 | 0.0627 | 0.0953 |
| $h$ | -18 → 18 | -18 → 18 | -18 → 17 |
| $k$ | -15 → 15 | -15 → 15 | -15 → 15 |
| $l$ | -24 → 38 | -38 → 24 | -38 → 38 |
| **Refinement** | | | |
| $\theta$ range (˚) | 1.00-31.00 | 1.00-31.00 | 1.00-31.00 |
| $^aR_1[F^2 > 2\sigma F^2)]$ | 0.0235 | 0.0248 | 0.0326 |
| $^bwR_2(F^2)$ | 0.0493 | 0.0518 | 0.0551 |
| Parameters | 122 | 122 | 122 |
| GooF on $F^2$ | 1.047 | 1.043 | 1.027 |
| $\mu$ (mm$^{-1}$) | 5.713 | 5.725 | 5.760 |
| $\Delta p_{max}$ (e Å$^{-3}$) | 0.956 | 1.117 | 0.993 |
| $\Delta p_{min}$ (e Å$^{-3}$) | -0.929 | -1.016 | -1.321 |
| Extinction coefficient | 0.00115(3) | 0.000136(4) | 0.00083(3) |

$^aR_1 = \Sigma||F_0| - |F_c||/\Sigma|F_0|$

$^bwR_2 = [\Sigma w(F_o^2 - F_c^2)^2/\Sigma w(F_0^2)^2]^{1/2}$; $P = (F_o^2 + 2F_c^2)/3$; $w = 1/[\sigma^2(F_o^2) + (0.0197P)^2 + 4.7574P]$, $w = 1/[\sigma^2(F_o^2) + (0.0235P)^2 + 2.7873P]$, and $w = 1/[\sigma^2(F_o^2) + (0.0193P)^2 + 7.2046P]$ for 9.1 %, 10.4 % and 15.5 % Si analogues, respectively

**Table 3.2** Atomic Positional and Displacement Parameters for $Ru_{23}Al_{86.9}Si_{10.1}$

| Atom | Wyckoff site | *x* | *y* | *z* | $U_{eq}$ (Å$^2$)[a] |
|---|---|---|---|---|---|
| Ru(1) | 12*k* | 0.538546(15) | 0.07709(3) | 0.837391(14) | 0.00664(8) |
| Ru(2) | 12*k* | 0.129206(15) | 0.25821(3) | 0.648949(15) | 0.00733(8) |
| Ru(3) | 12*k* | 0.212892(15) | 0.42578(3) | 0.030155(13) | 0.00692(8) |
| Ru(4) | 6*h* | 0.21134(2) | 0.42268(4) | ¼ | 0.00600(10) |
| Ru(5) | 4*f* | ⅓ | ⅔ | 0.60011(2) | 0.00689(12) |
| M(1)[b] | 24*l* | 0.34583(9) | 0.29235(9) | 0.89706(4) | 0.0105(2) |
| M(2) | 24*l* | 0.32731(8) | 0.33525(8) | 0.80164(4) | 0.00870(19) |
| M(3) | 12*i* | 0.37481(11) | 0 | 0 | 0.0113(3) |
| M(4) | 12*k* | 0.10696(6) | 0.21393(11) | 0.01690(5) | 0.0058(2) |
| M(5) | 12*k* | 0.40395(6) | 0.80790(11) | 0.51678(6) | 0.0083(3) |
| M(6) | 12*k* | 0.45386(6) | 0.90772(12) | 0.89642(6) | 0.0109(3) |
| M(7) | 12*k* | 0.08373(6) | 0.16746(13) | 0.33199(6) | 0.0110(3) |
| M(8) | 12*k* | 0.59627(6) | 0.19253(12) | 0.91831(6) | 0.0104(3) |
| M(9) | 12*k* | 0.20258(6) | 0.40515(12) | 0.93205(6) | 0.0102(3) |
| M(10) | 12*k* | 0.06790(6) | 0.13580(11) | 0.92540(5) | 0.0079(3) |
| M(11) | 12*k* | 0.24891(7) | 0.49783(13) | 0.32718(6) | 0.0138(3) |
| M(12) | 12*k* | 0.24986(6) | 0.49971(13) | 0.83660(6) | 0.0158(3) |
| M(13) | 6*h* | 0.58333(9) | 0.16666(17) | ¼ | 0.0132(4) |
| M(14) | 6*h* | 0.84056(8) | 0.68112(17) | ¼ | 0.0065(4) |
| M(15) | 6*h* | 0.09013(9) | 0.18025(18) | ¼ | 0.0126(4) |
| M(16) | 6*h* | 0.45649(8) | 0.91297(17) | ¼ | 0.0127(4) |
| M(17) | 2*c* | ⅓ | ⅔ | ¼ | 0.0114(7) |

[a] $U_{eq}$ is defined as one-third of the trace of the orthogonalized $U_{ij}$ tensor.
[b] M = Al/Si

**Table 3.3** Select interatomic distances in $Ru_{23}(Al,Si)_{97}$

| | | | |
|---|---|---|---|
| Ru(1)-Al(1) (x2) | 2.8005(10) | Ru(3)-Al(1) (x2) | 2.6143(11) |
| Ru(1)-Al(2) (x2) | 2.5156(10) | Ru(3)-Al(3) (x2) | 2.5637(4) |
| Ru(1)-Al(6) | 2.4352(15) | Ru(3)-Al(4) | 2.3460(13) |
| Ru(1)-Al(8) | 2.5062(15) | Ru(3)-Al(5) (x2) | 2.6158(8) |
| Ru(1)-Al(11) (x2) | 2.4847(4) | Ru(3)-Al(8) (x2) | 2.6766(9) |
| Ru(1)-Al(13) | 2.5348(9) | Ru(3)-Al(9) | 2.6338(16) |
| Ru(1)-Al(16) | 2.9481(12) | | |
| | | Ru(4)-Al(2) (x4) | 2.6264(10) |
| Ru(2)-Al(1) (x2) | 2.8324(10) | Ru(4)-Al(12) (x2) | 2.4649(16) |
| Ru(2)-Al(2) (x2) | 2.5557(10) | Ru(4)-Al(15) | 2.654(2) |
| Ru(2)-Al(7) (x2) | 2.5353(5) | Ru(4)-Al(16) (x2) | 2.6835(10) |
| Ru(2)-Al(9) | 2.6983(15) | Ru(4)-Al(17) | 2.6707(5) |
| Ru(2)-Al(10) | 2.3980(15) | | |
| Ru(2)-Al(12) | 2.6716(15) | Ru(5)-Al(5) (x3) | 2.7126(16) |
| Ru(2)-Al(15) | 2.8344(8) | Ru(5)-Al(6) (x3) | 2.6402(13) |
| | | Ru(5)-Al(9) (x3) | 2.9890(14) |
| | | Ru(5)-Al(12) (x3) | 2.4911(15) |

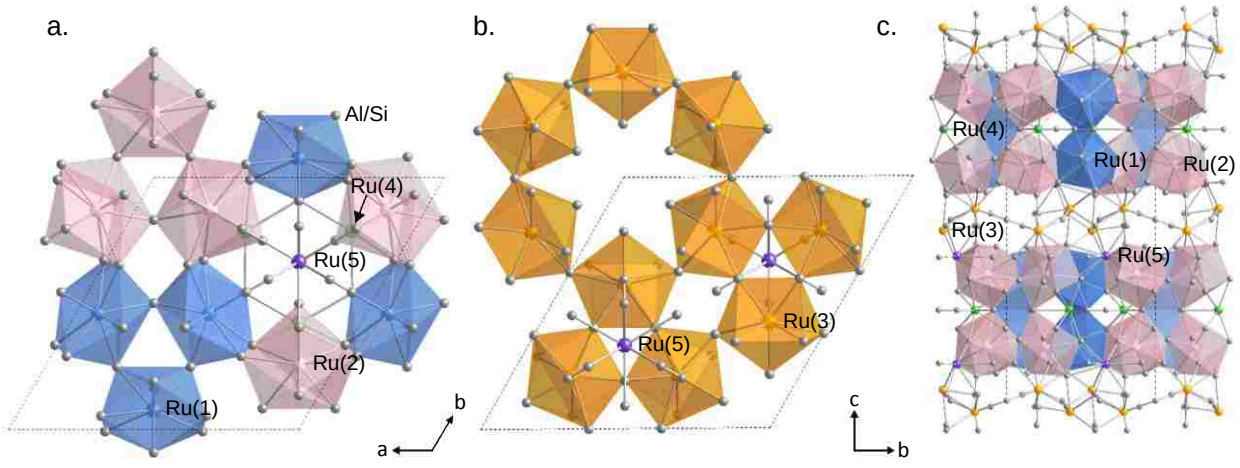


**Figure 3.2** Structure of $Ru_{23}(Al,Si)_{97}$ showing (a) the Ru1, Ru2, Ru4 slab, (b) the Ru3 slab and (c) the stacking of the two slabs with the Ru5 atoms laying in between. Ru4 and Ru5 polyhedra are not shown for clarity.

### 3.4 $CeRu_4(Al,Si)_{15.58}$

While attempting to grow single crystals of a Ce:Ru:Al phase, a sample was prepared with a Ce:Ru:Al ratio of 2:3:18 and was heated to 1200 °C for 24 h. A single crystal approximately 0.3 cm on each side was obtained from this growth. Single crystal XRD found this crystal to be a new phase, $CeRu_4(Al,Si)_{15.58}$. EDS analysis found the composition of this crystal to be $Ce_{1.00(10)}Ru_{3.59(14)}Al_{9.7(2)}Si_{4.5(2)}$. In order to grow this phase, silica wool must have entered the reaction during the growth.

The synthesis of $CeRu_4(Al,Si)_{15.58}$ is difficult due to the stability of $Ru_{23}(Al,Si)_{97}$. Several attempts were made to flux grow $CeRu_4(Al,Si)_{15.58}$ using the self-flux method while avoiding the growth of the pseudo-binary. Initially, the isolated growth of $CeRu_4(Al,Si)_{15.58}$ was attempted by varying the Si to Al ratio in the reaction. As $CeRu_4(Al,Si)_{15.58}$ has 31% Si and $Ru_{23}(Al,Si)_{97}$ has only 12% Si, increasing the Si concentration was expected to favour the growth of the quaternary phase. Multiple growths were carried out with a Ce:Ru:Al:Si ratio of 1:4:32:X (X = varying amounts of silicon) in which the reaction was heated to 1200 °C for 24 h before slow cooling to 720 °C at 5 °C/h. At low Si concentrations, circa 12%, only $Ru_{23}(Al,Si)_{97}$ forms. When the Si concentration is increased to near 33%, a mixture of the two phases results. However, a large amount of Si also precipitates out of the reaction making the separation of the crystals very difficult. Further increasing the Si concentration to 42% prevents the growth of the pseudo-binary. However, due to the very high Si concentration, only Si single crystals were visible in the growth, with $CeRu_4(Al,Si)_{15.58}$ being a poor quality polycrystalline material. Next, instead of increasing the Si concentration, the Ce concentration was increased while keeping the Si close to its maximum soluble concentration at 720 °C (22%). A reaction with a Ce:Ru:Al:Si ratio of 2:4:32:9.63 and the

heating scheme discussed above did not yield any of the desired $CeRu_4(Al,Si)_{15.58}$. Further increasing the Ce ratio was not attempted as to avoid the precipitation of $Ce_3Al_{11}$.

As changing the reaction ratio did not appear to lead to phase pure $CeRu_4(Al,Si)_{15.58}$, the next step was to change the reaction profile. The previously reported analogues of this structure type were all grown at lower dwell temperatures with longer dwell times.[3.7, 8] A reaction was prepared with a Ce:Ru:Al:Si ratio of 1:4:20:5, similar to the ratio used for the Fe analogues.[3.8] This reaction was dwelled at 850 °C for 4 days before being slow cooled at 5 °C/h. Lowering the dwell temperature and increasing the time did not yield the desired product but instead grew $Ru_{23}(Al,Si)_{97}$.

One final flux growth route which was attempted involved the pre-alloying of Ce with another element in order to kinetically favour the growth of $CeRu_4(Al,Si)_{15.58}$ over $Ru_{23}(Al,Si)_{97}$. Ce:Ru ratios of 1:2 and 1:4 were arc-melted together and the resulting alloy was added to Al and Si such that the Ru:Al:Si ratio was 4:32:5. Using the initial heating scheme, these reactions yielded $Ru_{23}(Al,Si)_{97}$ and other binary or psuedobinary phases but no $CeRu_4(Al,Si)_{15.58}$. Similarly, the pre-alloying of Ce and Al did not result in the desired product but instead grew multiple RuSi phases.

While the flux growth method is often a very good technique to grow phase pure crystals, it is not always the best or even a viable method. Following the failure of both changing the reaction ratio and reaction profile to yield phase pure $CeRu_4(Al,Si)_{15.58}$, a polycrystalline growth was attempted via arc melting. This phase was arc melted on stoichiometry using chunks or pellets of each element. The resulting button was turned over and remelted two times to ensure homogeneity. The resulting mass loss was less than 0.5%. Following the arc melting, powder XRD indicated a small impurity of $CeSi_{2-x}$. This impurity persisted after annealing for 2.5 days at 800 °C. Further annealing at 850 °C for two weeks decreased the amount of $CeSi_{2-x}$ by

approximately half but also led to the formation of a similar amount of $RuAl_2$. In an attempt to remove both impurities, the button was then annealed at 1150 °C, which is above the melting point of $RuAl_2$, for one week. However, this lead to the complete decomposition of $CeRu_4(Al,Si)_{15.58}$ into several binary phases.

$CeRu_4(Al,Si)_{15.58}$ is a new member of the $NdRh_4Al_{15.37}$ structure type[3.7] and crystallizes in the tetragonal space group $P4_2/nmc$ with the dimensions $a$ = 8.9690(5) Å and $c$ = 15.7050(10) Å. Two $LnFe_4Al_9Si_6$ ($Ln$ = Tb, Er) analogues have also been reported for this structure type.[3.8] As with $Ru_{23}(Al,Si)_{97}$, the Al and Si atoms could not be distinguished by XRD, and therefore, the structural model was refined with only Al atoms. Figures and tables of crystallographic data, atomic positions, and interatomic distances can be found in Figure 3.3 and Tables 3.4-6, respectively.

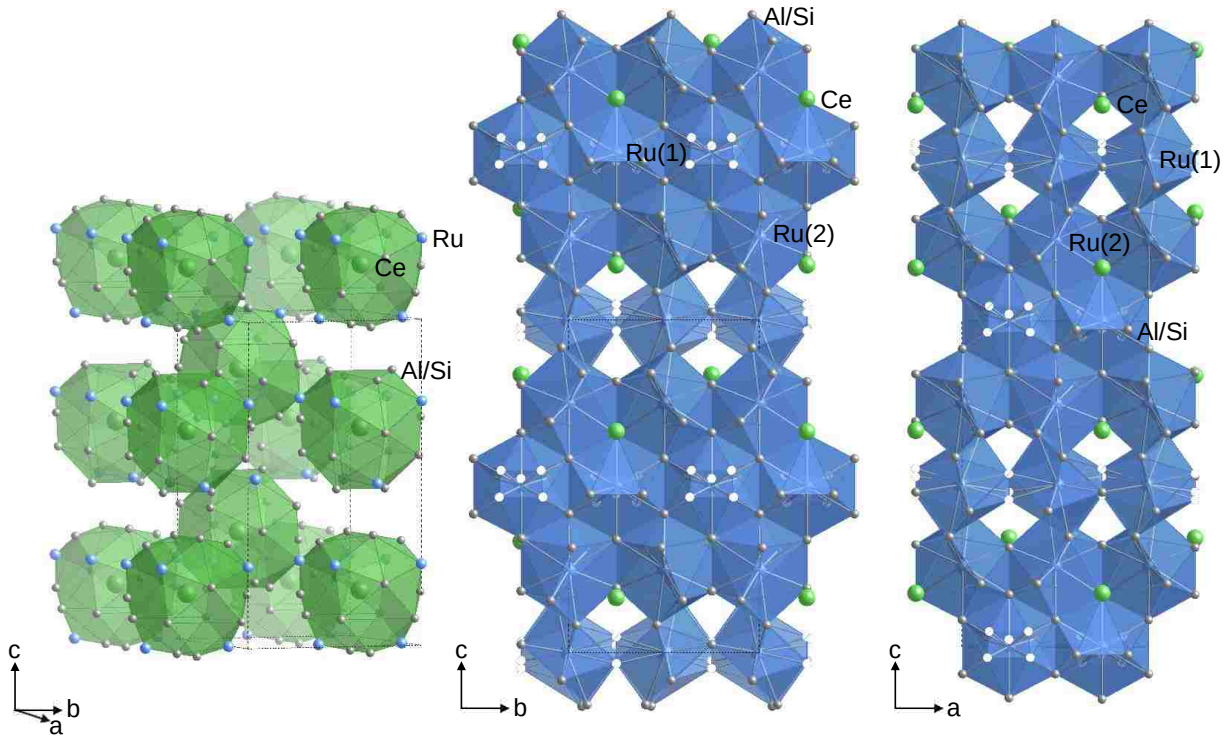


**Figure 3.3** Structure of $CeRu_4(Al,Si)_{15.58}$ showing (a) the Ce environment, (b and c) the Ru polyhedra viewed down the $x$ and $y$ axes, respectively, to emphasize the channels in which the Ce lie.

**Table 3.4** Crystallographic Data of $CeRu_4(Al,Si)_{15.58}$

| **Crystal data** | |
|---|---|
| Composition | $CeRu_4Al_{10.63}Si_{4.95}$ |
| Space group | $P4_2/nmc$ |
| $a$ (Å) | 8.9690(5) |
| $c$ (Å) | 15.7050(10) |
| $V$ (Å$^3$) | 1263.36(13) |
| $Z$ | 4 |
| Crystal size (mm$^3$) | 0.10 x 0.13 x 0.13 |
| **Data Collection** | |
| Temperature (K) | 298(2) |
| Measured reflections | 7532 |
| Independent reflections | 1121 |
| Reflections with I > 2$\sigma$(I) | 1053 |
| $R_{int}$ | 0.0203 |
| $h$ | -12 → 12 |
| $k$ | -12 → 12 |
| $l$ | -22 → 22 |
| **Refinement** | |
| $\theta$ range (˚) | 2.62-31.00 |
| $^aR_1[F^2 > 2\sigma F^2)]$ | 0.0171 |
| $^bwR_2(F^2)$ | 0.0405 |
| Parameters | 75 |
| GooF on $F^2$ | 1.231 |
| $\mu$ (mm$^{-1}$) | 9.266 |
| $\Delta p_{max}$ (e Å$^{-3}$) | 1.141 |
| $\Delta p_{min}$ (e Å$^{-3}$) | -1.008 |
| Extinction coefficient | 0.00300(9) |

$^aR_1 = \Sigma||F_0| - |F_c||/\Sigma|F_0|$
$^bwR_2 = [\Sigma w(F_o^2 - F_c^2)^2/\Sigma w(F_0^2)^2]^{1/2}$; $P = (F_o^2 + 2F_c^2)/3$; $w = 1/[\sigma^2(F_o^2) + (0.0106P)^2 + 4.4120P]$

$NdRh_4Al_{15.37}$ contains two Rh sites, the Rh1 site, which is coordinated by eight fully-occupied and three partially-occupied Al atoms, and the Rh2 site, which is coordinated by 10 Al atoms in a distorted pentagonal antiprism.[3.7] $CeRu_4(Al,Si)_{15.58}$ has similar disorder of the Al atoms around the Ru1 site. The Ru1 atoms are coordinated by eight ordered aluminium atoms along with five disordered aluminium atoms (Al7, Al8 and Al9). The eight ordered aluminium atoms along with the two Al7 atoms form a distorted pentagonal antiprism. The two Al8 atoms and the Al9 atom lie above the Al7 atoms. The Al7, Al8 and Al9 atoms have occupancies of 29.6(6)%,

**Table 3.5** Atomic Positional and Displacement Parameters for $CeRu_4(Al,Si)_{15.58}$

| Atom | Wyckoff site | *x* | *y* | *z* | Occ.[a] | $U_{eq}$ (Å$^2$)[b] |
|---|---|---|---|---|---|---|
| Ce(1) | 4*d* | ¼ | ¼ | 0.334900(17) | 1.00 | 0.00607(8) |
| Ru(1) | 8*g* | ¼ | 0.48983(3) | 0.001175(17) | 1.00 | 0.00936(8) |
| Ru(2) | 8*f* | 0.50104(2) | 0.49896(2) | ¾ | 1.00 | 0.00588(8) |
| Al(1) | 16*h* | 0.46234(12) | 0.49966(9) | 0.41687(5) | 1.00 | 0.01553(18) |
| Al(2) | 8*g* | ¼ | 0.01512(12) | 0.68508(7) | 1.00 | 0.00636(19) |
| Al(3) | 8*g* | ¼ | 0.06838(13) | 0.16103(7) | 1.00 | 0.0094(2) |
| Al(4) | 8*g* | ¼ | 0.38945(15) | 0.52425(7) | 1.00 | 0.0142(2) |
| Al(5) | 8*g* | ¼ | 0.59714(12) | 0.30621(7) | 1.00 | 0.00704(19) |
| Al(6) | 8*g* | ¼ | 0.59648(13) | 0.84339(8) | 1.00 | 0.0137(2) |
| Al(7) | 8*g* | ¼ | 0.6351(4) | 0.5329(2) | 0.296(6) | 0.0105(12) |
| Al(8) | 8*g* | ¼ | 0.6453(5) | 0.4519(3) | 0.281(7) | 0.0164(15) |
| Al(9) | 4*c* | ¾ | ¼ | 0.5231(3) | 0.430(10) | 0.0155(15) |

[a]Occupancy

[b]$U_{eq}$ is defined as one-third of the trace of the orthogonalized $U_{ij}$ tensor.

**Table 3.6** Select interatomic distances in $CeRu_4(Al,Si)_{15.58}$

| | | | |
|---|---|---|---|
| Ce(1)-Ru(1) (x2) | 3.3832(17) | Ru(1)-Al(4) (x2) | 2.5145(8) |
| Ce(1)-Ru(2) (x4) | 3.4400(2) | Ru(1)-Al(6) | 2.6562(16) |
| Ce(1)-Al(1) (x4) | 3.2091(9) | Ru(1)-Al(7) (x2) | 2.6066(17) |
| Ce(1)-Al(2) (x2) | 3.1582(11) | Ru(1)-Al(8) (x2) | 2.6208(19) |
| Ce(1)-Al(3) (x2) | 3.1796(11) | Ru(1)-Al(9) | 2.3587(7) |
| Ce(1)-Al(4) (x2) | 3.2261(12) | | |
| Ce(1)-Al(5) (x2) | 3.1460(11) | Ru(2)-Al(1) (x2) | 2.6413(8) |
| Ce(1)-Al(6) (x2) | 3.1104(12) | Ru(2)-Al(2) (x2) | 2.4749(5) |
| | | Ru(2)-Al(3) (x2) | 2.7066(6) |
| Ru(1)-Al(1) (x4) | 2.6130(8) | Ru(2)-Al(5) (x2) | 2.5511(6) |
| Ru(1)-Al(3) | 2.5642(11) | Ru(2)-Al(6) (x2) | 2.8259(8) |

28.1(7)% and 43.0(10)%, respectively. The above occupancies, along with bond distances, suggest that either the Al9 atom is present or a nonadjacent pair of Al7 and Al8 atoms is present in each Ru1 polyhedron. Based on the uncertainties in the occupancies of the three sites, the formula becomes $CeRu_4(Al,Si)_{15.58(3)}$.

Each cerium atom is surrounded by 14 aluminium and six ruthenium atoms. These polyhedra are similar in structure to the cerium polyhedra found within $CeRu_2Al_{10}$[3.9] and $Ce_2Ru_3Al_{15}$.[3.10] Unlike in these previously reported structures, the Ce polyhedra do not form face-sharing columns. Instead, they are corner sharing through Ru2 atoms. The Ce-Ce distance between vertically stacked cerium atoms is 7.8525(6) Å. The closest Ce-Ce interaction is actually between diagonally adjacent cerium polyhedral which are separated by 6.8798(18) Å and have a Ru2 atom located at their centroid.

The stability of this phase has been explained by considering the valence electron density. $NdRh_4Al_{15.37}$ has 85.11 valence electrons per formula unit. $LnFe_4Al_9Si_6$ (*Ln* = Er, Tb) has a similar valence electron concentration with 86 valence electrons per formula unit.[3.8] The $NdRh_4Al_{15.37}$ structure type being a valence electron count stabilized phase provides an explanation for why the iron analogue contains silicon. As Rh has one more valence electron than the iron analogue, silicon provides the extra valence electrons which are required to bring the electron density to the required level. This can also be seen in $CeRu_4(Al,Si)_{15.58}$ where the ~31% silicon brings the valence electron density to 86.69 valence electrons per formula unit (Ce: 3; Ru: 8; Al: 3; Si: 4).

Figure 3.4a shows the temperature-dependent magnetic susceptibility at 0.1 T for a sample of $CeRu_4(Al,Si)_{15.58}$ that was arc melted and annealed at 800 °C. Fitting with a modified Curie-Weiss law, $\chi = \chi_o + C/(T - \theta)$, from 50 to 200 K, $\chi_0$ = 0.00107(5) emu/mol-Ce and $\theta$ = -21.9(14) K. An effective moment of 1.93(2) $\mu_B$/Ce is calculated from the data and is smaller

than the 2.54 $\mu_B$ expected for $Ce^{3+}$. The inverse susceptibility, shown in the inset, displays a ferromagnetic transition at about 13 K. This transition is not accompanied by the large increase in susceptibility which is typically expected for ferromagnetic transitions. Instead, the susceptibility only reaches 0.12 emu/mol-Ce at 3 K. Furthermore, the magnetization as a function of field, shown in Figure 3.4b, only shows a very small hysteresis loop. These two characteristics, coupled with the negative Weiss temperature, suggest that $CeRu_4(Al,Si)_{15.58}$ is paramagnetic and that the slight ferromagnetic behaviour arises due to the $CeSi_{2-x}$ impurity, which is ferromagnetic for $x$ between 0.2 and 0.3 with $T_c \approx 10$ K.[3.11] Paramagnetic behaviour down to 3 K is expected for $CeRu_4(Al,Si)_{15.58}$ as the closest Ce-Ce contacts are 6.8798(18) Å. This is in agreement with other Ce containing compounds with large Ce-Ce distances.[3.12] This is also in agreement with $LnFe_4Al_9Si_6$ ($Ln$ = Tb, Er) which were both found to be paramagnetic.[3.8] The presence of a ferromagnetic impurity in the arc-melted sample highlights one of the advantages single crystals offer over polycrystalline samples.

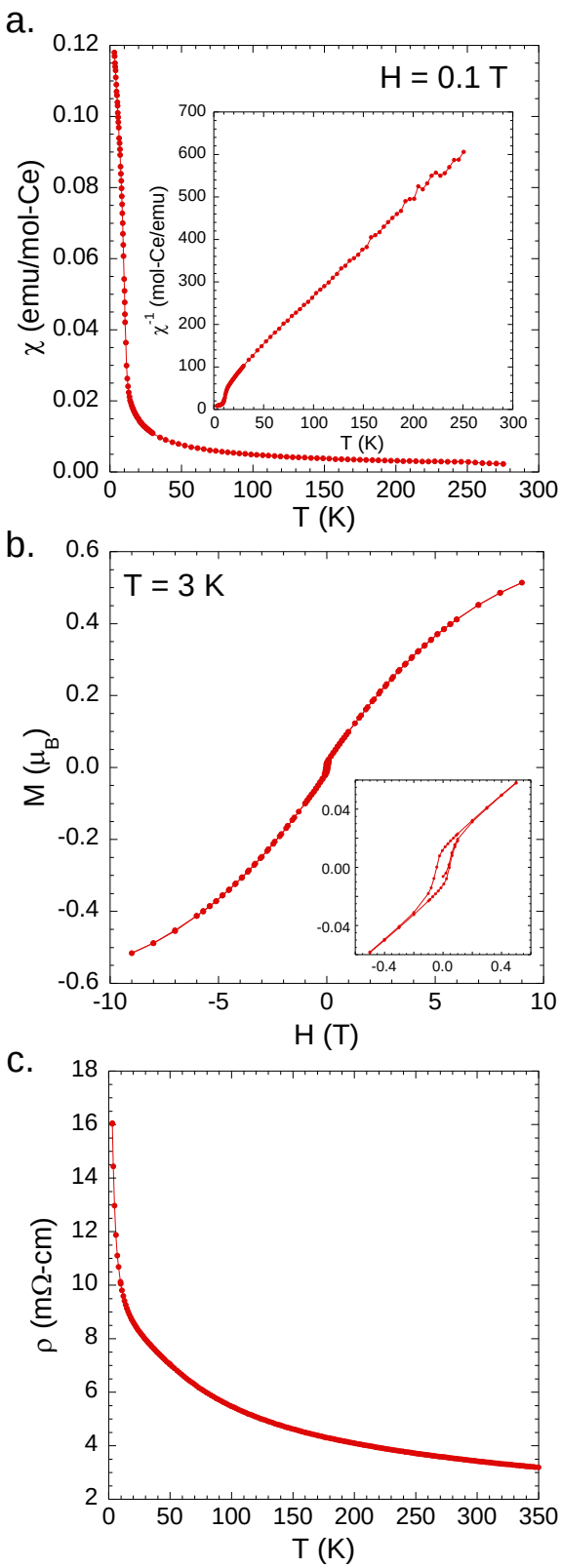


**Figure 3.4** Physical properties of $CeRu_4(Al,Si)_{15.58}$.

The resistivity of the single crystal of $CeRu_4(Al,Si)_{15.58}$, shown in Figure 3.4c, displays semiconducting-like behaviour. While negative in slope, the high temperature region of the resistivity does not follow the activated behaviour ($\rho = \rho_o e^{-E_G/2kT}$) which is expected for semiconductors.

## 3.7 Conclusions

The self-flux technique offers a great deal of control over reaction conditions in crystal growth experiments. This control is especially important when two or more competing phases exist within a phase space. The ability to control elements such as reactant ratio, dwell temperature, cooling rate and spin temperature often allows for the selective growth of one compound over another. While the self-flux method is not always the best method, and sometimes not even a viable method, for the growth of a phase, it is a simple, highly versatile technique which should always be considered. One case in which the self-flux method is especially useful is in the synthesis of aluminium silicides. The high solubility of silicon in aluminium, along with the lack of any ordered binaries within either phase space, makes these phases ideal candidates for the self-flux technique.

## 3.8 References


3.1. Brondyke, K. J., *J. Am. Ceram. Soc.* **1953,** *36*, 171-174.

3.2. Phelan, W. A.; Kangas, M. J.; Drake, B. L.; Zhao, L. L.; Wang, J. K.; DiTusa, J. F.; Morosan, E.; Chan, J. Y., *Inorg. Chem.* **2012,** *51*, 920-927.

3.3. Canfield, P. C.; Fisk, Z., *Philos. Mag. B* **1992,** *65*, 1117-1123.

3.4. Kanatzidis, M. G.; Rainer, P.; Jeitschko, W., *Angew. Chem. Int. Ed. Engl.* **2005,** *44*, 6996-7023.

3.5. Corby, R. N.; Black, P. J., *Acta Crystallogr. Sect. B* **1977,** *33*, 3468-3475.

3.6. Roudebush, J. H.; de la Cruz, C.; Chakoumakos, B. C.; Kauzlarich, S. M., *Inorg. Chem.* **2011,** *51*, 1805-1812.

3.7. Fehrmann, B.; Jeitschko, W., *J. Alloys Compd.* **2000,** *298*, 153-159.

3.8. Sieve, B.; Gray, D. L.; Henning, R.; Bakas, T.; Schultz, A. J.; Kanatzidis, M. G., *Chem. Mater.* **2008,** *20*, 6107-6115.

3.9. Niemann, S.; Jeitschko, W., *Z. Krist.* **1995,** *210*, 338-341.

3.10. Tursina, A. I.; Murashova, E. V.; Nesterenko, S. N.; Chernyshev, I. V.; No; l, H.; Seropegin, Y. D., *Acta Crystallogr. Sect. E* **2004,** *60*, i145-i146.

3.11. Yashima, H.; Satoh, T., *Solid State Commun.* **1982,** *41*, 723-727.

3.12. Julián G, S., Low-temperature behaviour of cerium compounds: Specific heat of binary and related intermetallics. In *Handbook on the Physics and Chemistry of Rare Earths*, Karl A. Gschneidner, Jr.; LeRoy, E., Eds. Elsevier: New York, 1991; Vol. 15, p 1.

## Chapter 4.[†] Synthesis, Structure, and Properties of $Ln_2Ru_3Al_{15}$ (*Ln* = Ce, Gd): A Comparison with $LnRu_2Al_{10}$ and $CeRu_4(Al,Si)_{15.58}$

### 4.1 Introduction

$CeRu_2Al_{10}$, a member of the $YbFe_2Al_{10}$ structure type,[4.1] has received attention because it exhibits a metal-to-insulator transition and orders at 27 K,[4.2] higher than the 16 K antiferromagnetic (AFM) ordering of $GdRu_2Al_{10}$.[4.3] Single crystal neutron scattering data indicates that the magnetic ordering is AFM with a (1,0,0) propagation vector[4.4] and a reduced moment of 0.34(2) $\mu_B$/Ce at 1.5 K.[4.5] Furthermore, the magnetic susceptibility displays a large degree of anisotropy.[4.6] Both the anisotropy and the reduced moment can be attributed to crystal electric field splitting,[4.7] where the first two splitting terms have been calculated to be 500 K and 760 K.[4.8] While the AFM ordering has been well characterized, its origin remains in question. Two possible explanations for the ordering are a charge density wave formation[4.9] or a Spin-Peierls transition.[4.10] Recently, a computational study[4.11] on $CeRu_2Al_{10}$ suggested that the atoms in the Ce polyhedra are shifted from the lowest energy state structure by about 0.025 Å. Magnetic calculations on the computationally relaxed structure found it to have a non-magnetic ground state, while calculations on the actual structure resulted in a competition between non-magnetic and AFM states. This suggests that the Ce polyhedra are important to the low temperature properties of $CeRu_2Al_{10}$.[4.11]

In an effort to explore the relationship between the structure and the properties of $CeRu_2Al_{10}$, we have studied the effect of the rare earth on the properties of $LnRu_2Al_{10}$ (*Ln* = lanthanide).[4.12] $PrRu_2Al_{10}$ displays paramagnetic behavior down to 13.2 K, when it enters a nonmagnetic singlet ground state due to crystal electric field splitting of the *f* orbitals, and has a

[†]Reproduced with permission from Morrison, G.; Haldolaarachchige, N.; Chen, C.-W.; Young, D. P.; Morosan, E.; Chan, J. Y., *Inorg. Chem.* **2013,** *52,* 3198-3206. Copyright 2013 American Chemical Society.

large paramagnetic Curie-Weiss temperature of -49.8(14) K. $GdRu_2Al_{10}$ was found to order antiferromagnetically at 15.5 K with $\theta_N$ = -15.45(8) K. $YbRu_2Al_{10}$ is a Pauli paramagnet, indicating that Yb is in its divalent state. All three analogues display metallic behavior, although $GdRu_2Al_{10}$ is a poor metal with a resistivity on the order of 1 mΩ-cm.[4.12]

In order to further explore the role of the structure of $CeRu_2Al_{10}$ on the properties we have grown $CeRu_4(Al,Si)_{15.58}$, a member of the $NdRh_4Al_{15.37}$ structure type,[4.13] which contains Ce polyhedra that closely resemble the Ce environment in $CeRu_2Al_{10}$. However, instead of the face-sharing columns seen in $CeRu_2Al_{10}$, the polyhedra in $CeRu_4(Al,Si)_{15.58}$ form corner-sharing sheets. $CeRu_4(Al,Si)_{15.58}$ follows a Curie-Weiss law with $\theta$ = -21.9(14) K but does not order down to 3 K. The resistivity displays a negative temperature dependence but does not follow the activated behavior ($\rho = \rho_o e^{-E_G/2kT}$) typical of semiconductors.[4.14]

Another structure type which is related to $YbFe_2Al_{10}$ is the $Ce_2Ru_3Al_{15}$ structure type.[4.15] Like $CeRu_4(Al,Si)_{15.58}$, $Ce_2Ru_3Al_{15}$ contains Ce polyhedra which are similar to those in $CeRu_2Al_{10}$. Furthermore, these polyhedra form face sharing columns much like the columns in $CeRu_2Al_{10}$. It is therefore of interest to study the properties of $Ce_2Ru_3Al_{15}$ in order to gain a better understanding of both how the Ce environment *and* the packing of the Ce polyhedra influence the properties. Herein, we report on the synthesis, structure, and properties of $Ln_2Ru_3Al_{15}$ (*Ln* = Ce, Gd) and compare them to the properties of $LnRu_2Al_{10}$.

## 4.2 Experimental Section

### 4.2.1 Synthesis

Ce (Pieces- 99.9% metal basis excluding Ta), Gd (Pieces- 99.9% metal basis excluding Ta), Al (Shot- 99.999%), and Ru (Powder- 99.9%) were used as received. For flux growth reactions, the elements were loaded into an alumina crucible, covered with a second crucible, and

sealed in an evacuated fused-silica tube. Individual reaction ratios and temperature profiles for the growths will be discussed in the results section. After the heating cycles were complete, the reactions were inverted and centrifuged to remove any excess flux. For radio frequency induction furnace growths, the reactant metals were loaded into an alumina crucible which was wrapped in tantalum foil. The crucible was placed in the furnace chamber which was evacuated and flushed with Ar three times then pressurized with Ar during heating. The temperature was increased (~100 °C per minute) until the sample was completely melted. The sample was further heated and dwelled for ~ 10 minutes before being quick cooled (~100 °C per minute) to room temperature. Unfortunately, the utilized induction furnace is not equipped with a temperature probe. However, based on previous experience with the furnace and experimental results (vide infra) it is believed that the reaction temperature was above the 1200 °C maximum achieved by the conventional flux method. For growths via arc melting, the reactant metals were placed on a copper hearth in the arc furnace chamber. The chamber was evacuated and flushed with Ar three times then pressurized with Ar. The reactant metals were melted into a button which was turned over and remelted three times to ensure homogeneity. In order to minimize mass loss, the ruthenium powder was initially arc melted into buttons before being used for the synthesis of $Ln_2Ru_3Al_{15}$. Mass loss in these reactions ranged from 0.53 - 1.16%. Arc melted samples were placed in alumina crucibles and sealed in quartz tubes filled with a partial pressure of argon prior to annealing. A partial pressure was used such that the internal pressure and external pressure were similar in order to help maintain tube integrity during long, high temperature dwells.

### 4.2.2 Structure

Structure determination was performed using single crystal X-ray diffraction data. For $Ce_2Ru_3Al_{15}$, a single crystal was obtained from an aluminum poor flux growth reaction, and for

$Gd_2Ru_3Al_{15}$ a single crystal was extracted from an arc melted pellet. Data collections were performed using an Enraf Nonius KappaCCD diffractometer with a Mo $K_\alpha$ source ($\lambda$ = 0.71073 Å). Direct methods using SIR97[4.16] were performed in order to obtain an initial structural model which was then refined using SHELXL-97.[4.17] Crystallographic data and atomic positions for $Ln_2Ru_3Al_{15}$ can be found in Tables 4.1 and 4.2, respectively. In order to determine reaction products and to ensure that the annealed arc melted buttons were phase pure, powder X-ray diffraction was performed using a Bruker AXS D8 Advance Diffractometer with a Cu Kα source ($\lambda$ = 1.54056 Å) equipped with a Ge incident beam monochromator.

**Table 4.1** Crystallographic Data for $Ln_2Ru_3Al_{15}$ (*Ln* = Ce, Gd)

| Formula | **$Ce_2Ru_3Al_{15.04}$** | **$Gd_2Ru_{3.08}Al_{15}$** |
|---|---|---|
| Space group | $P6_3/mcm$ | $P6_3/mcm$ |
| *a* (Å) | 13.1210(10) | 13.0320(10) |
| *c* (Å) | 9.0970(10) | 9.0590(10) |
| *V* (Å$^3$) | 1356.3(2) | 1332.4(2) |
| *Z* | 4 | 4 |
| Crystal dimensions (mm$^3$) | 0.13 x 0.15 x 0.15 | 0.03 x 0.03 x 0.13 |
| Temperature (K) | 295(1) | 295(1) |
| Density (g cm$^{-3}$) | 4.845 | 5.137 |
| $\theta$ Range (°) | 1.79-30.99 | 1.80-30.98 |
| $\mu$ (mm$^{-1}$) | 10.784 | 14.184 |
| | | |
| *Data Collection and Refinement* | | |
| Collected reflections | 5182 | 4760 |
| Unique reflections | 813 | 799 |
| $R_{int}$ | 0.0256 | 0.0309 |
| *h* | $-19 \le h \le 19$ | $-18 \le h \le 18$ |
| *k* | $-15 \le k \le 15$ | $-15 \le k \le 15$ |
| *l* | $-13 \le l \le 12$ | $-12 \le l \le 13$ |
| $\Delta\rho_{max}$ (e Å$^{-3}$) | 1.409 | 1.803 |
| $\Delta\rho_{min}$ (e Å$^{-3}$) | -0.882 | -2.134 |
| GoF | 1.181 | 1.091 |
| Extinction coefficient | 0.00325(9) | 0.00091(8) |
| [a] $R_1(F)$ for $F_o^2 > 2\sigma(F_o^2)$ | 0.0192 | 0.0218 |
| [b] $R_w(F_o^2)$ | 0.0390 | 0.0527 |

[a] $R_1 = \Sigma||F_0| - |F_c||/\Sigma|F_0|$
[b] $wR_2 = [\Sigma w(F_o^2 - F_c^2)^2/\Sigma w(F_0^2)^2]^{1/2}$; $P = (F_o^2 + 2F_c^2)/3$; $w = 1/[\sigma^2(F_o^2) + (0.0129P)^2 + 3.6920P]$ and $w = 1/[\sigma^2(F_o^2) + (0.0247P)^2 + 6.3560P]$ for Ce and Gd analogues, respectively

**Table 4.2** Atomic Coordinates and Atomic Displacement Parameters for $Ln_2Ru_3Al_{15}$

| Atom | Wyckoff site | *x* | *y* | *z* | $U_{eq}$ (Å$^2$)[a] | Occ. |
|---|---|---|---|---|---|---|
| $Ce_2Ru_3Al_{15.04}$ | | | | | | |
| Ce(1) | 6*g* | 0.60512(2) | 0 | ¼ | 0.00674(8) | 1 |
| Ce(2) | 2*a* | 0 | 0 | ¼ | 0.00551(15) | 0.825(2) |
| Ce(3) | 4*e* | 0 | 0 | 0.2219(6) | 0.00551(15) | 0.0874(12) |
| Ru(1) | 12*i* | 0.203474(11) | 0.40695(2) | 0 | 0.00532(8) | 1 |
| Al(1) | 12*k* | 0.79755(8) | 0 | 0.02717(13) | 0.0082(2) | 1 |
| Al(2) | 12*i* | 0.40892(5) | 0.81785(10) | 0 | 0.0078(2) | 1 |
| Al(3) | 12*j* | 0.16673(10) | 0.87969(9) | ¼ | 0.0075(2) | 1 |
| Al(4) | 12*j* | 0.72320(10) | 0.47613(9) | ¼ | 0.0087(2) | 1 |
| Al(5) | 12*k* | 0.61777(8) | 0 | 0.89713(13) | 0.0077(2) | 1 |
| Al(6) | 2*b* | 0 | 0 | 0 | 0.004(5) | 0.0874(12) |
| | | | | | | |
| $Gd_2Ru_{3.08}Al_{15}$ | | | | | | |
| Gd(1) | 6*g* | 0.60675(2) | 0 | ¼ | 0.00804(10) | 1 |
| Gd(2) | 2*a* | 0 | 0 | ¼ | 0.00738(17) | 0.670(2) |
| Gd(3) | 4*e* | 0 | 0 | 0.2093(4) | 0.00738(17) | 0.1649(11) |
| Ru(1) | 12*i* | 0.203187(14) | 0.40637(3) | 0 | 0.00588(11) | 1 |
| Ru(2) | 2*b* | 0 | 0 | 0 | 0.0196(13) | 0.1649(11) |
| Al(1) | 12*k* | 0.79815(10) | 0 | 0.02826(17) | 0.0094(3) | 1 |
| Al(2) | 12*i* | 0.40949(6) | 0.81898(12) | 0 | 0.0085(3) | 1 |
| Al(3) | 12*j* | 0.16530(13) | 0.87973(12) | ¼ | 0.0084(3) | 1 |
| Al(4) | 12*j* | 0.72567(13) | 0.47679(12) | ¼ | 0.0097(3) | 1 |
| Al(5) | 12*k* | 0.61650(10) | 0 | 0.89787(17) | 0.0084(3) | 1 |

[a] $U_{eq}$ is defined as one-third of the trace of the orthogonalized $U_{ij}$ tensor.

Energy-dispersive X-ray spectroscopy was performed on a single crystal of $Ce_2Ru_3Al_{15}$ from an aluminum poor flux growth using a FEI Quanta 200 SEM equipped with an EDAX detector. Data were collected for six different locations on a single crystal, and the average and standard deviation were taken as the composition and uncertainty, respectively. The determined composition of the sample, normalized to Ce, was $Ce_{2.0(3)}Ru_{2.59(16)}Al_{13.4(5)}$.

### 4.2.3 Physical Properties

Physical properties were measured on polycrystalline annealed arc melted samples of $Ln_2Ru_3Al_{15}$ which were sanded into bar shapes. Magnetic and electrical transport properties were measured using a Quantum Design Physical Property Measurement System (QD PPMS). Zero field cooled DC magnetic susceptibility was measured as a function of temperature from 3-290 K, and field dependent magnetization was measured up to an applied field of 9 T. Resistivity was measured from 3-290 K, and magnetoresistance was measured from 0-9 T at 3 K using the standard four probe method with an excitation current of 5.13 mA. $H = 0$ heat capacity was measured in a QD PPMS using an adiabatic relaxation technique, for temperatures between 2 and 50 K.

## 4.3 Results and Discussion

### 4.3.1 Synthesis

Initially, the growth of $Ce_2Ru_3Al_{15}$ was attempted using the self-flux method. However, its synthesis proved difficult due to the stability of $CeRu_2Al_{10}$. A graphical depiction of the competition between the two phases is shown in Figure 4.1. When an excess of flux is used, the reaction favors the growth of $CeRu_2Al_{10}$. Dwelling a reaction with a Ce:Ru:Al ratio of 2:3:18 at 1200 °C for 24 h before cooling to 720 °C at 5 °C/h only yielded $CeRu_2Al_{10}$. When stoichiometric amounts of the reactant metals were used, the reaction products were found to be highly dependent on reaction temperature. When the reaction was dwelled at 1050 °C, polycrystalline $CeRu_2Al_{10}$ and $Ru_4Al_{13}$ were grown with none of the desired $Ce_2Ru_3Al_{15}$. Raising the dwell temperature to 1200 °C yielded polycrystalline $Ce_2Ru_3Al_{15}$ as the majority product with large amounts of $CeRu_2Al_{10}$ and $Ru_4Al_{13}$ as impurities. The results of higher temperature syntheses will be discussed in the next paragraph. Single crystalline $Ce_2Ru_3Al_{15}$ can be grown using the self-flux method with flux poor reaction ratios. Reactions with Ce:Ru:Al ratios of either 2:3:12 or 3:4:12,

which were dwelled at 1200 °C, sometimes yielded single crystalline $Ce_2Ru_3Al_{15}$ imbedded in a matrix of binaries. However, the crystals were too small and difficult to extract to be able to be used for the measurement of physical properties.

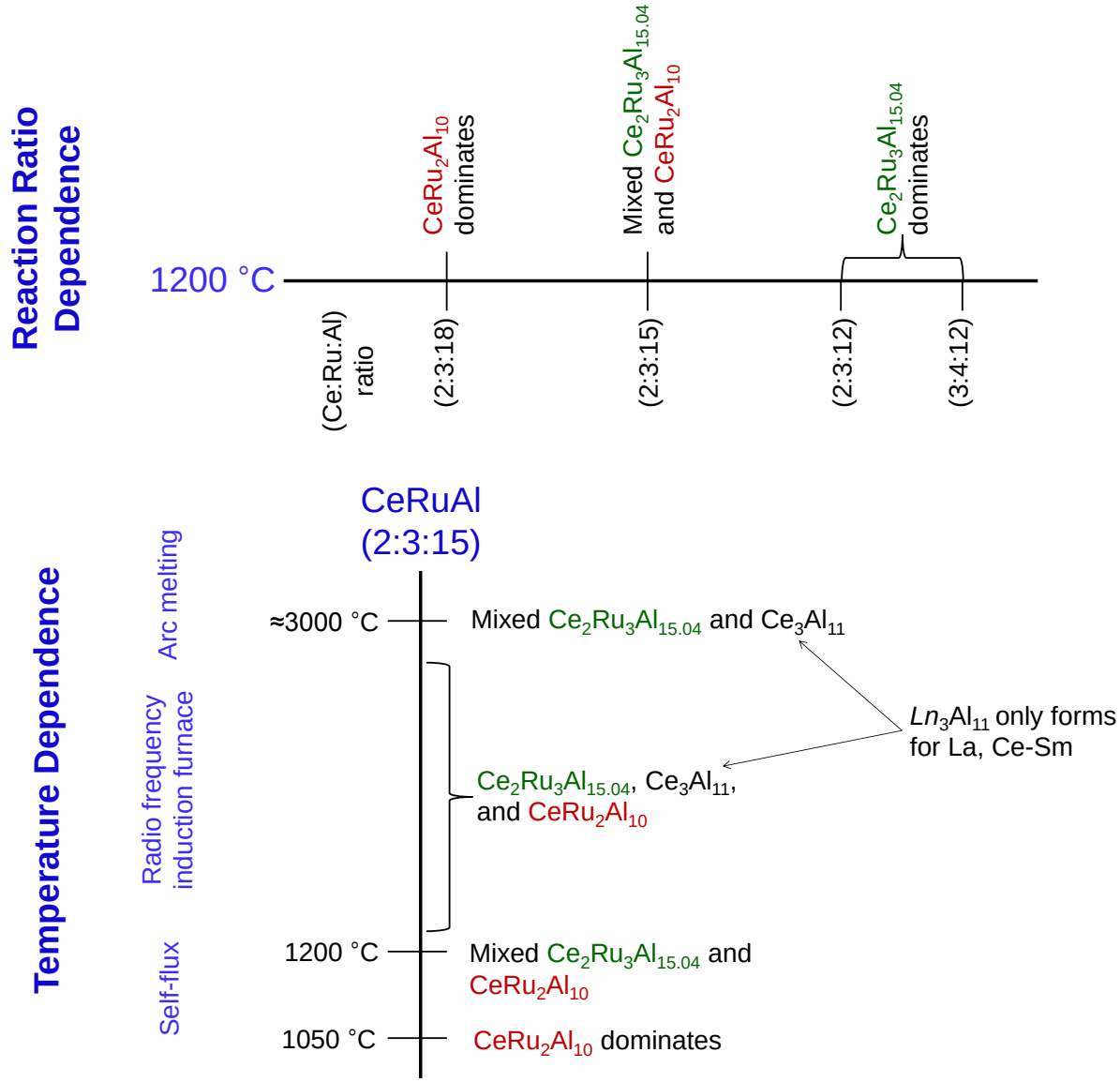


**Figure 4.1** Two schematics showing the products of flux growth reactions dwelled at 1200 °C with various reactant ratios and the products of reactions with a Ce:Ru:Al composition of 2:3:15 heated to various temperatures.

Following the failure to obtain large, extractable single crystals using the flux growth method, the growth of $Ce_2Ru_3Al_{15}$ was attempted using higher temperature synthesis methods, as

the former flux-grown stoichiometric reactions suggested that higher temperatures favored the formation of $Ce_2Ru_3Al_{15}$ over $CeRu_2Al_{10}$ and $Ru_4Al_{13}$. A $Ce_2Ru_3Al_{15}$ growth was attempted by arc melting on stoichiometry, and as expected, no $CeRu_2Al_{10}$ was present in the final button. However, the high temperatures stabilized a different impurity phase, $Ce_3Al_{11}$, which was present in the button along with $Ce_2Ru_3Al_{15}$. In an attempt to eliminate all three impurities, an intermediate temperature growth was performed on stoichiometry using an RF induction furnace. This growth was found to contain $Ce_2Ru_3Al_{15}$, $CeRu_2Al_{10}$ and $Ce_3Al_{11}$, indicating that there is no ideal temperature regime which avoids the growth of all impurities.

Although no optimal temperature was found to grow $Ce_2Ru_3Al_{15}$ on stoichiometry, phase purity of the arc melted pellet can be obtained by annealing. When annealing at low temperatures, circa 800 °C, $CeRu_2Al_{10}$ forms in the sample. In order to avoid this, annealing at 1150 °C is required. By annealing at this temperature for six days, almost-phase-pure $Ce_2Ru_3Al_{15}$ was obtained. In attempt to anneal out the remaining impurity (a small, unidentified impurity resulting in a diffraction peak at $2\theta = 73.8$ °), a sample was annealed at 1150 °C for 12 days. However, this longer annealing time led to the formation of $CeRu_2Al_{10}$. Thus, samples of phase-pure $Gd_2Ru_3Al_{15}$ and almost-phase-pure $La_2Ru_3Al_{15}$ were also prepared via arc melting and annealing for six days.

### 4.3.2 Structure

$Ce_2Ru_3Al_{15}$ crystallizes in the hexagonal space group $P6_3/mcm$ with $a$ = 13.1210(10) Å and $c$ = 9.0970(10) Å. $Gd_2Ru_3Al_{15}$ is reported for the first time and has the lattice parameters $a$ = 13.0320(10) Å and $c$ = 9.0590(10) Å. This structure type has also been reported for $Ln_2Os_3Al_{15}$ ($Ln$ = Nd, Sm, Gd) as an impurity product in arc melted pellets of $LnOs_2Al_{10}$.[4.18] Initially, the structural models of $Ln_2Ru_3Al_{15}$ were refined in agreement with the previously reported structure of $Ce_2Ru_3Al_{15}$.[4.15] In this model there is one Ru site and two lanthanide sites. Each Ru(1) atom

is surrounded by 10 Al atoms forming a distorted pentagonal antiprism which is bicapped by *Ln*(1) atoms such that the point symmetry is 2. The Ru-Al distances, 2.5673(3)-2.6912(6) Å (Ce) and 2.5564(3)-2.6772(8) Å (Gd), are close to the sum of their covalent radii, while the two Ru-*Ln*(1) interactions, 3.4500(3) Å (Ce) and 3.4230(3) Å (Gd), are > 0.5 Å outside of bonding. As shown in Figure 4.2a, each Ru(1) polyhedron is edge-sharing with two other polyhedra, and six of these

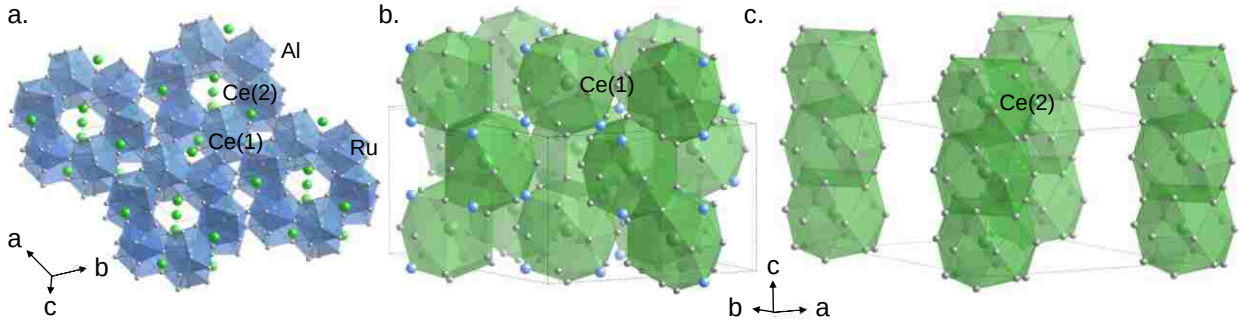


**Figure 4.2** The (a) structure of $Ce_2Ru_3Al_{15}$ showing the Ru polyhedra and the (b) Ce(1) sublattice and (c) Ce(2) sublattice. The Ce(3) and Al(6) sites are omitted for clarity.

polyhedra form a ring. Each polyhedron within the ring is also corner-sharing with two other rings. This generates triangular and quadrilateral channels within the Ru-Al sheets. These sheets lie in the *ab* plane and are edge-sharing in the *c* direction. The Ru sheets resemble the sheets seen in $Ru_{23}(Al,Si)_{97}$ of the α-AlFeSi structure type.[4.14]

The *Ln*(1) polyhedra lie in the square channels created by the Ru sublattice. Each *Ln*(1) atom is surrounded by 14 Al and 4 Ru atoms with point symmetry *mm*. The *Ln*(1) polyhedra resemble the 20 coordinate *Ln* polyhedral seen in $LnRu_2Al_{10}$[4.1] and $CeRu_4(Al,Si)_{15.58}$.[4.14] The *Ln*(1)-Al distances [3.1438(11)-3.3703(7) Å (Ce) and 3.1037(14)-3.3524 Å (Gd)] and *Ln*(1)-Ru distances [3.4500(3) Å (Ce) and 3.4230(3) Å (Gd)], while larger than the sums of the covalent radii, are similar to the distances seen in the respective analogues of the other two structure types. As shown in Figure 4.2b, each *Ln*(1) polyhedron is face sharing with two other *Ln*(1) polyhedra to

form columns in the *c* direction. These columns are edge sharing with each other through the Ru(1) atoms.

Figure 4.3a compares the Ce(1) environment in $Ce_2Ru_3Al_{15}$ to the Ce environments in $CeRu_2Al_{10}$ and $CeRu_4(Al,Si)_{15.58}$. As stated above, the 18 coordinate Ce(1) polyhedra in $Ce_2Ru_3Al_{15}$ are closely related to the 20 coordinate Ce polyhedra in the other two compounds. The main difference between these three polyhedra concerns two equivalent atoms. In $CeRu_4(Al,Si)_{15.58}$ these two atoms are Ru2 atoms, and the Ce-Ru2 distances are comparable to the

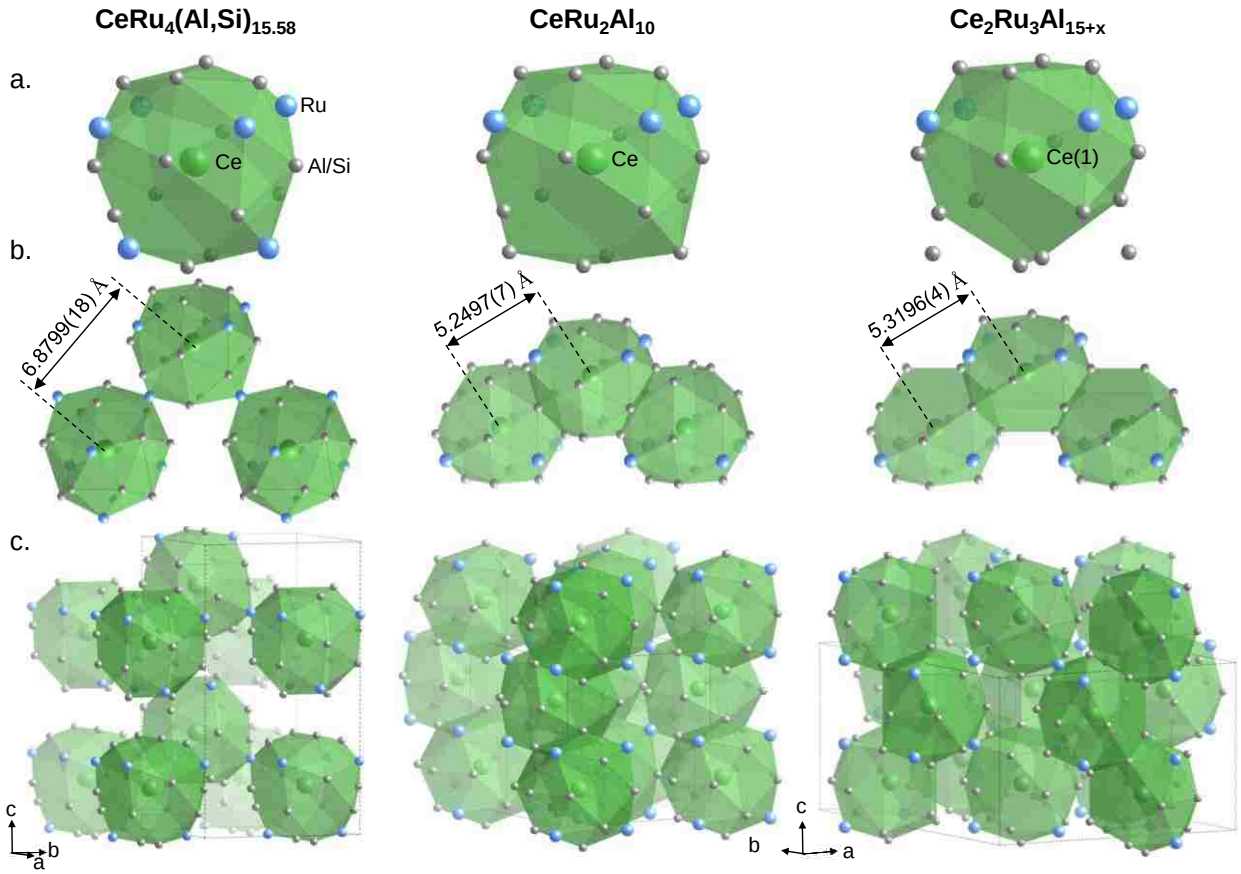


**Figure 4.3** A comparison of the Ce(1) environments in $CeRu_4(Al,Si)_{15.58}$, $CeRu_2Al_{10}$ and $Ce_2Ru_3Al_{15}$ showing the (a) Ce(1) polyhedra, (b) Ce(1)-Ce(1) nearest neighbors and (c) packing of the Ce(1) polyhedra within the unit cells.

other Ce-Ru distances in the polyhedra. In $CeRu_2Al_{10}$, these atoms are Al(1) atoms and the Ce-Al(1) distances are approximately 0.36 Å larger than the other Ce-Al distances. In $Ce_2Ru_3Al_{15}$, these atoms are Al(8) atoms but the Ce(1)-Al(8) distances are over 0.5 Å larger than the largest Ce(1)-Al distance, and therefore the Al(8) atoms are no longer considered part of the Ce(1) polyhedron. Figure 4.3b shows the packing of the Ce(1) polyhedra in each compound. The Ce polyhedra in $Ce_2Ru_3Al_{15}$ and $CeRu_2Al_{10}$ pack in the same way. That is, they form face sharing columns in the *c* direction. While packing in the same way, the Ce(1)-Ce(1) distances in $CeRu_2Al_{10}$, 5.2497(7) Å, are somewhat closer than in $Ce_2Ru_3Al_{15}$, 5.3196(4) Å. The Ce polyhedral in $CeRu_4(Al,Si)_{15.58}$, on the other hand, form corner sharing columns in the *b* direction through the Ru(2) atoms. Due to the fact that they are corner sharing, the Ce(1)-Ce(1) distances in $CeRu_4(Al,Si)_{15.58}$ of 6.8799(18) Å are considerably larger than in the other two compounds.[4.14] It is important to note that while Ce(1) is the only Ce site in $CeRu_2Al_{10}$ and $CeRu_4(Al,Si)_{15.58}$, this is not the case in $Ce_2Ru_3Al_{15}$. A comparison of all of the *Ln-Ln* contact distances in each structure can be found in Table 4.3 and pack in different ways, as can be seen in Figure 4.3c. In both

**Table 4.3** Comparison of *Ln-Ln* distances between titled structure types

| Interaction | Ce (Å) | Gd (Å) | Ref. |
|---|---|---|---|
| ***Ln*Ru$_4$(Al,Si)$_{15.58}$** | | | |
| *Ln*(1)-*Ln*(1) | 6.8799(18) | — | 4.14 |
| ***Ln*Ru$_2$Al$_{10}$** | | | |
| *Ln*(1)-*Ln*(1) | 5.2497(7) | 5.2516(7) | 4.12 |
| ***Ln*$_2$Ru$_3$Al$_{15}$** | | | |
| *Ln*(1)-*Ln*(1) | 5.3196(4) | 5.3158(5) | |
| *Ln*(1)-*Ln*(2) | 5.1812(3) | 5.1248(4) | |
| *Ln*(1)-*Ln*(3) | 5.1875(4) | 5.1381(5) | |
| *Ln*(2)-*Ln*(2) | 4.5485(5) | 4.5295(5) | |
| *Ln*(2)-*Ln*(3) | 4.293(6) | 4.161(4) | |
| *Ln*(3)-*Ln*(3) | 5.060(8) | 5.267(5) | |

compounds the columns are corner sharing through the Ru atoms, but in $CeRu_2Al_{10}$ the columns are aligned with each other while in $Ce_2Ru_3Al_{15}$ each column is rotated 120 ° with respect to the adjacent columns.

The *Ln*2 polyhedra lie in the center of the six-membered Ru polyhedral rings. Each *Ln*(2) is surrounded by 18 Al atoms with point symmetry -6*m*2. The *Ln*(2)-Al distances range from 3.2759(11) to 3.6625(9) Å (Ce) and 3.2363(14) to 3.6433(12) Å (Gd). The *Ln*(2) polyhedra form volume sharing columns in the *c* direction, as shown in Figure 4.2c. Each *Ln*(2) polyhedron is also face sharing with three *Ln*(1) polyhedra in the *ab* plane.

Following the initial refinement of the models using the previously reported structure of $Ce_2Ru_3Al_{15}$, the largest residual electron density was 3.931 and 18.869 $e^-/Å^3$ for the Ce and Gd analogues, respectively. These Q peaks were located at the origin with the closest contacts being two *Ln*(2) atoms 2.27 (Ce) or 2.26 (Gd) Å away. Because of the close proximity of the *Ln*(2) contacts, it was believed that the site was either a partially occupied Al or Ru atom. Due to the partial occupancy of the site, either atom resulted in the same quality structural model. For the Ce analogue the resulting site occupancies were 8.5(13)% (Al) and 2.4(4)% (Ru), and for the Gd analogue the occupancies were 46.5(16)% (Al) and 13.5(4)% (Ru). While the identity of the atom can not be determined by looking at the site, it can be determined from the splitting of the *Ln*(2) site. Since the *Ln*(2) contacts are inside the sum of the covalent radii, when the partially occupied atom is present, the adjacent *Ln*(2) atoms are pushed off the mirror plane to a *Ln*(3) site. Because of the closeness of the *Ln*(2) and *Ln*(3) sites, the atomic displacement parameters of these sites had to be refined isotropically. The occupancy of the *Ln*(3) site was found to be 9.0(14)% for the Ce analogue and 17.8(4)% for the Gd analogue. Comparing these occupancies to the Al or Ru occupancies reveals that the partially-occupied site is an Al site [Al(6)] for the Ce analogue and a

Ru site [Ru(2)] for the Gd analogue. Since the occupancy of *Ln*(3) should equal that of Al(6) or Ru(2), the occupancies of the sites were then confined. This resulted in an Al(6) occupancy of 8.72(12)% and a Ru(2) occupancy of 16.49(11)%. Based on these occupancies, the resulting stoichiometries are $Ce_2Ru_3Al_{15.04}$ and $Gd_2Ru_{3.08}Al_{15}$. For simplicity, the two analogues will continue to be referred to using the $Ln_2Ru_3Al_{15}$ stoichiometry.

The *Ln*(3) site is surrounded by 15 Al atoms and either an Al(6) or Ru(2) atom with point symmetry 3. The *Ln*(3)-Al distances range from 3.193(3) to 3.502(4) Å (Ce) and 3.100(2) to 3.546(3) Å (Gd). The Ce(3)-Al(6) contact is 2.530(5) Å and the Gd(3)-Ru(2) contact is 2.663(3) Å, both of which are closer than the sum of their covalent radii, 2.90 and 2.85 Å, respectively.[4.19] The closer Ce-Al contact, despite the larger sum of covalent radii, suggests that Ce(3) is tetravalent. The different atom types in the two structures does not appear to be a structural effect, as Ru and Al have very close covalent radii and have similar interatomic distances within *Ln*-Ru-Al compounds.[4.12, 20, 21] On the other hand, the structural difference may be an electronic effect. Tetravalent Ce donates more electrons to the conduction band than $Gd^{3+}$. This difference is counteracted by the fact that Ru has a greater number of valence electrons than does Al.

Excluding the disordered *Ln*(3), the closest *Ln*-*Ln* contacts within $Ln_2Ru_3Al_{15}$ are between volume sharing *Ln*(2) polyhedra and are 4.5485(5) Å (Ce) and 4.5295(5) (Gd) Å. The *Ln*(1)-*Ln*(1) contacts are 5.3196(4) (Ce) and 5.3158(5) (Gd) Å which is farther than the contacts found in $LnRu_2Al_{10}$ (5.2497(7) (Ce) and 5.2516(7) (Gd) Å). The *Ln*(1)-*Ln*(2) contacts, which are closer than the *Ln*(1)-*Ln*(1) contacts and the $LnRu_2Al_{10}$ contacts, are 5.1812(3) (Ce) and 5.1248(4) (Gd) Å. These distances along with the *Ln*-*Ln*(3) distances can be found in Table 4.4.

**Table 4.4** Select Interatomic Distances in $Ln_2Ru_3Al_{15}$ (*Ln* = Ce, Gd) (Å)

| Interaction | $Ce_2Ru_3Al_{15.04}$ | $Gd_2Ru_{3.08}Al_{15}$ |
|---|---|---|
| *Ln*(1)-Ru(1) (x4) | 3.4500(3) | 3.4230(3) |
| *Ln*(1)-Al(1) (x2) | 3.2380(12) | 3.2026(15) |
| *Ln*(1)-Al(2) (x4) | 3.3703(7) | 3.3524(9) |
| *Ln*(1)-Al(3) (x2) | 3.1438(11) | 3.1037(14) |
| *Ln*(1)-Al(4) (x2) | 3.1477(12) | 3.0976(15) |
| *Ln*(1)-Al(5) (x2) | 3.2144(12) | 3.1925(16) |
| *Ln*(1)-Al(5) (x2) | 3.2162(11) | 3.2029(14) |
| *Ln*(2)-Al(1) (x6) | 3.3414(11) | 3.3098(14) |
| *Ln*(2)-Al(1) (x6) | 3.6625(9) | 3.6433(12) |
| *Ln*(2)-Al(3) (x6) | 3.2759(11) | 3.2363(14) |
| *Ln*(3)-Al(1) (x3) | 3.193(3) | 3.100(2) |
| *Ln*(3)-Al(1) (x3) | 3.491(4) | 3.399(2) |
| *Ln*(3)-Al(1) (x3) | 3.502(4) | 3.546(3) |
| *Ln*(3)-Al(3) (x6) | 3.2859(12) | 2.2572(14) |
| *Ln*(3)-M[a] (x1) | 2.530(5) | 2.663(3) |
| Ru(1)-*Ln*(1) (x2) | 3.4500(3) | 3.4230(3) |
| Ru(1)-Al(1) (x2) | 2.6879(6) | 2.6690(8) |
| Ru(1)-Al(2) (x2) | 2.5673(3) | 2.5564(3) |
| Ru(1)-Al(3) (x2) | 2.6686(6) | 2.6597(7) |
| Ru(1)-Al(4) (x2) | 2.6686(6) | 2.6259(7) |
| Ru(1)-Al(5)(x2) | 2.6912(6) | 2.6772(8) |
| M[a]-*Ln*(3) (x2) | 2.530(5) | 2.633(3) |
| M[a]-Al(1) (x6) | 2.6678(11) | 2.6439(13) |

[a]M = Al6 for Ce analogue and Ru2 for Gd analogue

## 4.4 Physical Properties

### 4.4.1 Magnetization

Table 4.5 summarizes the magnetic data for $LnRu_2Al_{10}$ and $Ln_2Ru_3Al_{15}$ (*Ln* = Ce, Gd). Figure 4.4a shows the magnetic susceptibility of $Ce_2Ru_3Al_{15}$ as a function of temperature at an applied field of 0.1 T. The inset shows the derivative of the susceptibility and highlights two

**Table 4.5** Magnetic Properties for $LnRu_2Al_{10}$ and $Ln_2Ru_3Al_{15}$ (*Ln* = Ce, Gd)

| | $\chi_o$(emu/mol-Ln) | $T_N$ (K) | θ (K) | $\mu_{calc}$ ($\mu_B$) | $\mu_{eff}$ ($\mu_B$) | Fit Range (K) | Ref. |
|---|---|---|---|---|---|---|---|
| $CeRu_2Al_{10}$ | | 27.3 | -44 | 2.54 | 3.03 | | 4.6 |
| $GdRu_2Al_{10}$ | 0.00015(4) | 15.5 | -15.45(8) | 7.94 | 8.14(10) | 50-275 | 4.12 |
| $Ce_2Ru_3Al_{15}$ | 0.00018(7) | 3.7 | -7(3) | 2.54 | 2.33(4) | 100-290 | |
| $Gd_2Ru_3Al_{15}$ | 0.0008(3) | 21.0 | 11.5(17) | 7.94 | 7.97(7) | 160-288 | |

apparent low temperature transitions. Heat capacity data (vide infra) shows that these transitions are bulk transitions and occur at 3.7 K and 3.1 K. Below 100 K, the inverse susceptibility drops below Curie-Weiss behavior, which can be attributed to crystalline electric field effects. Similar behavior has been observed in other rare earth intermetallics such as hexagonal CeNiIn[4.22] and orthorhombic $CePtSi_2$[4.23] and is expected as $CeRu_2Al_{10}$ was found to display considerable CEF effects.[4.8] Fitting from 100-290 K with a modified Curie-Weiss law $\chi = \chi_o + C/(T - \theta)$, where $\chi_0$ is a temperature independent sum of the diamagnetic and Pauli paramagnetic contributions, yields a Curie-Weiss temperature of -7(3) K. The negative θ, coupled with the increase in dχ/dT below

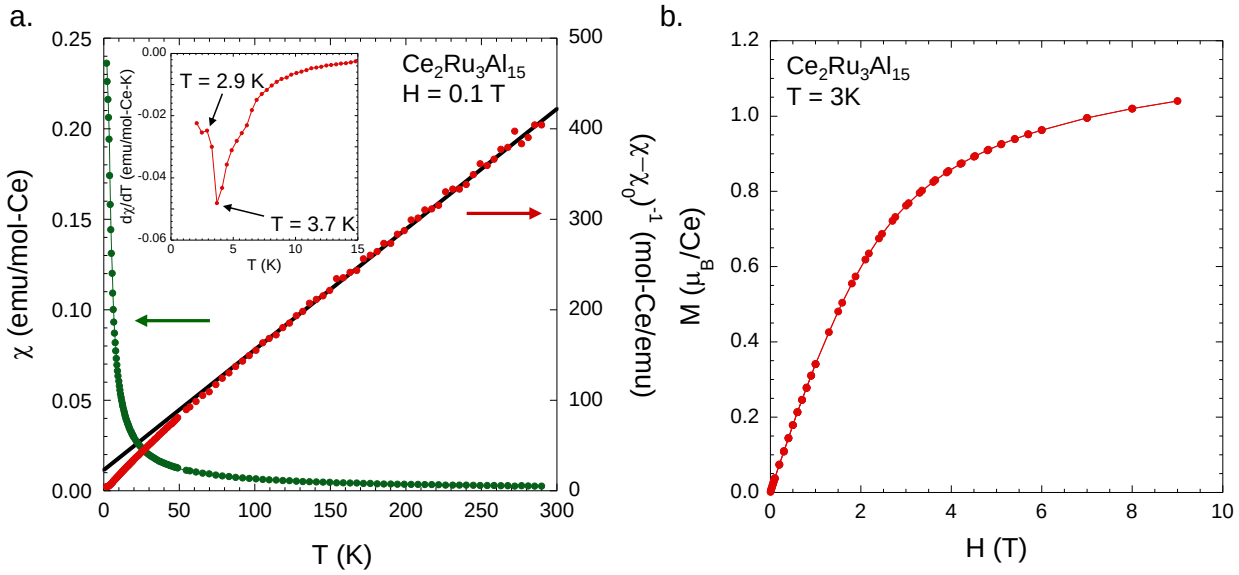


**Figure 4.4** (a) Magnetic susceptibility and inverse susceptibility of $Ce_2Ru_3Al_{15}$. Inset shows the derivative of the susceptibility, highlighting two low temperature transitions. (b) Field-dependent magnetization of $Ce_2Ru_3Al_{15}$.

3.7 K and the AFM ordering of $Gd_2Ru_3Al_{15}$, as shown below, suggests that the 3.7 K transition is an AFM ordering. An effective moment of 2.33(4) $\mu_B$ is determined from the Curie-Weiss fit at high temperatures and is less than the 2.54 $\mu_B$ expected for $Ce^{3+}$. The magnetization as a function of field, shown if Figure 4.4b, appears to saturate at ~1.04 $\mu_B$/Ce which is smaller than the 2.14 $\mu_B$ expected for trivalent Ce.

The temperature dependent magnetic susceptibility of $Gd_2Ru_3Al_{15}$ at 0.1 T, shown in Figure 4.5a, displays an AFM ordering at $T_N$ = 21.0 K with a spin reorientation at 4.1 K, similar to the two spin reorientations observed in $Ce_2Ru_3Al_{15}$. Below 150 K, the inverse susceptibility deviates below Curie-Weiss behavior. This deviation is believed to be caused by a small FM impurity, below the detection limit of powder XRD, such as $GdAl_2$, which orders at ~170 K, depending on sample purity and disorder.[4.24] Fitting with a modified Curie-Weiss law above 160 K yields an effective moment of 7.97(7) $\mu_B$, close to the 7.94 $\mu_B$ expected for $Gd^{3+}$, and a $\theta$ of 11.5(17) K. This suggests that the Ru atoms are non-magnetic. As the *f* orbital of Gd is half-filled,

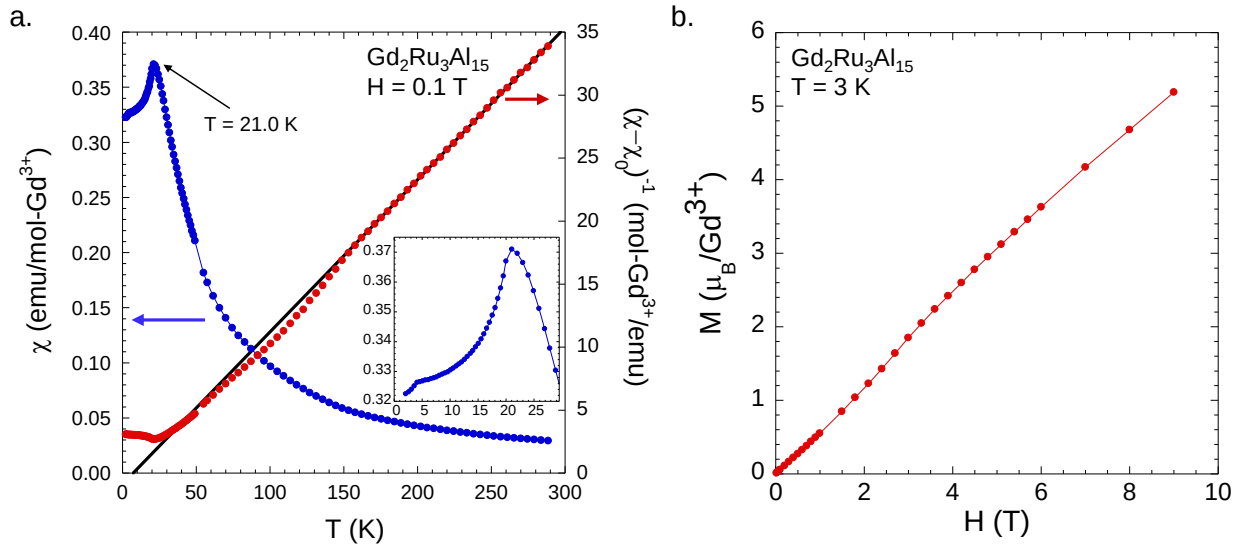


**Figure 4.5** (a) Magnetic susceptibility and inverse susceptibility of $Gd_2Ru_3Al_{15}$. Inset highlights the two low temperature transitions. (b) Field-dependent magnetization of $Gd_2Ru_3Al_{15}$.

and therefore spherically symmetric, the positive Curie-Weiss temperature cannot be due to CEF effects. Therefore, a positive $\theta$, despite the antiferromagnetic ordering, suggests strong ferromagnetic correlations within the structure. One possibility is that these correlations involve the Gd(3) atoms. As the Gd(2)-Gd(3) distance, 4.161(4) Å, is the closest distance in the structure, based on $1/r^3$ attenuation of the RKKY interaction,[4.25-27] a mechanism in which the conduction electrons mediate magnetic ordering, it may have the strongest $J$ coupling. However, due to the partial occupancy of the Gd(3) site, no long range order can exist. This would also explain the lack of a positive Curie-Weiss temperature in $Ce_2Ru_3Al_{15}$, as Ce(3) is believed to be tetravalent. Magnetization as a function of field is shown in Figure 4.5b and does not saturate up to 9 T. A broad transition, possible a partial spin reorientation, is observed at $H \sim 2.5$ T.

### 4.4.2 Electrical Transport

Figures 4.6a and 4.6b show the polycrystalline resistivity (a) and magnetoresistance (b) of $Ce_2Ru_3Al_{15}$ (green) and $Gd_2Ru_3Al_{15}$ (blue), respectively. Both analogues display a similar

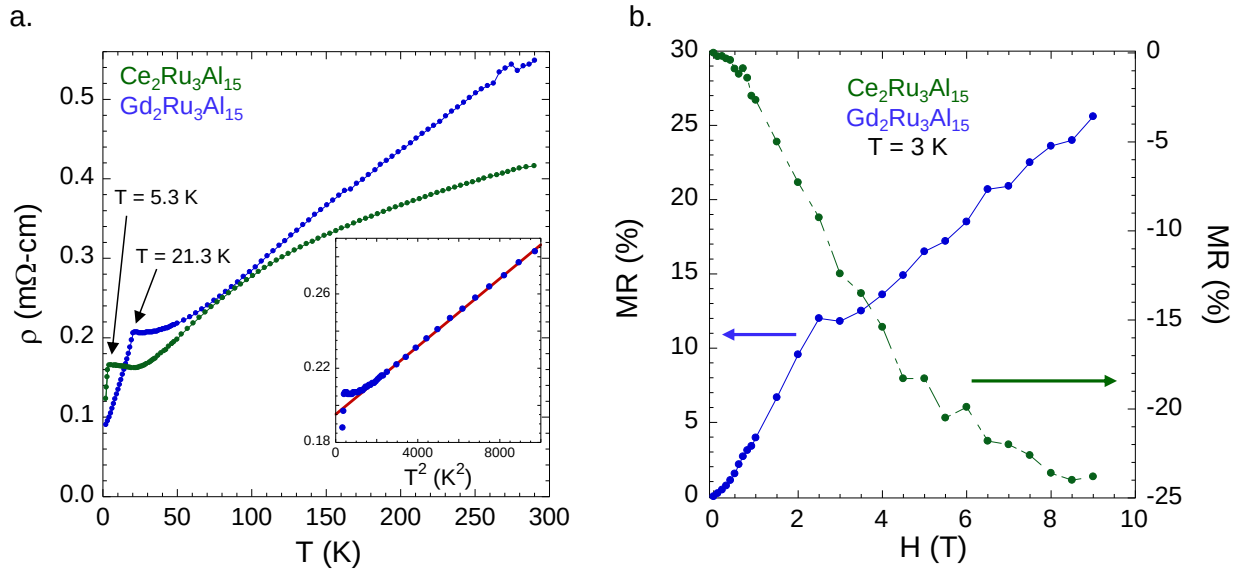


**Figure 4.6** (a) Resistivity and (b) magnetoresistance of $Ln_2Ru_3Al_{15}$ ($Ln$ = Ce, Gd). Inset in (a) highlights the low temperature dependence of the resistivity for the Gd analogue.

magnitude of resistivity, with $\rho_{290K} \approx 0.42$ mΩ-cm (Ce) and 0.55 mΩ-cm (Gd) and $\rho_{2K}$ of 0.12 mΩ-cm and 0.091 mΩ-cm (Gd). This leads to residual resistivity ratios, RRR = ($\rho_{290K/}$ $\rho_{2K}$), of 3.4 (Ce) and 6.1 (Gd). These RRR values are smaller than the 8.9 observed for a single crystal of $GdRu_2Al_{10}$ and can be attributed to grain boundary scattering due to the polycrystalline nature of the samples. For $40 \leq T \leq 100$ K, the resistivity of $Gd_2Ru_3Al_{15}$ follows a $T^2$ dependence, shown in the inset of Figure 4.6a, which is typical of metallic compounds at low temperature.

Decreases in the resistivities at 5.3 K (Ce) and 21.3 K (Gd) can be attributed to a loss of spin disorder scattering due to the magnetic ordering. Prior to this decrease, the Ce analogue displays an upturn at 20 K, suggestive of the Kondo effect, a mechanism in which the conduction electrons screen the magnetic moment of the rare earths.[4.28] This is in agreement with the magnetoresistance (MR), which is negative for $Ce_2Ru_3Al_{15}$ and reaches -24% at 9 T. Before the AFM ordering, the resistivity of $Gd_2Ru_3Al_{15}$ displays a small upturn at 26.3 K. Similar behavior was observed in $GdRu_2Al_{10}$[4.12] and may be due to the formation of magnetic polarons prior to the magnetic ordering, such as is observed in $EuB_6$.[4.29] The MR of $Gd_2Ru_3Al_{15}$ is positive, which is typical for intermetallics, and reaches 26% at 9 T. The magnitude of the MR is greater than in most intermetallic compounds. For example, $GdRu_2Al_{10}$, which orders antiferromagnetically at 15.5 K, with a spin reorientation at 7.8 K, has a MR of less than 1% at 9 T.[4.12] The large MR in $Gd_2Ru_3Al_{15}$ may be due to the proximity of the 3 K measurement temperature to the spin reorientation at 4.1 K. Enhanced MR has been observed in other intermetallics near magnetic transitions.[4.30, 31] At 2.5 T, the MR changes slope, which can be attributed to the broad transition observed in the magnetization as a function of applied field.

### 4.4.3 Heat Capacity

Figure 4.7 shows the specific heat capacity of $Ln_2Ru_3Al_{15}$ ($Ln$ = La, Ce). The low temperature data, emphasized in the inset, displays two transitions in $Ce_2Ru_3Al_{15}$ at 3.7 and 3.1 K. Typically, the low temperature heat capacity of metals follows $C_p = \gamma T + \beta T^3$, where $\gamma$ is the electronic specific heat coefficient and $\beta T^3$ is the phonon contribution to the specific heat. The non-magnetic contribution to the specific heat can be approximated as the specific heat of a non-magnetic analogue, and can be subtracted from $C_p$ to obtain $C_m$, the magnetic specific heat.

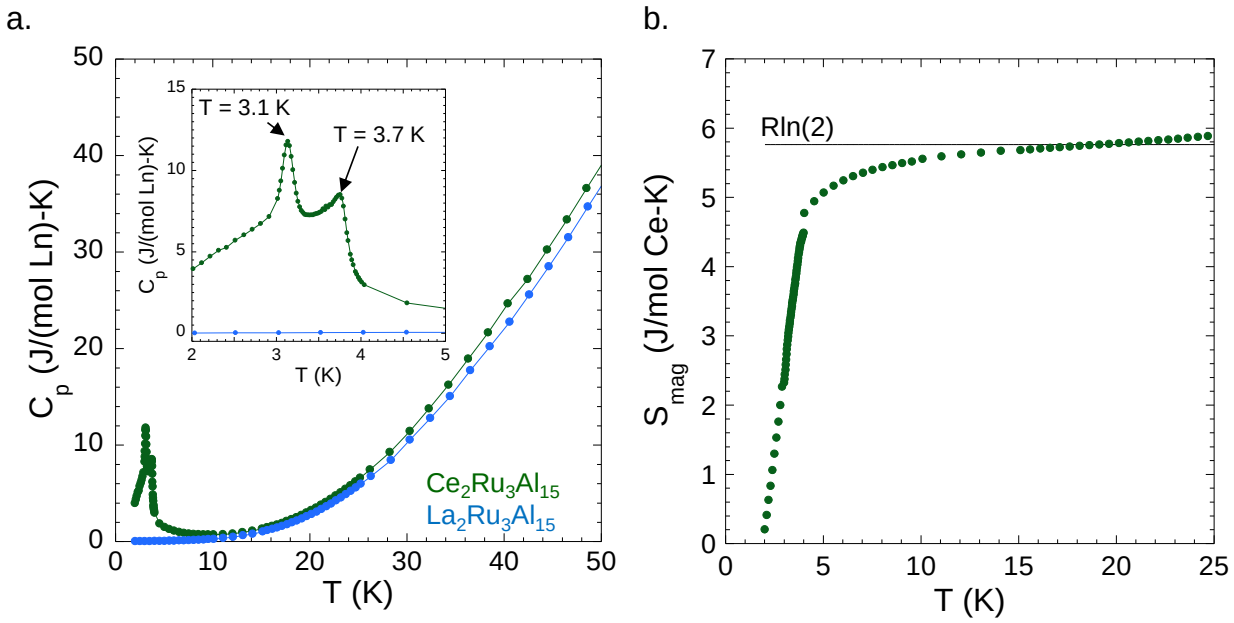


**Figure 4.7** (a) Heat capacity of $Ln_2Ru_3Al_{15}$ ($Ln$ = La, Ce). Inset highlights the low temperature transitions in the Ce analogue. (b) Magnetic entropy of $Ce_2Ru_3Al_{15}$ as a function of temperature. The solid line indicates Rln2.

The specific heat of the La analogue was subtracted from the Ce analogue in order to obtain $C_m$. For a magnetic transition, $R\ln(2J+1)$ of entropy ($S_m$) should accompany the transition, where $J$ is the total angular momentum. Integrating the magnetic entropy of $Ce_2Ru_3Al_{15}$ from 2 K to 15 K recovers $S_m \approx R\ln 2$ entropy, based on the trivalent Ce concentration from the susceptibility. The entropy is actually recovered prior to 15 K as the phase transition is still occurring below 2 K and

therefore, not all of the magnetic entropy has been integrated. Due to the non-linearity of $C_m/T$ vs. $T^2$ above the magnetic orderings, believed to be caused by small impurities in the arc melted samples, the Sommerfeld coefficient was not determined.

### 4.4.4 Comparison of Structure Types

$GdRu_2Al_{10}$ orders antiferromagnetically at 15.5 K, while $Gd_2Ru_3Al_{15}$ orders antiferromagnetically at 21.0 K. Two Gd-Gd interactions are similar in distance to the 5.2516(7) Å distance in $GdRu_2Al_{10}$: the Gd(1)-Gd(1) interaction, 5.3158(5) Å and the Gd(1)-Gd(2) interaction, 5.1248(4) Å. However, it is not readily apparent between which Gd atoms the AFM ordering occurs. $Gd_2Ru_3Al_{15}$, despite being polycrystalline, also has a lower resistivity at the ordering temperature, ~0.2 mΩ-cm, than does $GdRu_2Al_{10}$, ~0.3 mΩ-cm. This suggests that $Gd_2Ru_3Al_{15}$ has a higher carrier concentration, which would lead to stronger RKKY interactions.

Based on the 16 K ordering of $GdRu_2Al_{10}$ and deGennes scaling, $CeRu_2Al_{10}$ is expected to order at 0.1 K.[4.3] Instead, $CeRu_2Al_{10}$ shows an enhanced ordering temperature of 27 K.[4.2] A similar trend is not observed in $Ln_2Ru_3Al_{15}$, where the Gd analogue orders at 21.0 K, and the Ce analogue orders at 3.7 K. Furthermore, $Ce_2Ru_3Al_{15}$ displays metallic resistivity over the entire measured temperature range, 2 - 290 K, unlike $CeRu_2Al_{10}$ which displays a metal-to-insulator transition at 27 K indicative of a narrow gap opening at the Fermi surface.[4.2] While structurally related to $CeRu_2Al_{10}$, it is apparent that $Ce_2Ru_3Al_{15}$ does not display the same anomalous behavior. The contrast in properties despite both structures containing very similar columns of Ce polyhedra suggests that either the properties are dependent on the packing of the columns within the unit cell, or as was suggested in the computation study discussed in the introduction, that the properties of $CeRu_2Al_{10}$ arise due to small changes in the Ce polyhedra. Due to the similar structure but contrasting properties, $Ce_2Ru_3Al_{15}$ offers potential for further comparison studies with $CeRu_2Al_{10}$.

## 4.5 Conclusions

The synthesis of $Ce_2Ru_3Al_{15}$ is difficult due to the stability of $CeRu_2Al_{10}$ at low temperatures and in flux rich melts and the stability of $Ce_3Al_{11}$ at high temperatures. $Ln_2Ru_3Al_{15}$ (*Ln* = La, Ce, Gd) were synthesized by arc melting and annealing at 1150 °C for 6 days. The crystal structure was modified from the originally reported structure[4.15] in order to account for a partially-occupied atom at the origin (2*b*) and the resulting splitting of the *Ln*(2) site into a *Ln*(2) site and a *Ln*(3) site. Based on the occupancy of the *Ln*(3) site, the 2*b* site was determined to be an Al atom in the Ce analogue and a Ru analogue in the Gd analogue.

$Gd_2Ru_3Al_{15}$ was found to order antiferromagnetically at 21.0 K with a spin reorientation at 4.1 K. The Curie-Weiss temperature was found to be positive, indicating FM interactions within the structure, possibly involving the partially-occupied Gd(3) atoms. $Ce_2Ru_3Al_{15}$ displays two spin reorientations, the first of which is believed to be an AFM ordering, at low temperatures, 3.7 K and 3.1 K, made apparent by $d\chi/dT$ and heat capacity measurements. Below 100 K, the susceptibility deviates below the Curie-Weiss fit which is characteristic of lost moment due to Kondo screening. This is supported by an upturn in the resistivity at 20 K and a negative magnetoresistance of -24% at 9 T. $Ce_2Ru_3Al_{15}$ does not display the enhanced ordering temperature or metal-to-insulator transition observed in $CeRu_2Al_{10}$ despite the two structures containing similar columns of Ce polyhedra. For this reason, further comparison studies between the two compounds is warranted and could help elucidate the cause of the anomalous properties observed in $CeRu_2Al_{10}$.

## 4.6 References


4.1. Niemann, S.; Jeitschko, W., *Z. Krist.* **1995,** *210*, 338-341.

4.2. Strydom, A. M., *Physica B* **2009,** *404*, 2981-2984.

4.3. Nishioka, T.; Kawamura, Y.; Takesaka, T.; Kobayashi, R.; Kato, H.; Matsumura, M.; Kodama, K.; Matsubayashi, K.; Uwatoko, Y., *J. Phys. Soc. Jpn.* **2009,** *78*, 123705.

4.4. Mignot, J.-M.; Robert, J.; André, G.; Bataille, A. M.; Nishioka, T.; Kobayashi, R.; Matsumura, M.; Tanida, H.; Tanaka, D.; Sera, M., *J. Phys. Soc. Jpn.* **2011,** *80*, SA022.

4.5. Khalyavin, D. D.; Hillier, A. D.; Adroja, D. T.; Strydom, A. M.; Manuel, P.; Chapon, L. C.; Peratheepan, P.; Knight, K.; Deen, P.; Ritter, C.; Muro, Y.; Takabatake, T., *Phys. Rev. B* **2010,** *82*, 100405.

4.6. Takesaka, T.; Oe, K.; Kobayashi, R.; Kawamura, Y.; Nishioka, T.; Kato, H.; Matsumura, M.; Kodama, K., *J. Phys. Conf. Ser.* **2010,** *200*, 012201.

4.7. Strigari, F.; Willers, T.; Muro, Y.; Yutani, K.; Takabatake, T.; Hu, Z.; Chin, Y. Y.; Agrestini, S.; Lin, H. J.; Chen, C. T.; Tanaka, A.; Haverkort, M. W.; Tjeng, L. H.; Severing, A., *Phys. Rev. B* **2012,** *86*, 081105.

4.8. Hanzawa, K., *J. Phys. Soc. Jpn.* **2011,** *80*, 023707.

4.9. Kimura, S.-i.; Iizuka, T.; Miyazaki, H.; Irizawa, A.; Muro, Y.; Takabatake, T., *Phys. Rev. Lett.* **2011,** *106*, 056404.

4.10. Tanida, H.; Tanaka, D.; Sera, M.; Moriyoshi, C.; Kuroiwa, Y.; Takesaka, T.; Nishioka, T.; Kato, H.; Matsumura, M., *J. Phys. Soc. Jpn.* **2010,** *79*, 043708.

4.11. Goraus, J.; Ślebarski, A., *J. Phys. Condens. Matter* **2012,** *24*, 095503.

4.12. Morrison, G.; Haldolaarachchige, N.; Young, D. P.; Chan, J. Y., *J. Phys. Condens. Matter* **2012,** *24*, 356002.

4.13. Fehrmann, B.; Jeitschko, W., *J. Alloys Compd.* **2000,** *298*, 153-159.

4.14. Morrison, G. W.; Menard, M. C.; Treadwell, L. J.; Haldolaarachchige, N.; Kendrick, K. C.; Young, D. P.; Chan, J. Y., *Philos. Mag.* **2012,** *92*, 2524-2540.

4.15. Tursina, A. I.; Murashova, E. V.; Nesterenko, S. N.; Chernyshev, I. V.; No; l, H.; Seropegin, Y. D., *Acta Crystallogr. Sect. E* **2004,** *60*, i145-i146.

4.16. Altomare, A.; Burla, M. C.; Camalli, M.; Cascarano, G.; Giacovazzo, C.; Guagliardi, A.; Moliterni, A. G. G.; Polidori, G.; Spagna, R., *J. Appl. Crystallogr.* **1999,** *32*, 115.

4.17. Sheldrick, G. M., *Acta Crystallogr. Sect. A* **2008,** *64*, 112-122.

4.18. Muro, Y.; Kajino, J.; Onimaru, T.; Takabatake, T., *J. Phys. Soc. Jpn.* **2011,** *80*, SA021.

4.19. Emsley, J., *The Elements*. 2 ed.; Oxford University Press: New York, 1991.

4.20. Niemann, J.; Jeitschko, W., *Z. anorg. allg. Chem.* **2002,** *628*, 2549-2556.

4.21. Murashova, E. V.; Tursina, A. I.; Bukhanko, N. G.; Nesterenko, S. N.; Kurenbaeva, Z. M.; Seropegin, Y. D.; Noël, H.; Potel, M.; Roisnel, T.; Kaczorowski, D., *Mater. Res. Bull.* **2010,** *45*, 993-999.

4.22. Fujii, H.; Inoue, T.; Andoh, Y.; Takabatake, T.; Satoh, K.; Maeno, Y.; Fujita, T.; Sakurai, J.; Yamaguchi, Y., *Phys. Rev. B* **1989,** *39*, 6840-6843.

4.23. Lee, W. H.; Kwan, K. S.; Klavins, P.; Shelton, R. N., *Phys. Rev. B* **1990,** *42*, 6542-6545.

4.24. Williams, D. S.; Shand, P. M.; Pekarek, T. M.; Skomski, R.; Petkov, V.; Leslie-Pelecky, D. L., *Phys. Rev. B* **2003,** *68*, 214404.

4.25. Ruderman, M. A.; Kittel, C., *Phys. Rev.* **1954,** *96*, 99-102.

4.26. Kasuya, T., *Prog. Theor. Phys.* **1956,** *16*, 45-57.

4.27. Yosida, K., *Phys. Rev.* **1957,** *106*, 893-898.

4.28. Edelstein, A. S., *J. Magn. Magn. Mater.* **2003,** *256*, 430-448.

4.29. Snow, C. S.; Cooper, S. L.; Young, D. P.; Fisk, Z.; Comment, A.; Ansermet, J.-P., *Phys. Rev. B* **2001,** *64*, 174412.

4.30. Chan, J. Y.; Kauzlarich, S. M.; Klavins, P.; Liu, J. Z.; Shelton, R. N.; Webb, D. J., *Phys. Rev. B* **2000,** *61*, 459-463.

4.31. Mazumdar, C.; Nigam, A. K.; Nagarajan, R.; Gupta, L. C.; Chandra, G.; Padalia, B. D.; Godart, C.; Vijayaraghaven, R., *J. Appl. Phys.* **1997,** *81*, 5781-5783.

# Chapter 5. Synthesis and Anisotropic Properties of Single Crystalline $Gd_2Ru_3Al_{15.09}$

## 5.1 Introduction

Single crystalline samples offer many advantages over polycrystalline samples including structure determination via single crystal X-ray diffraction and the measurement of intrinsic properties unaltered by impurities or grain boundaries, including anisotropic properties.[5.1, 2] Anisotropic properties can be instrumental in understanding the intrinsic properties of a system. For example, studies of the anisotropic magnetization of $EuZn_2Sb_2$ found that the antiferromagnetic ordering consisted of spins lying perpendicular to the *c*-axis.[5.3] Similarly, anisotropic magnetic properties of $CeNiSb_2$ indicated that the ferromagnetic easy axis is the *a*-axis.[5.4] In some cases, the bulk polycrystalline properties can differ from the properties of a single crystal.[5.5, 6] For example, the Neel temperatures of single crystals of $Ln(Cu,Al)_{12}$ follow de Gennes scaling[5.7] while the Neel temperatures of polycrystalline samples deviate significantly.[5.8]

While single crystalline samples offer many advantages, their growth can be difficult, especially when another compound is more robust and stable. We previously reported on the synthesis, structure, and magnetic and transport properties of $Ln_2Ru_3Al_{15}$ (*Ln* = Ce, Gd).[5.9] The synthesis of $Ln_2Ru_3Al_{15}$ was complicated by the stability of $LnRu_2Al_{10}$ relative to $Ln_2Ru_3Al_{15}$.[5.9] As a result of the difficulty in growing $Ln_2Ru_3Al_{15}$, magnetic and transport measurements were conducted on polycrystalline arc-melted samples. Polycrystalline $Gd_2Ru_{3.08}Al_{15}$ was found to be metallic and ordered antiferromagnetically at 21.0 K with a spin reorientation at 4.1 K. A deviation from Curie-Weiss behavior at 150 K was believed to be attributed to a ferromagnetic impurity. Fitting the susceptibility above this deviation resulted in a positive Weiss temperature of 11.5(17) K and an effective moment of 7.97(7) $\mu_B$/mol-Gd, which is in good agreement with the expected moment for a free $Gd^{3+}$ ion. Finally, a positive magnetoresistance (MR) of 26% was observed at

3 K and 9 T which was believed to be due to the proximity of the 3 K measurement to the spin reorientation at 4.1 K.[5.9]

We have succeeded in synthesizing large single crystals of $Gd_2Ru_3Al_{15}$ using the flux growth method. Herein, we report on the synthesis, structure and anisotropic properties of single crystals of $Gd_2Ru_3Al_{15.09}$ and compare them to polycrystalline $Gd_2Ru_{3.08}Al_{15}$.

## 5.2 Experimental

### 5.2.1 Synthesis

High purity elements, Gd (pieces, 99.9% REO), Y (pieces, 99.9% REO), Ru (powder, 99.98% metal basis excluding Ca), and Al (99.999% metal basis), were used as obtained. Single crystals were grown using the self-flux technique. The elements were placed in a 99.8% alumina crucible with the Al flux on top. A second crucible was covered on top of the first and the reaction vessel was sealed in an evacuated fused-silica tube backfilled with ~1/6 atm of Ar to help maintain their integrity at high dwell temperatures. Specific elemental ratios and heating profiles will be discussed in the Results and Discussion section. After the growth was complete, the resulting single crystal was mechanically extracted from the flux and polished into a bar shape.

### 5.2.2 Structure

Structure determination was carried out via single crystal X-ray diffraction of a fragment broken off of the same single crystal used for physical property measurements. Diffraction data was collected on an Enraf Nonius KappaCCD diffractometer equipped with a Mo K$\alpha$ source ($\lambda$ = 0.71073 Å). Direct methods using SIR97[5.10] were used to obtain an initial structural model which was then refined using SHELXL-97.[5.11] A summary of the crystallographic data can be found in Table 5.1. Elemental composition was checked by energy dispersive X-ray spectroscopy using an

**Table 5.1** Crystallographic Data for $Gd_2Ru_3Al_{15.09}$

| Formula | **$Gd_2Ru_3Al_{15.09}$** |
|---|---|
| Space group | $P6_3/mcm$ |
| $a$ (Å) | 13.0114(10) |
| $c$ (Å) | 9.0552(10) |
| $V$ (Å$^3$) | 1327.6(2) |
| $Z$ | 4 |
| Crystal dimensions (mm$^3$) | 0.07 x 0.07 x 0.13 |
| Temperature (K) | 295(1) |
| Density (g cm$^{-3}$) | 5.127 |
| $\theta$ Range (°) | 3.13-30.98 |
| $\mu$ (mm$^{-1}$) | 14.153 |
| | |
| *Data Collection and Refinement* | |
| Collected reflections | 5269 |
| Unique reflections | 797 |
| $R_{int}$ | 0.0351 |
| $h$ | $-18 \leq h \leq 18$ |
| $k$ | $-15 \leq k \leq 15$ |
| $l$ | $-13 \leq l \leq 13$ |
| $\Delta\rho_{max}$ (e Å$^{-3}$) | 1.572 |
| $\Delta\rho_{min}$ (e Å$^{-3}$) | -1.749 |
| GoF | 1.128 |
| Extinction coefficient | 0.00482(16) |
| [a] $R_1(F)$ for $F_o^2 > 2\sigma(F_o^2)$ | 0.0229 |
| [b] $R_w(F_o^2)$ | 0.0528 |

[a] $R_1 = \Sigma||F_0| - |F_c||/\Sigma|F_0|$
[b] $wR_2 = [\Sigma w(F_o^2 - F_c^2)^2/\Sigma w(F_0^2)^2]^{1/2}$; $P = (F_o^2 + 2F_c^2)/3$; $w = 1/[\sigma^2(F_o^2) + (0.0233P)^2 + 4.9683P]$

FEI Quanta 200 SEM equipped with an EDAX detector. Six scans across a freshly cut face of the single crystal gave an elemental composition of $Gd_{2.00(12)}Ru_{3.33(18)}Al_{18.0(6)}$.

Orientation of the extracted, bar-shaped, single crystal was carried out using single crystal X-ray diffraction data. Phi scans were collected on three non-confacial corners in order to ensure that the bar was indeed a single crystal with one orientation throughout. The crystallographic *c*-axis was found to coincide with the long axis of the bar-shaped crystal. Because of the hexagonal space group and poor macroscopic alignment of the *a* and *b* crystallographic axes, anisotropic properties will be reported as parallel and perpendicular to the *c*-axis.

After all physical properties measurements were conducted, the bar-shaped single crystal was cut into several faces and the resulting faces were visually inspected to check for any inclusions. Furthermore, a portion of the crystal was ground and used for a powder X-ray diffraction experiment. Powder diffraction was conducted on a Bruker AXS D8 Advance Diffractometer equipped with a Cu K$\alpha$ ($\lambda$ = 1.54056 Å) source and a Ge incident beam monochromator. No indication of an impurity was observed using either technique.

### 5.2.3 Physical Properties

Anisotropic magnetic and transport properties were measured on a bar-shaped crystal parallel and perpendicular to the crystallographic *c*-axis. Magnetic properties were measured on a Quantum Design Magnetic Property Measurement System (MPMS). Magnetic susceptibility was measured from 1.8 - 390 K at $H$ = 0.1 T under zero-field-cooled (ZFC) and field-cooled (FC) conditions and field dependent magnetization was measured for $H$ = 0 - 7 T at 2 K. Electrical resistivity and magnetoresistance were measured on a Quantum Design Physical Property Measurement System (PPMS). Resistivity was measured from 3 - 295 K at an applied current of 5.18 mA and magnetoresistance was measured at 3 K for $H$ = 0 - 9 T using the four probe method.

## 5.3 Results and Discussion

### 5.3.1 Synthesis

The competition between the growth of $Ce_2Ru_3Al_{15}$ and $CeRu_2Al_{10}$ was previously reported.[5.9] In summary, it was found that when dwelled at 1200 °C, Al rich reactions (Ce:Ru:Al - 2:3:18) favored the growth of $CeRu_2Al_{10,}$ a stoichiometric reaction (Ce:Ru:Al - 2:3:15) resulted in a mixture of $Ce_2Ru_3Al_{15}$ and $CeRu_2Al_{10}$, and only in Al poor conditions (Ce:Ru:Al - 2:3:12) was the growth of $Ce_2Ru_3Al_{15}$ dominant. However, due to the flux-poor conditions, only small, irregularly shaped single crystals were formed. Furthermore, it was found that on a stoichiometric

concentration of Ce:Ru:Al (2:3:15), at low dwell temperatures (1050 °C) the growth of $CeRu_2Al_{10}$ dominated, while at intermediate temperatures (1200 - ~2000 °C) both $CeRu_2Al_{10}$ and $Ce_2Ru_3Al_{15}$ grew, and only at temperatures achieved by arc-melting (~ 3000 °C) was the growth of $CeRu_2Al_{10}$ prevented. As a result, the previously reported physical property studies were carried out on polycrystalline arc-melted samples of $Ln_2Ru_3Al_{15}$ (*Ln* = Ce, Gd).[5.9]

The arc-melted Gd analogue was almost phase pure prior to annealing and contained single crystals large enough for single crystal X-ray diffraction. These two indicators, along with the fact that Gd metal is more soluble in Al than is Ce metal, suggested that large single crystals of $Gd_2Ru_3Al_{15}$ may form more readily than $Ce_2Ru_3Al_{15}$. For this reason, the studies done in this manuscript were conducted on $Gd_2Ru_3Al_{15}$. Indeed, the method reported here grows large single crystals of the Gd analogue and other latter rare earth analogues, while the same method using Ce yields predominantly $CeRu_2Al_{10}$ and $Ce_3Al_{11}$.

The formula for $Gd_2Ru_3Al_{15}$ can be reduced to $Gd_{1.33}Ru_2Al_{10}$ which highlights that it is only more Gd rich than $GdRu_2Al_{10}$. It follows that $Gd_2Ru_3Al_{15}$ may be stabilized over $GdRu_2Al_{10}$ in Gd rich reactions. A reaction with a Gd:Ru:Al ratio of 4:3:24 which was dwelled at 1250 °C for 24 h before being slow cooled to 720 °C at 5 °C/h yielded predominantly $Gd_2Ru_3Al_{15}$. However, the flux poor nature of the reaction only allowed for the growth of small (< 0.5 mm), poorly shaped single crystals of $Gd_2Ru_3Al_{15}$. In order to grow larger single crystals, a more Al rich reaction was prepared. To counteract the increased Al content, which is known to favor the growth of $GdRu_2Al_{10}$, the Ru concentration was lowered. Furthermore, the cooling rate was decreased between 1250 °C to 1150 °C, the temperature range in which it is believed that $Gd_2Ru_3Al_{15}$ grows from the Ce study. A reaction with a Gd:Ru:Al ratio of 4:2:40 was dwelled at 1250 °C for 24 h, slow cooled to 1150 °C at 1 °C/h, and cooled to 1000 °C at 5 °C/h at which

temperature it was removed from the oven. This reaction resulted in one large single crystal (~4 mm on its longest side) surrounded by frozen flux. A bar-shaped single crystal weighing 15.4 mg was mechanically extracted and polished. While the crystal used here was mechanically extracted, the excess flux can also be spun off at 1000 °C. Figure 5.1 shows pictures of the large $Gd_2Ru_3Al_{15}$ single crystal, the polished bar used for physical property measurements, and a 45 mg piece of a single crystal of $Y_2Ru_3Al_{15}$ grown using the same method.

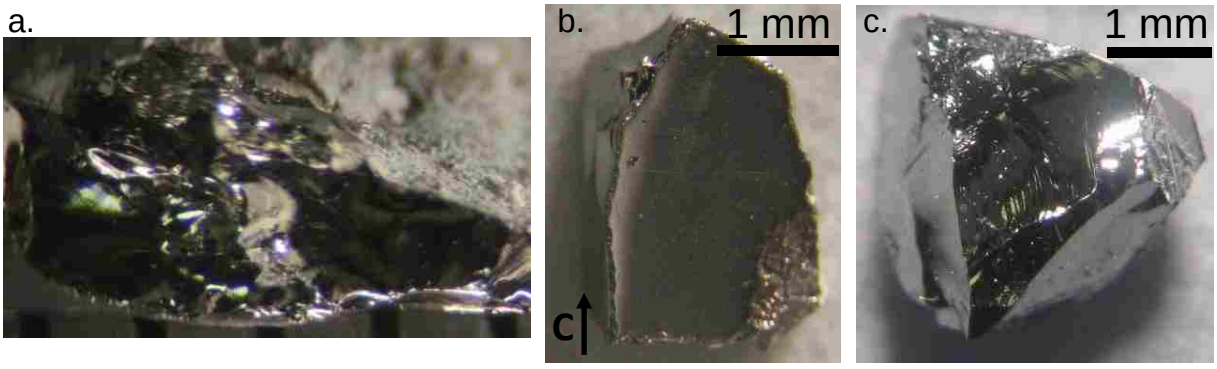


**Figure 5.1 (a)** Single crystal of $Gd_2Ru_3Al_{15.09}$ (b) bar-shaped $Gd_2Ru_3Al_{15.09}$ single crystal used for physical property measurements and (c) single crystal of $Y_2Ru_3Al_{15.04}$.

**Table 5.2** Atomic Coordinates and Atomic Displacement Parameters for $Gd_2Ru_3Al_{15.09}$

| Atom | Wyckoff site | *x* | *y* | *z* | $U_{eq}$ (Å$^2$)[a] | Occ. |
|---|---|---|---|---|---|---|
| Gd(1) | 6*g* | 0.60641(2) | 0 | ¼ | 0.00887(10) | 1 |
| Gd(2) | 2*a* 0.6556(16) | 0 | 0 | ¼ | 0.00782(17) | |
| Gd(3) | 4*e* | 0 | 0 | 0.1917(3) | 0.00782(17) | 0.1722(8) |
| Ru(1) | 12*i* | 0.202841(13) | 0.40568(3) | 0 | 0.00715(11) | 1 |
| Al(1) | 12*k* | 0.79727(10) | 0 | 0.02888(16) | 0.0107(2) | 1 |
| Al(2) | 12*i* | 0.40955(6) | 0.81911(12) | 0 | 0.0095(2) | 1 |
| Al(3) | 12*j* | 0.16565(12) | 0.88007(11) | ¼ | 0.0096(2) | 1 |
| Al(4) | 12*j* | 0.72558(12) | 0.47621(11) | ¼ | 0.0099(3) | 1 |
| Al(5) | 12*k* | 0.61621(10) | 0 | 0.89711(16) | 0.0091(3) | 1 |
| Al(6) | 2*b* | 0 | 0 | 0 | 0.008(3) | 0.1722(8) |

[a] $U_{eq}$ is defined as one-third of the trace of the orthogonalized $U_{ij}$ tensor.

### 5.3.2 Structure

Table 5.2 provides atomic positions for single crystalline $Gd_2Ru_3Al_{15.09}$. $Gd_2Ru_3Al_{15.09}$ is a member of the $Ce_2Ru_3Al_{15}$ structure type[5.12] and crystallizes in the hexagonal space group $P6_3/mcm$ with lattice parameters $a$ = 13.0114(10) Å and $c$ = 9.0552(10) Å. The structure consists of two main Gd sites. As shown in Figure 5.2a, Gd(1) is surrounded by 14 Al and 4 Ru atoms with point group symmetry *mm*. The Gd(1) polyhedra form face sharing columns in the *c*-direction. Each Gd(2) atom is surrounded by 18 Al atoms with point symmetry -6*m*2. The Gd(2) polyhedra form volume sharing columns in the *c*-direction, shown in Figure 5.2b.

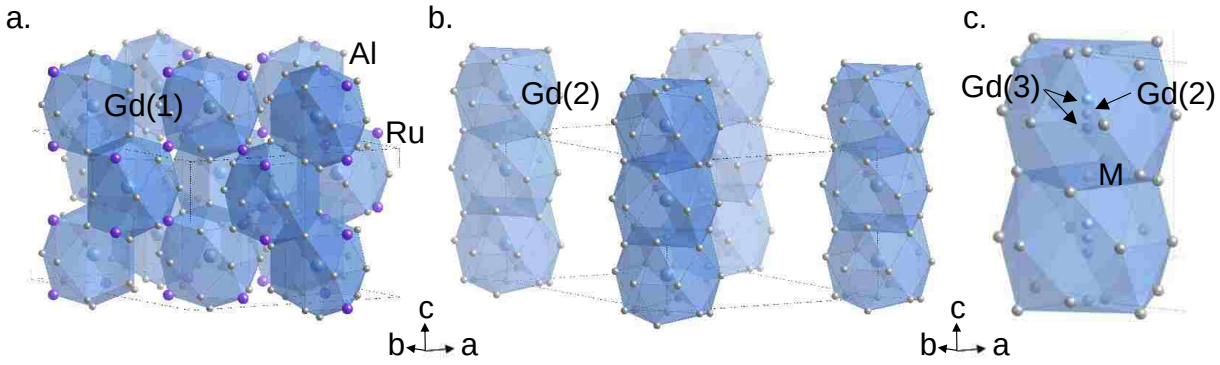


**Figure 5.2** Structure of $Gd_2Ru_3Al_{15.09}$ showing (a) Gd(1) polyhedra (b) Gd(2) polyhedra (c) disorder surrounding the partially occupied M site.

Directly between two Gd(2) atoms lies a partially occupied M atom, shown in Figure 5.2c. When this atom is present, the Gd(2) atom is pushed off a mirror plane onto a Gd(3) site. The identity of the partially occupied site can be determine by comparing the refined occupancy of the Gd(3) site to the refined occupancy of the M as either a Ru atom or an Al atom. For polycrystalline $Gd_2Ru_{3.08}Al_{15}$, the occupancy of the M site refined to 46.5(16)% as an Al atom and 13.5(4)% as a Ru atom. The Gd(3) site was found to be 17.8(4)% occupied indicating that M is a Ru atom. After confining the Gd(3) and M site, Ru(2), occupancies to be equal, the resulting occupancy was 16.49(11)%.[5.9] For single crystalline $Gd_2Ru_3Al_{15.09}$, the M site occupancy refined to 14(4)% as an

Al atom and 3.9(10)% as a Ru atom. The occupancy of the Gd(3) site refined to 17.22(10)%, indicating that the M site is an Al atom. After confining the Gd(3) and M site, Al(6), occupancies to be equal, the resulting occupancy was 17.22(8)%. Despite the different atom types, the two occupancies of the M site are very similar between the single crystalline and polycrystalline samples. This is not unexpected given the similarity of the covalent radii of Ru and Al.[5.13]

The atom identity of the M site appears to be synthesis dependent. Flux grown single crystals of Y, Gd and Tb analogues using the *Ln*:Ru:Al 4:2:40 reaction ratio were all found to have an Al atom on the M site. Likewise, the Al poor Ce flux growths were found to have Al atoms, suggesting that it is not the excess Al that leads to the atomic identity. The only instance in which the M site was found to be a Ru atom was in the arc-melted $Gd_2Ru_{3.08}Al_{15}$. For these reasons, it appears that the identity of the M atom is synthesis method dependent, with the lower temperature and slower cooling flux growth method favoring Al on the site. Unfortunately, no other arc-melted analogues of $Ln_2Ru_3Al_{15}$ yielded X-ray diffraction quality single crystals and the two powder diffraction patterns are too similar to be distinguishable on an in-house powder diffractometer.

As a result of the slightly different structure, the *a* and *c* lattice parameters for single crystalline $Gd_2Ru_3Al_{15.09}$ are 0.0206 Å and 0.0037 Å smaller than for polycrystalline $Gd_2Ru_{3.08}Al_{15}$, respectively. As shown in Table 5.3, all of the Gd-Gd interactions are shorter in the single crystalline analogue than in the polycrystalline analogue. Interestingly, the Gd(3) splitting is more pronounced in the single crystalline $Gd_2Ru_3Al_{15.09}$ despite the smaller lattice parameters.

### 5.3.3 Physical Properties

Figure 5.3 shows the magnetic susceptibility with the field applied parallel to the *ab*-plane and the *c*-direction. At high temperatures, the susceptibility in the two directions overlap. This is

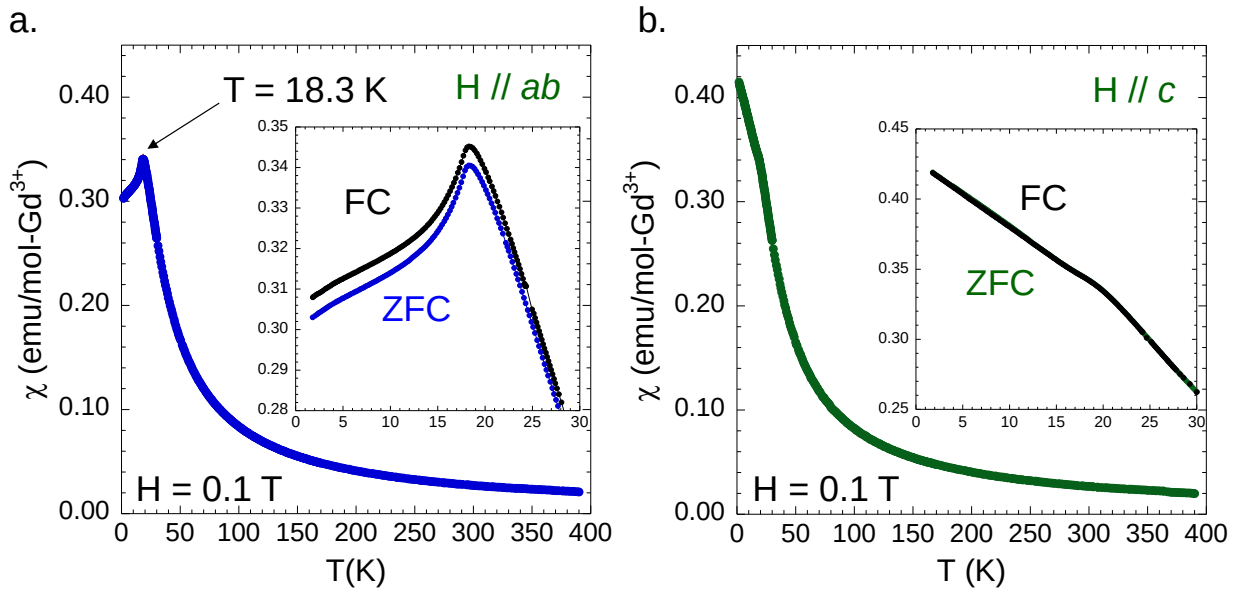


**Figure 5.3** Zero-field-cooled magnetic susceptibility with (a) H // *ab* (b) H // *c*. Insets show the ZFC and FCC susceptibilities at low temperature.

expected as the *f*-electrons in $Gd^{3+}$ are spherically symmetric and therefore, not susceptible to crystalline electric field effects. When H // *ab*, the susceptibility displays an antiferromagnetic ordering at $T_N$ = 18.3 K, similar to what is observed in the polycrystalline analogue. When H // *c*, the susceptibility has a negative slope for all T with only a kink at 18.3 K. This behavior is indicative of an antiferromagnetic ordering with the spins aligned in the *ab*-plane. The fact that the susceptibility with H // *c* does not become temperature independent, as is expected for a canted antiferromagnet, suggests that the magnetic ordering does not involve all three Gd sites.

Polycrystalline $Gd_2Ru_{3.08}Al_{15}$ was found to order at a higher temperature, 21.0 K, than single crystalline $Gd_2Ru_3Al_{15.09}$. As all of the Gd-Gd distances are shorter in the single crystalline analogue than in the polycrystalline analogue, this suggests that the RKKY interaction strengthens with increasing Gd distance. The same behavior was observed in $GdM_2Al_{10}$ (M = Fe, Ru, Os) which has similar Gd-Gd distances.[5.14]

In polycrystalline $Gd_2Ru_{3.08}Al_{15}$, a small upwards deviation was observed in the susceptibility at 150 K. This deviation was believed to be caused by a ferromagnetic impurity, likely $GdAl_2$, whose concentration was below the detection limit of our powder X-ray diffractometer.[5.9] No deviation was observed in single crystalline $Gd_2Ru_3Al_{15.09}$, confirming that this behavior was indeed due to an impurity.

**Table 5.4** Magnetic Properties for $Gd_2Ru_3Al_{15}$

| | H dir. | Fit Range | $\chi_o$(emu/mol-Ln) | $T_N$ (K) | $\theta$ (K) | $\mu_{eff}$ ($\mu_B$) | Ref. |
|---|---|---|---|---|---|---|---|
| $Gd_2Ru_{3.08}Al_{15}$ | | 160-288 | 0.0008(3) | 21.0 | 11.5(17) | 7.97(7) | 5.9 |
| $Gd_2Ru_3Al_{15.09}$ | H // *ab* | 50-300 | -0.00143(4) | 18.3 | -0.38(5) | 8.27(6) | |
| $Gd_2Ru_3Al_{15.09}$ | H //*c* | 50-300 | -0.00148(4) | 18.3 | -0.14(5) | 8.21(6) | |

Table 5.4 summarizes the anisotropic magnetic properties of single crystalline $Gd_2Ru_3Al_{15.09}$ along with the previously reported $Gd_2Ru_{3.08}Al_{15}$ polycrystalline properties.[5.9] Fitting the high temperature, 50-300 K, region of the susceptibility using a modified Curie Weiss law, $\chi = \chi_0 + C/(T - \theta)$, where $\chi_0$ is a temperature independent sum of the diamagnetic and Pauli paramagnetic contributions, yields effective moments of 8.27(6) $\mu_B$/mol-$Gd^{3+}$ (H // *ab*) and 8.21(6) $\mu_B$/mol-$Gd^{3+}$ (H // *c*). While this is somewhat higher than the 7.94 $\mu_B$/mol expected for a free $Gd^{3+}$ ion, no local moment was observed in $Y_2Ru_3Al_{15.04}$, suggesting that the Ru atoms do not carry a moment in $Gd_2Ru_3Al_{15.09}$. From the Curie-Weiss fit, Weiss temperatures, $\theta_N$, of -0.38(5) K (H // *ab*) and -0.14(5) K (H// *c*) were obtained. A $\theta_N$ of ~0 K despite the antiferromagnet ordering suggests that there are ferromagnetic correlations present in the structure. Ferromagnetic correlations were suggested to be between the Gd(2) and partially occupied Gd(3) atoms, thereby preventing the occurrence of long range order.[5.9] These ferromagnetic correlations could explain the bifurcation that arises between the ZFC and FC susceptibilities near the antiferromagnetic ordering when H // *ab*, shown in the inset of Figure 3a. The fact that no such bifurcation was

observed in polycrystalline $Gd_2Ru_{3.08}Al_{15}$ may be due to the large difference in Gd2-Gd3 interaction lengths between the two analogues. Alternatively, a small spin-glass component may be present due to the disorder caused by the partially occupied M site.

Figure 5.4 shows the magnetization as a function of field at 2 K for the two crystallographic directions. When H // *ab*, a metamagnetic transition occurs at H ≈ 1.2 T. This transition is not observed when H // *c*, which is consistent with an antiferromagnet with the spins aligned in the *ab*--plane. The magnitude of the magnetization in each direction is similar and does not saturate up to 7 T, only reaching 4.6 $\mu_B/Gd^{3+}$ (H// *ab*) and 4.4 $\mu_B/Gd^{3+}$ (H// *c*).

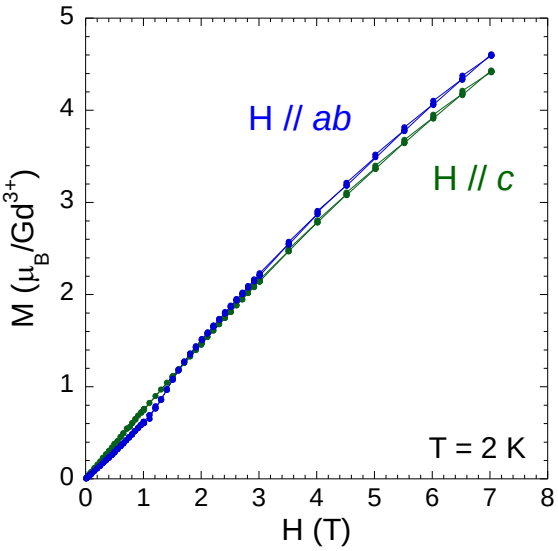


**Figure 5.4** Magnetization as a function of field in the two directions.

Figure 5.5a shows the resistivity as a function of temperature in both measured directions of single crystalline $Gd_2Ru_3Al_{15.09}$. Due to the dimensions of the bar-shaped single crystal, the magnitude of the resistivity with i // *ab* is likely inaccurate. For this reason, only the relative resistivity, $\rho/\rho_{2K}$, is reported for this direction. While the absolute magnitude of the resistivity in the two directions can not be compared, the resistivity is clearly anisotropic, with the resistivity with i // *ab* having a steeper slope than with i // *c*. In both directions, a decrease in the resistivity occurs at 18.3 K, in agreement with a reduction in spin disorder scattering due to the antiferromagnetic ordering. The magnetoresistance, shown in Figure 5.5b, is negative in both directions and reaches -6.3% (i // *ab*) and -4.3% (i // *c*) at 9 T and 2 K. As grain boundaries can

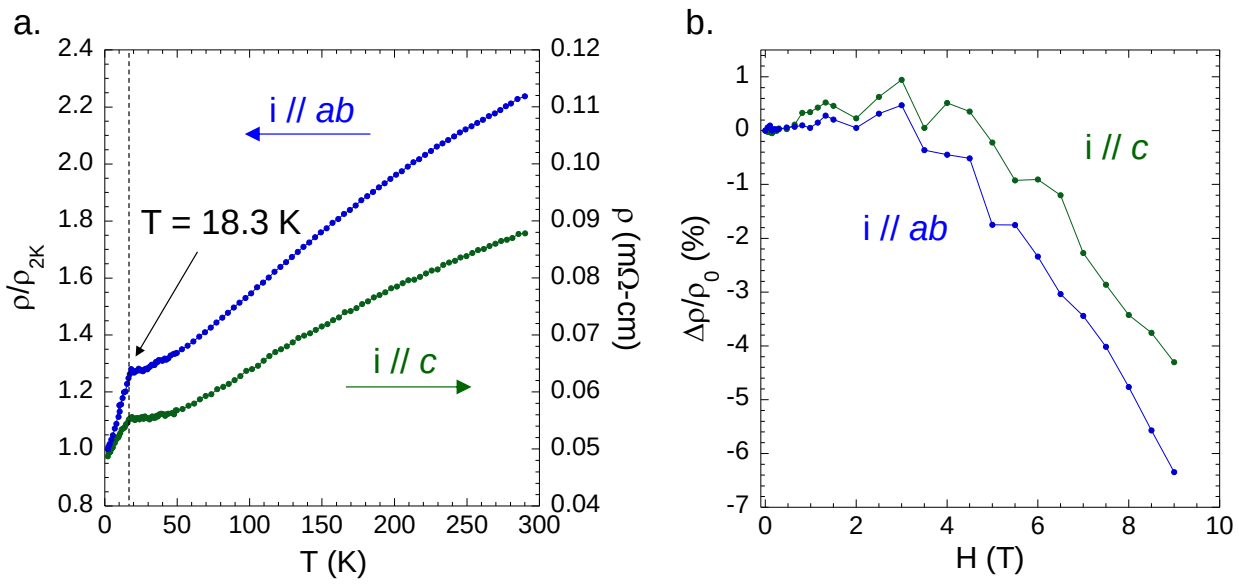


**Figure 5.5** (a) Resistivity and (b) magnetoresistance with current applied in the two directions.

have a large effect on MR,[5.15] the negative MR is most likely intrinsic, while the larger magnitude positive MR observed in polycrystalline $Gd_2Ru_{3.08}Al_{15}$ is likely extrinsic.

## 5.4 Conclusions

$Gd_2Ru_3Al_{15}$ can be stabilized over $GdRu_2Al_{10}$ at high temperatures, i.e. arc-melting, and in Ru poor conditions. Large single crystals of $Gd_2Ru_3Al_{15.09}$ have been grown from a Ru poor melt using the self-flux method. The anisotropic properties of the single crystalline analogue highlights the advantages of single crystals over polycrystalline samples, with single crystals allowing for the study of the intrinsic properties of $Gd_2Ru_3Al_{15.09}$ unaltered by the ferromagnetic impurity that was present in the polycrystalline sample. Furthermore, the anisotropic susceptibility provides information on the type antiferromagnetism observed in the polycrystalline sample. The downturn turn in the susceptibility with H // *ab*, combined with the continuously negative slope with H // *c*, indicates that the antiferromagnetic ordering occurs with the spins aligned in the *ab*-plane. This is consistent with the metamagnetic transition in the magnetization as a function of field with H // *ab*.

Along with providing insight into the magnetic ordering, the single crystalline $Gd_2Ru_3Al_{15.09}$ also exhibits different properties than polycrystalline $Gd_2Ru_{3.08}Al_{15}$. The atomic identity of the partially occupied M site was found to be synthesis method dependent. This change in the structure led to shorted Gd-Gd interactions in the flux grown single crystalline analogue. As a result, the single crystalline analogue orders antiferromagnetically at 18.3 K, which is lower than the 21.0 K ordering of polycrystalline $Gd_2Ru_{3.08}Al_{15}$.

## 5.5 References


5.1. Schmitt, D. C.; Haldolaarachchige, N.; Prestigiacomo, J.; Karki, A.; Young, D. P.; Stadler, S.; Jin, R.; Chan, J. Y., *J. Am. Chem. Soc.* **2013,** *135*, 2748-2758.

5.2. Phelan, W. A.; Menard, M. C.; Kangas, M. J.; McCandless, G. T.; Drake, B. L.; Chan, J. Y., *Chem. Mater.* **2012,** *24*, 409-420.

5.3. Weber, F.; Cosceev, A.; Drobnik, S.; Faißt, A.; Grube, K.; Nateprov, A.; Pfleiderer, C.; Uhlarz, M.; Löhneysen, H. v., *Phys. Rev. B* **2006,** *73*, 014427.

5.4. Thamizhavel, A.; Takeuchi, T.; Okubo, T.; Yamada, M.; Asai, R.; Kirita, S.; Galatanu, A.; Yamamoto, E.; Ebihara, T.; Inada, Y.; Settai, R.; Ōnuki, Y., *Phys. Rev. B* **2003,** *68*, 054427.

5.5. Cao, G.; McCall, S. C.; Crow, J. E.; Guertin, R. P., *Phys. Rev. B* **1997,** *56*, 5387-5394.

5.6. Thomas, E. L.; Moldovan, M.; Young, D. P.; Chan, J. Y., *Chem. Mater.* **2005,** *17*, 5810-5816.

5.7. Drake, B. L.; Capan, C.; Cho, J. Y.; Nambu, Y.; Kuga, K.; Xiong, Y. M.; Karki, A. B.; Nakatsuji, S.; Adams, P. W.; Young, D. P.; Chan, J. Y., *J. Phys. Condens. Matter* **2010,** *22*, 066001.

5.8. Felner, I.; Nowik, I., *J. Phys. Chem. Solids* **1979,** *40*, 1035-1044.

5.9. Morrison, G.; Haldolaarachchige, N.; Chen, C.-W.; Young, D. P.; Morosan, E.; Chan, J. Y., *Inorg. Chem.* **2013,** *52*, 3198-3206.

5.10. Altomare, A.; Burla, M. C.; Camalli, M.; Cascarano, G.; Giacovazzo, C.; Guagliardi, A.; Moliterni, A. G. G.; Polidori, G.; Spagna, R., *J. Appl. Crystallogr.* **1999,** *32*, 115.

5.11. Sheldrick, G. M., *Acta Crystallogr. Sect. A* **2008,** *64*, 112-122.

5.12. Tursina, A. I.; Murashova, E. V.; Nesterenko, S. N.; Chernyshev, I. V.; No; l, H.; Seropegin, Y. D., *Acta Crystallogr. Sect. E* **2004,** *60*, i145-i146.

5.13. Emsley, J., *The Elements*. 2 ed.; Oxford University Press: New York, 1991.

5.14. Morrison, G.; Haldolaarachchige, N.; Young, D. P.; Chan, J. Y., *J. Phys. Condens. Matter* **2012,** *24*, 356002.

5.15. Tomioka, Y.; Okuda, T.; Okimoto, Y.; Kumai, R.; Kobayashi, K. I.; Tokura, Y., *Phys. Rev. B* **2000,** *61*, 422-427.

## Chapter 6. Highly Anisotropic Properties due to Strong Crystalline Electric Field Effects in $Tb_2Ru_3Al_{15.05}$

### 6.1 Introduction

The non-spherical crystalline electric field (CEF) surrounding the lanthanide's *f*-orbitals of Ln containing intermetallics (Ln = Ce-Eu, Tb-Yb) can affect their magnetic properties in many ways. Common CEF effects include non-magnetic[6.1, 2] or reduced moment ground states, anisotropic magnetization,[6.3-5] and deviation from Curie-Wiess behavior.[6.6-8] In some cases, CEFs can lead to highly anisotropic properties. For example, in TmAgGe, the anisotropy of the magnetic susceptibility, $\chi_{ab}/\chi_{c}$, reaches 30 at T = 5.0 K. Furthermore, field dependent magnetization has a series of metamagnetic transitions with H // [1 2 0] which are not observed for H // [0 1 0].[6.9] Similarly, a large splitting energy of 370 K between the ground state and first excited state leads to highly anisotropic magnetism in $CeRh_2Si_2$.[6.10] Despite the highly anisotropic magnetism, in both of these compounds the magnetic transitions are observed in both axial directions.[6.9, 10] This is not the case in $HoNi_2B_2C$, where a splitting energy of ~90 K between the low-lying energy levels and the next set of energy levels leads to a broad hump in the susceptibility with H // *c* which is not observed with H // *ab*.[6.3] However, even in this compound, the 5 K antiferromagnetic order is observed with both H // *ab* and H // *c*,[6.11] indicating that the polarization of the moment into the *ab*-plane is not complete.

We have studied three families of compounds which are structurally related to $CeRu_2Al_{10}$ and all contain very similar Ln environments: $LnRu_2Al_{10}$ (Ln = Pr, Gd, Yb),[6.12] $CeRu_4(Al,Si)_{15.58}$,[6.13] and $Ln_2Ru_3Al_{15}$ (Ln = Ce, Gd).[6.14] Crystalline electric field effects were found to result in a nonmagnetic ground state in $PrRu_2Al_{10}$ at 13.2 K[6.12] and lead to a deviation from Curie-Weiss behavior in $Ce_2Ru_3Al_{15}$.[6.14] Furthermore, the magnetization of $CeRu_2Al_{10}$ was found to be anisotropic and the first two splitting energies were calculated to be 500 and 760 K.[6.5]

The CEF effects observed in these structurally related compounds, combined with our recent ability to grow large single crystals of $Ln_2Ru_3Al_{15}$ for latter rare earths,[6.15] made it of interest to further study CEF effects in $Ln_2Ru_3Al_{15}$. Herein, we report the anisotropic magnetization of $Tb_2Ru_3Al_{15.05}$.

## 6.2 Experimental

### 6.2.1 Synthesis

A single crystal of $Tb_2Ru_3Al_{15.05}$ was grown using the self-flux growth conditions reported for $Gd_2Ru_3Al_{15.09}$.[6.15] Tb (pieces, 99.9 % REO), Ru (powder, 99.98 % metal basis excluding Ca) and Al (shot, 99.999 %) were used as received. A Tb:Ru:Al ratio of 4:2:40 was placed in an alumina crucible, covered with a second crucible, and sealed in a fused-silica tube. The tube was sealed under a partial pressure (~ 1/6 atm) in order to help maintain its integrity at high temperatures. The reaction was rapidly heated to 1250 °C, dwelled for 24 h, slow cooled at 1 °C/h to 1150 °C, and cooled to 1000 °C at 5 °C/h. It was then removed from the oven, inverted, and spun in a centrifuge to remove the excess flux. This growth resulted in one large single crystal (3-

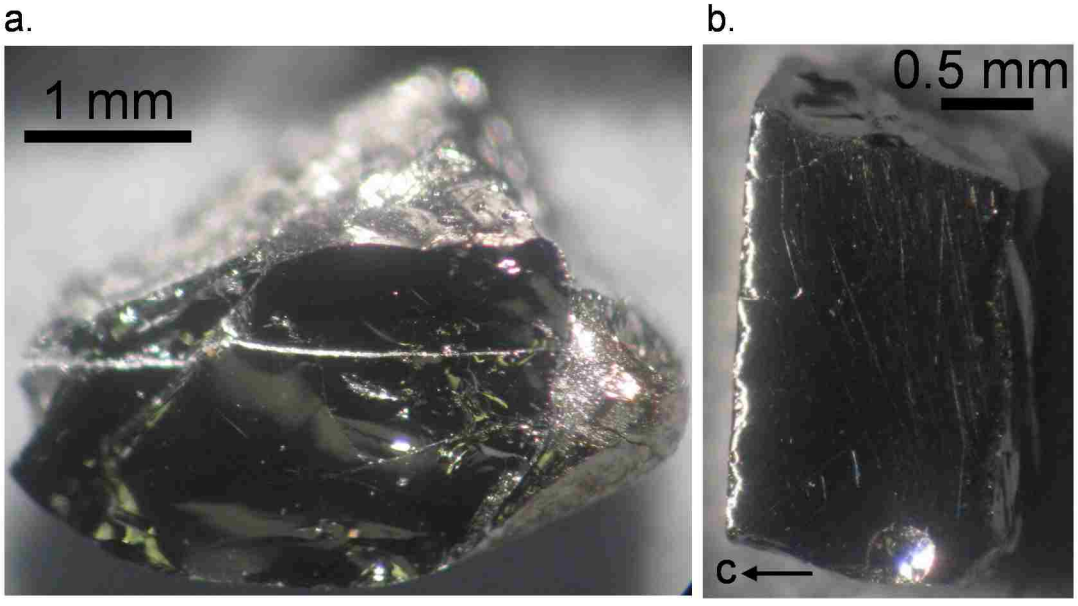


**Figure 6.1** (a) Large single crystal of $Tb_2Ru_3Al_{15.05}$ and (b) bar-shaped single crystal used for physical property measurements.

4 mm on each side), as shown in Figure 6.1a. A single crystal of suitable size for physical property measurements, shown in Figure 6.1b, was mechanically extracted from the larger single crystal and polished into a bar shape.

### 6.2.2 Structure

Single crystal X-ray diffraction data was collected using an Enraf Nonius KappaCCD diffractometer equipped with a Mo Kα source (λ = 0.71073 Å). An initial structural model was obtained with direct methods using SIR97[6.16] which was then refined using SHELXL-97.[6.17] A summary of crystallographic data and atomic positions can be found in Tables 6.1 and 6.2, respectively. Orientation of the bar shaped single crystal was also done using X-ray diffraction

**Table 6.1** Crystallographic Data for $Tb_2Ru_3Al_{15.05}$

| Formula | **$Tb_2Ru_3Al_{15.05}$** |
|---|---|
| Space group | $P6_3/mcm$ |
| a (Å) | 13.0072(10) |
| c (Å) | 9.0289(10) |
| V (Å$^3$) | 1322.9(2) |
| Z | 4 |
| Crystal dimensions (mm$^3$) | 0.07 x 0.07 x 0.10 |
| Temperature (K) | 295(1) |
| Density (g cm$^{-3}$) | 5.156 |
| θ Range (°) | 1.81-30.97 |
| μ (mm$^{-1}$) | 14.866 |
| | |
| Data Collection and Refinement | |
| Collected reflections | 5257 |
| Unique reflections | 795 |
| $R_{int}$ | 0.0296 |
| h | $-18 \le h \le 18$ |
| k | $-15 \le k \le 15$ |
| l | $-12 \le l \le 13$ |
| $\Delta\rho_{max}$ (e Å$^{-3}$) | 1.721 |
| $\Delta\rho_{min}$ (e Å$^{-3}$) | -1.506 |
| GoF | 1.154 |
| Extinction coefficient | 0.00106(8) |
| [a] $R_1(F)$ for $F_o^2 > 2\sigma(F_o^2)$ | 0.0229 |
| [b] $R_w(F_o^2)$ | 0.0548 |

[a] $R_1 = \Sigma||F_0| - |F_c||/\Sigma|F_0|$

[b] $wR_2 = [\Sigma w(F_o^2 - F_c^2)^2/\Sigma w(F_0^2)^2]^{1/2}$; $P = (F_o^2 + 2F_c^2)/3$; $w = 1/[\sigma^2(F_o^2) + (0.0223P)^2 + 6.5326P]$

data collected on three non-confacial corners of the crystal in order to ensure that the bar was a single crystal with one orientation throughout. The *c*-direction was found to be the medium axis of the bar, labeled in Figure 6.1b. The *a* and *b* axes did not align with macroscopic axes of the bar. For this reason, properties will be reported as parallel to the *c*-direction and parallel to the *ab*-plane.

**Table 6.2** Atomic Coordinates and Atomic Displacement Parameters for $Tb_2Ru_3Al_{15.05}$

| Atom | Wyckoff site | x | y | z | $U_{eq}$ (Å$^2$)[a] | Occ. |
|---|---|---|---|---|---|---|
| Tb(1) | 6g | 0.60706(2) | 0 | ¼ | 0.00926(11) | 1 |
| Tb(2) | 2a | 0 | 0 | ¼ | 0.00834(17) | 0.813(2) |
| Tb(3) | 4e | 0 | 0 | 0.2036(6) | 0.00834(17) | 0.0935(10) |
| Ru(1) | 12i | 0.202956(15) | 0.40591(3) | 0 | 0.00695(11) | 1 |
| Al(1) | 12k | 0.79804(11) | 0 | 0.02806(17) | 0.0102(3) | 1 |
| Al(2) | 12i | 0.40950(6) | 0.81901(13) | 0 | 0.0095(3) | 1 |
| Al(3) | 12j | 0.16506(13) | 0.87981(12) | ¼ | 0.0095(3) | 1 |
| Al(4) | 12j | 0.72605(13) | 0.47679(13) | ¼ | 0.0105(3) | 1 |
| Al(5) | 12k | 0.61580(11) | 0 | 0.89771(17) | 0.0095(3) | 1 |
| Al(6) | 2b | 0 | 0 | 0 | 0.032(11) | 0.0935(10) |

[a]$U_{eq}$ is defined as one-third of the trace of the orthogonalized $U_{ij}$ tensor.

Elemental analysis was performed via energy dispersive X-ray spectroscopy, EDS, using an FEI Quanta 200 SEM equipped with an EDAX detector. Six data points were collected on each of two clean cut faces of a single crystal of $Tb_2Ru_3Al_{15}$ and provided an average composition of $Tb_{2.00(13)}Ru_{3.72(16)}Al_{22.4(8)}$.

### 6.2.3 Physical Properties

Anisotropic magnetic properties were collected for H // *ab* and H // *c* on a Quantum Design Magnetic Property Measurement System (QD-MPMS). Magnetic susceptibility was collected under zero-field-cooled (ZFC) and field-cooled (FC) conditions from 2-395 K at H = 0.1 T and magnetization as a function of field was collected at 2 K for H = 0-7 T. Further magnetic

susceptibility measurements were collected for H // *ab* on a Quantum Design Physical Property Measurement System (QD-PPMS) under ZFC and FC conditions from 3-290K at H = 2 and 5 T. Resistivity for T = 3-290 K and magnetoresistance was measured for H = 0-9 T with i // *ab* and i // *c* on the QD-PPMS.

## 6.3 Results and Discussion

### 6.3.1 Structure

$Tb_2Ru_3Al_{15.05}$ contains three unique Tb sites. Table 6.3 provides Tb contacts less than 3.7 Å. Tb(1), which constitutes 75% of the Tb atoms, is surrounded by 14 Al atoms and 4 Ru atoms with point symmetry *mm*. As shown in Figure 6.2a, the mirrors lie in the *ab* and *ac*-planes. The Tb(1) polyhedra form face-sharing columns in the *c*-direction. Due to the hexagonal symmetry of the structure, there are three different orientations of the columns, each a 120° rotation from the others. Likewise, there are three orientations of the mirror planes in the *ac*-direction, with each polyhedron containing one of the mirror planes. Tb(2), which constitutes 20.33(5)% of the Tb atoms, is surrounded by 18 Al atoms with point symmetry *mm*. Like with Tb(1), these mirror planes lie in the *ab* and *ac*-planes. However, as shown in Figure 6.2b, each polyhedron contains

**Table 6.3** Selected Interatomic Distances in $Tb_2Ru_3Al_{15.05}$ (Å)

| Interaction | Distance (Å) | Interaction | Distance (Å) |
|---|---|---|---|
| Tb(1)-Ru(1) (x4) | 3.4128(2) | Tb(2)-Al(1) (x6) | 3.3040(14) |
| Tb(1)-Al(1) (x2) | 3.1917(15) | Tb(2)-Al(1) (x6) | 3.6337(15) |
| Tb(1)-Al(2) (x4) | 3.3453(9) | Tb(2)-Al(3) (x6) | 3.2265(15) |
| Tb(1)-Al(3) (x2) | 3.0951(14) | Tb(3)-Al(1) (x3) | 3.068(3) |
| Tb(1)-Al(4) (x2) | 3.0872(15) | Tb(3)-Al(1) (x3) | 3.358(4) |
| Tb(1)-Al(5) (x2) | 3.1828(16) | Tb(3)-Al(1) (x3) | 3.574(4) |
| Tb(1)-Al(5) (x2) | 3.1908(15) | Tb(3)-Al(3) (x6) | 3.2536(16) |
| | | Tb(3)-Al(6) (x1) | 2.676(6) |

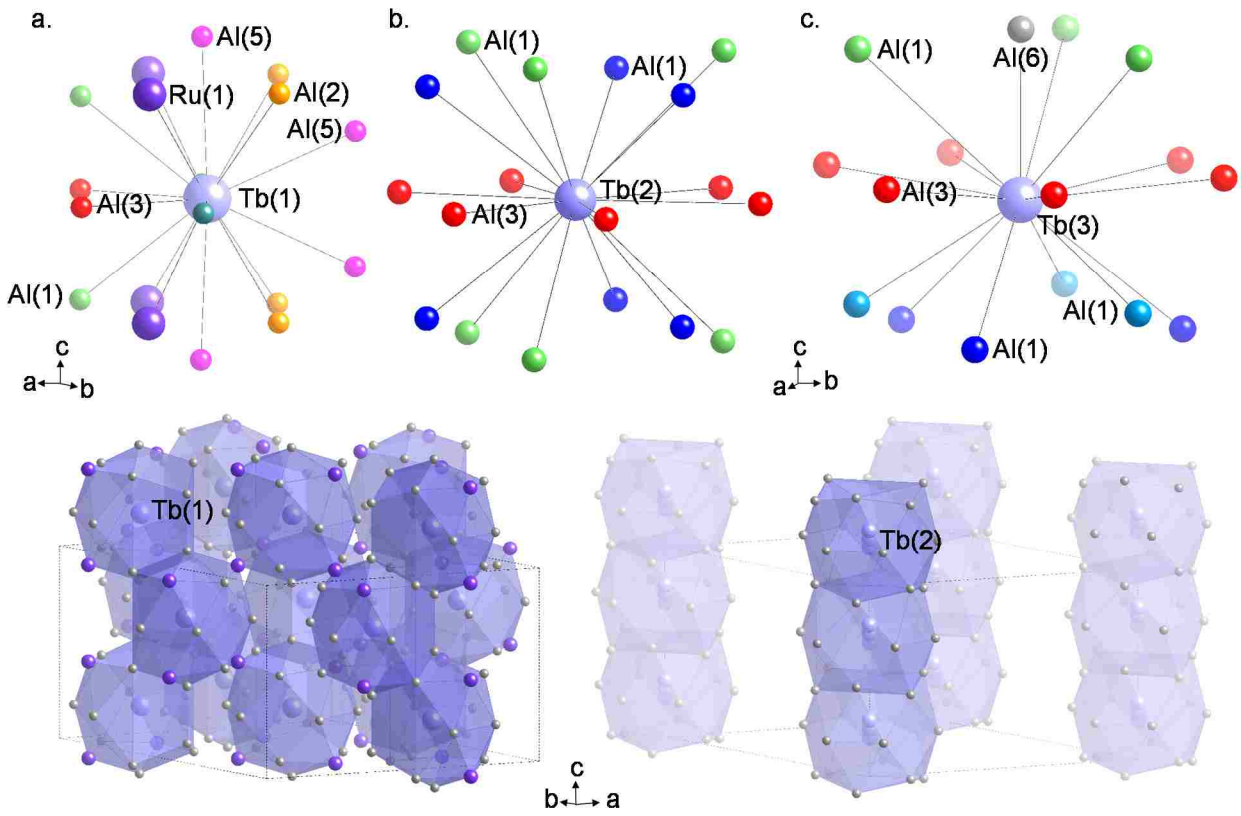


**Figure 6.2** Structure of $Tb_2Ru_3Al_{15.05}$ showing the three Tb environments and the packing of the Tb polyhedra.

all three mirror planes in the ac-direction. The Tb(2) polyhedra from volume-sharing polyhedra in the *c*-direction. Directly in between two adjacent Tb(2) atoms is a partially occupied Al(6) atom. When this atom is present, the two neighboring Tb(2) atoms deviate from the *ab* mirror plane onto a Tb(3) site. Tb(3), which constitutes 4.67(5)% of the Tb atoms, is surrounded by 16 Al atoms with point symmetry *m*. As shown in Figure 6.2c, the Tb(3) polyhedra still contain the three *ac* mirror planes but, unlike the Tb(1) and Tb(2) polyhedra, do not contain the *ab* mirror plane.

### 6.3.2 Properties

Table 6.4 summarizes the anisotropic magnetic data for $Tb_2Ru_3Al_{15.05}$. Figure 6.3 shows the anisotropic magnetic susceptibility of $Tb_2Ru_3Al_{15.05}$ with H parallel to the *ab*-plane and

*c*-direction. For H // *ab*, three successive magnetic transitions occur at low temperatures, shown in the top inset. At ~17 K, the system enters a reduced moment ground state due to crystalline electric field effects. An upturn at 16.7 K suggests a partial ferromagnetic ordering followed by an antiferromagnetic ordering at 15.2 K. The large magnitude change at 15.2 K, as compared to most antiferromagnetic transitions, is due to the overlap of the antiferromagnetic ordering and the reduced moment ground state. A small bifurcation between the zero-field-cooled and field-cooled (not shown) susceptibilities, is consistent with a partial ferromagnetic ordering. Fitting the high temperature susceptibility with a modified Curie-Weiss law, $\chi = \chi_0 + C/(T - \theta)$, where $\chi_0$ is a temperature independent sum of the diamagnetic and Pauli paramagnetic contributions, yields an effective moment of 9.462(15) $\mu_B/Tb^{3+}$, smaller than the 9.72 $\mu_B$ expected for a free $Tb^{3+}$, and a Weiss-temperature of 12.8(3) K. As will be discussed later, these values are likely the result of a deviation for Curie-Weiss behavior due to CEF effects.

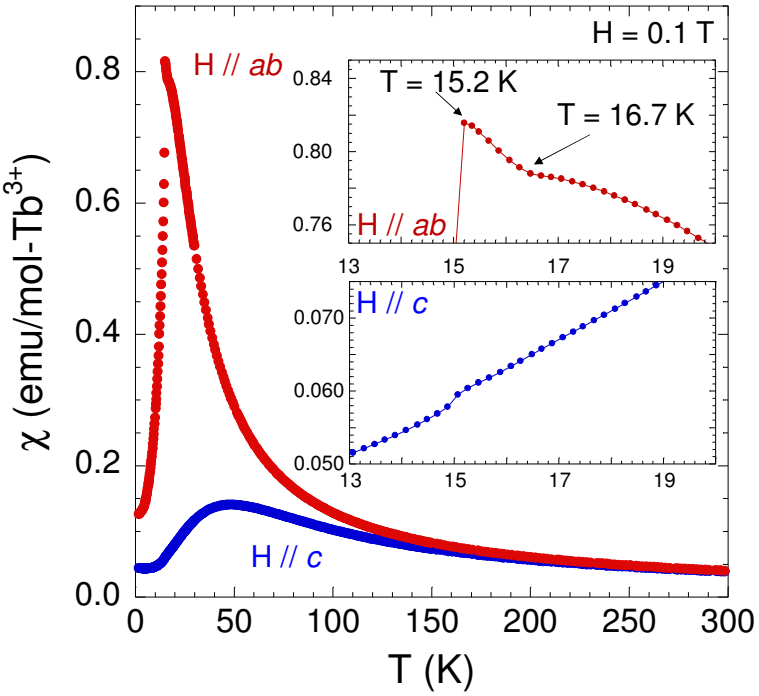


**Figure 6.4** Magnetic susceptibility of $Tb_2Ru_3Al_{15.05}$.

**Table 6.4** Magnetic Properties for $Tb_2Ru_3Al_{15.05}$

| | H dir. | Field (T) | Fit Range | $\chi_o$(emu/mol-Ln) | $T_N$ (K) | θ (K) | $\mu_{eff}(\mu_B)$ |
|---|---|---|---|---|---|---|---|
| $Tb_2Ru_3Al_{15.05}$ | H // *ab* | 0.1 | 150-390 | 0.00070(8) | 15.2 | 12.8(3) | 9.462(15) |
| $Tb_2Ru_3Al_{15.05}$ | H // *ab* | 2 | 150-295 | -0.00215(10) | - | 9.7(4) | 9.554(18) |
| $Tb_2Ru_3Al_{15.05}$ | H // *ab* | 5 | 150-295 | -0.00398(16) | - | 5.0(5) | 9.81(3) |
| $Tb_2Ru_3Al_{15.05}$ | H // *c* | 0.1 | 150-390 | 0.00008(10) | - | -13.5(6) | 9.78(2) |

The magnetic susceptibility with H // *c* does not resemble the susceptibility with H // *ab*. Instead, the system appears to enter a reduced moment ground state at 49 K with no indication of the three low temperature transitions observed in the other direction. This suggests that the 49 K transition is not a reduced moment ground state but is instead the result of CEF effects completely polarizing a portion of the moment, likely the moment from Tb(1), into the *ab* plane. The bottom inset of Figure 6.3, shows the susceptibility for H // *c* at 15 K, highlighting how complete the polarization is and how accurate the crystal alignment is. Fitting the susceptibility from 150-390 K yields an effective moment of 9.78(2) $\mu_B$/$Tb^{3+}$ and a $\theta_N$ of –13.5(6) K. The good agreement between these values and the values expected for a free $Tb^{3+}$ ion and a 15.2 K antiferromagnet, respectively, suggests that the high temperature susceptibility is less affected by the CEF with H // *c* than *ab*.

Figure 6.4 shows the magnetization as a function of field at 2 K for $Tb_2Ru_3Al_{15.05}$. When H // *c*, at low fields the magnetization is small and linear, consistent with the susceptibility. Starting at ~ 5 T, the magnetization begins to increase above linearity, which may be due to the large applied field disrupting the crystalline electric field effects. When H // *ab*, the magnetization is initially linear up to 0. 8 T, at which field it undergoes the first of 3-4 metamagnetic transitions. At H ~ 4

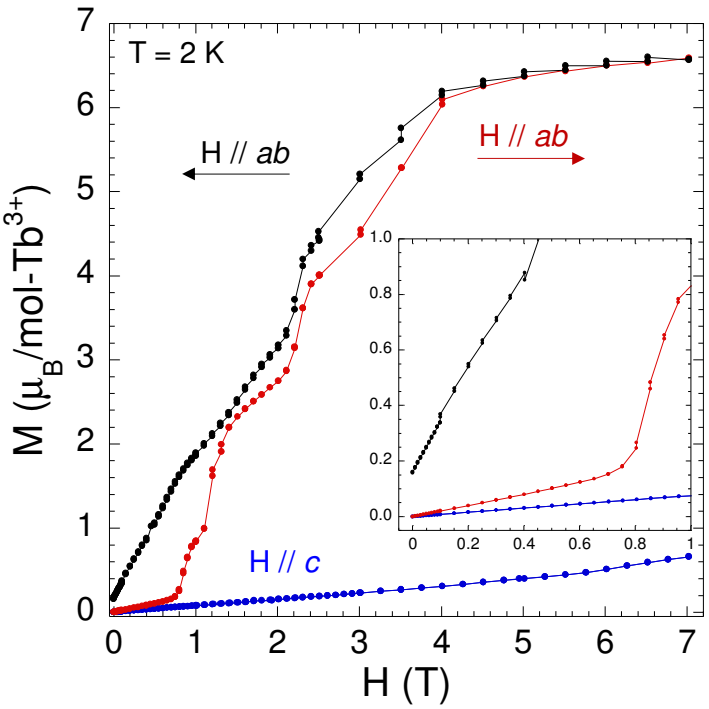


**Figure 6.4** Field dependent magnetization of $Tb_2Ru_3Al_{15.05}$.

T, the magnetization saturates at 6.6 $\mu_B$/mol-$Tb^{3+}$ which is less than the 9 $\mu_B$ expected for a free $Tb^{3+}$ ion and is consistent with a reduced moment ground state. The magnetization under descending field with H // *ab* does not overlay with the ascending field magnetization. This hysteresis may be due to the ferromagnetic component observed in the susceptibility. Interestingly, only two of the metamagnetic transitions are observed under descending field and the system does not revert back to its original state down to zero field.

To investigate the origin of the metamagnetic transitions observed in the magnetization as a function of field, the magnetic susceptibility was measured at the plateaus at 2 and 5 T, shown in Figure 6.5. When H = 2 T, the antiferromagnetic ordering has been disrupted, leaving the reduced moment ground state and a brief spike in the susceptibility at 16.0 K, whose origin is unclear. The bifurcation observed at 0.1 T is still present at 2 T. When H = 5 T, the susceptibility saturates at 6.3 $\mu_B$/mol-$Tb^{3+}$, similar to the saturated moment observed in the magnetization as a function of field and consistent with a reduced moment ground state. No magnetic transitions are observed, presumably because the spins are almost saturated at the temperatures the orderings would occur.

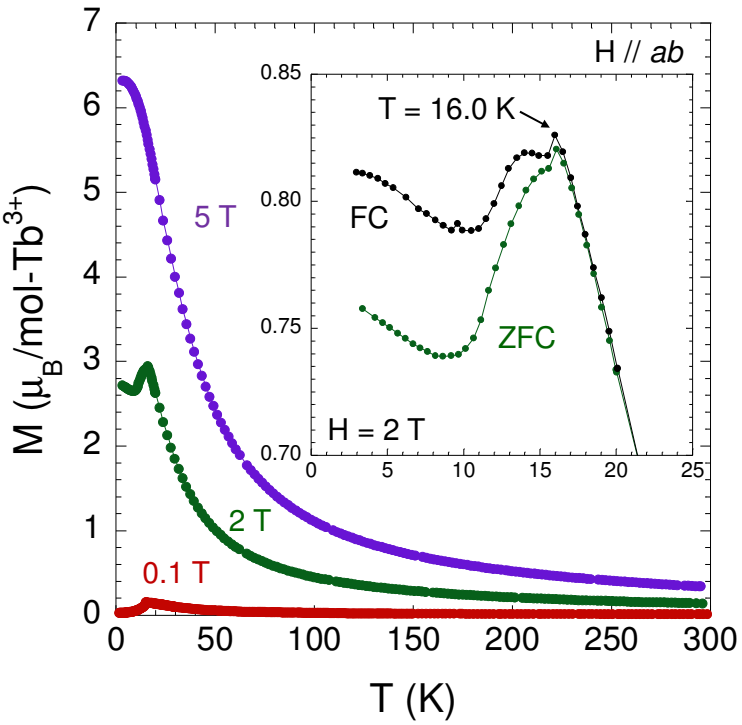


**Figure 6.4** Magnetic susceptibility of $Tb_2Ru_3Al_{15.05}$ at several field strengths with H // *ab*.

Finally, the temperature at which the system enters its reduced moment ground state has been reduced, as is expected for an applied external field.

As shown in Table 6.4, fitting the high temperature magnetic susceptibility with H // *ab* at 0.1 T yields an effective moment of 9.462(15) $\mu_B/Tb^{3+}$ and a positive Weiss temperature of 12.8(3) K. Under an applied field of 2 T, the effective moment was found to be 9.554(18) $\mu_B/Tb^{3+}$ with $\theta_N$ of 9.7(4) K. Finally at H = 5 T, a Curie-Weiss fit yields an effective moment of 9.81(3) $\mu_B/Tb^{3+}$ and a Weiss temperature of 5.0(5) K. The increase in the moment and the decrease in the $\theta_N$ with increased field suggest that the positive Weiss temperature and reduced moment with H // *ab* are the effect of deviations from Curie-Weiss behavior due to the crystalline electric field.

## 6.4 Conclusions

The magnetic properties of $Tb_2Ru_3Al_{15.05}$ are highly anisotropic due to strong crystalline electric field effects. Three successive magnetic transitions are observed in the magnetic susceptibility with H // *ab*, the most prominent of which is an antiferromagnetic ordering at 15.2 K. These transitions are not observed with H // *c*. Instead, a broad transition at T ≈ 49 K is indicative of a portion of the moment, likely the Tb(1) moment, being polarized into the *ab*-plane. Furthermore, the magnetization as a function of field, is small and linear with H // *c* whereas when H // *ab*, a series of metamagnetic transitions are observed, leading to a saturation of the moment at ~ 4 T.

Several compounds have been reported with highly anisotropic magnetic properties due to crystalline electric field effects. However, in all of these compounds, the low temperature magnetic transitions are observed with the external field applied in all directions, indicating that the polarization of the spins is not absolute. $Tb_2Ru_3Al_{15.05}$ is unique in that a portion of the magnetic moment appears to be completely polarized into the *ab*-plane. This polarization,

combined with the ability to easily grow large single crystals, makes $Tb_2Ru_3Al_{15.05}$ an ideal subject for further studies, such as neutron scattering experiments.

### 6.5 References


6.1. Sakai, A.; Nakatsuji, S., *J. Phys. Soc. Jpn.* **2011,** *80*, 063701.

6.2. Muro, Y.; Kajino, J.; Onimaru, T.; Takabatake, T., *J. Phys. Soc. Jpn.* **2011,** *80*, SA021.

6.3. Cho, B. K.; Harmon, B. N.; Johnston, D. C.; Canfield, P. C., *Phys. Rev. B* **1996,** *53*, 2217-2220.

6.4. Prestigiacomo, J.; Schmitt, D. C.; Chan, J. Y.; Young, D. P.; Adams, P. W., *In Preparation* **2013**.

6.5. Hanzawa, K., *J. Phys. Soc. Jpn.* **2011,** *80*, 023707.

6.6. Xing, H.; Long, G.; Guo, H.; Zou, Y.; Feng, C.; Cao, G.; Zeng, H.; Xu, Z.-A., *J. Phys. Condens. Matter* **2011,** *23*, 216005.

6.7. Fujii, H.; Inoue, T.; Andoh, Y.; Takabatake, T.; Satoh, K.; Maeno, Y.; Fujita, T.; Sakurai, J.; Yamaguchi, Y., *Phys. Rev. B* **1989,** *39*, 6840-6843.

6.8. Lee, W. H.; Kwan, K. S.; Klavins, P.; Shelton, R. N., *Phys. Rev. B* **1990,** *42*, 6542-6545.

6.9. Morosan, E.; Bud'ko, S. L.; Canfield, P. C.; Torikachvili, M. S.; Lacerda, A. H., *J. Magn. Magn. Mater.* **2004,** *277*, 298-321.

6.10. Abe, H.; Kitazawa, H.; Suzuki, H.; Kido, G.; Matsumoto, T., *J. Magn. Magn. Mater.* **1998,** *177–181*, 479-480.

6.11. Canfield, P. C.; Cho, B. K.; Johnston, D. C.; Finnemore, D. K.; Hundley, M. F., *Physica C* **1994,** *230*, 397-406.

6.12. Morrison, G.; Haldolaarachchige, N.; Young, D. P.; Chan, J. Y., *J. Phys. Condens. Matter* **2012,** *24*, 356002.

6.13. Morrison, G. W.; Menard, M. C.; Treadwell, L. J.; Haldolaarachchige, N.; Kendrick, K. C.; Young, D. P.; Chan, J. Y., *Philos. Mag.* **2012,** *92*, 2524-2540.

6.14. Morrison, G.; Haldolaarachchige, N.; Chen, C.-W.; Young, D. P.; Morosan, E.; Chan, J. Y., *Inorg. Chem.* **2013,** *52*, 3198-3206.

6.15. Morrison, G.; Haldolaarachchige, N.; Young, D. P.; Stadler, S.; Chan, J. Y., *In Preparation* **2013**.

6.16. Altomare, A.; Burla, M. C.; Camalli, M.; Cascarano, G.; Giacovazzo, C.; Guagliardi, A.; Moliterni, A. G. G.; Polidori, G.; Spagna, R., *J. Appl. Crystallogr.* **1999,** *32*, 115.

6.17. Sheldrick, G. M., *Acta Crystallogr. Sect. A* **2008,** *64*, 112-122.

# Chapter 7. Single Crystal X-ray Diffraction of α- and β-$YbAl_{1-x}Fe_xB_4$

## 7.1 Introduction

$YbAlB_4$ exists as two polymorphs. α-$YbAlB_4$ is a member of the $YCrB_4$ structure type and crystallizes in the noncentrosymmetric space group *Pbam*.[7.1] The Yb atoms have an intermediate valence of +2.73[7.2] and the system has a heavy Fermi liquid ground state.[7.3] β-$YbAlB_4$ crystallizes in the $ThMoB_4$ structure type with the space group *Cmmm*.[7.1] Like the α- polymorph, β-$YbAlB_4$ has an intermediate Yb valence of +2.75[7.2] and is a heavy fermion system.[7.1] β-$YbAlB_4$ has a superconducting ground state with $T_c$ ~ 80 mK and $H_{c2}$ ~ 30 mT. In this superconducting state, quantum criticality arises without any field or pressure tuning. Quantum criticality is noteworthy within β-$YbAlB_4$ as it is the first example of a quantum critical point (QCP) without the need for tuning and is also the first instance of a quantum critical heavy fermion system with a non-integer valence.[7.4]

A quantum critical point is a point at which the temperature of a phase transition is depressed to 0 K and is of interest as the suppression of the normal state can lead to novel or new states of matter. Typically, a quantum critical point is reached through the tuning of a non-temperature parameter such as pressure or dopant concentration. For example, a magnetic field of 0.66 T can tune the antiferromagnetic ordering of $YbRh_2Si_2$ to T = 0 K.[7.5] Similarly, at x = 0.32, $BaFe_2(As_{1-x}P_x)_2$ exists at a QCP which corresponds with the suppression of a spin-density wave and emergence of a superconducting state.[7.6]

In some special cases, such as $YFe_2Al_{10}$[7.7] and β-$YbAlB_4$,[7.4] a compound exists at a quantum critical point without the need for any tuning. This makes the normal state of the system difficult to determine as it has been completely suppressed. In $YFe_2Al_{10}$, the normal state is believed to be characterized by the ferromagnetic ordering of localized Fe moments. In order to

study the suppressed ordered state of β-$YbAlB_4$, single crystals of α- and β-$YbAl_{1-x}Fe_xB_4$ have been prepared.[7.8] Herein, single crystal X-ray diffraction is used to study the effect of Fe doping on the structure of α- and β-$YbAl_{1-x}Fe_xB_4$ at 295 and 100 K.[7.8]

**Table 7.1**† Crystallographic Data for α-$YbAl_{0.93}Fe_{0.07}B_4$, β-$YbAl_{0.97}Fe_{0.03}B_4$, and β-$YbAl_{0.97}Fe_{0.03}B_4$ at 295(3) and 100(1) K

| Formula | **α-$YbAl_{0.93}Fe_{0.07}B_4$** | | **β-$YbAl_{0.97}Fe_{0.03}B_4$** | | **β-$YbAl_{0.97}Fe_{0.05}B_4$** | |
|---|---|---|---|---|---|---|
| Temperature (K) | 295(3) | 100(1) | 295(3) | 100(1) | 295(3) | 100(1) |
| Space group | P*bam* | P*bam* | C*mmm* | C*mmm* | C*mmm* | C*mmm* |
| *a* (Å) | 5.9184(6) | 5.9167(6) | 7.3075(9) | 7.3015(12) | 7.3023(12) | 7.3013(12) |
| *b* (Å) | 11.4645(15) | 11.4602(15) | 9.3178(15) | 9.3133(12) | 9.3178(12) | 9.3130(12) |
| *c* (Å) | 3.4832(6) | 3.4780(4) | 3.4971(6) | 3.4892(6) | 3.4917(6) | 3.4852(6) |
| *V* (Å$^3$) | 236.34(6) | 235.83(4) | 238.1(3) | 237.27(6) | 237.58(6) | 236.98(6) |
| *Z* | 4 | 4 | 4 | 4 | 4 | 4 |
| Crystal dimensions (mm$^3$) | 0.07x0.13x0.17 | | 0.01x0.07x0.07 | | 0.01x0.07x0.07 | |
| Density (g cm$^{-3}$) | 6.894 | 6.904 | 6.787 | 6.811 | 6.801 | 6.819 |
| $\theta$ Range (°) | 3.55-31.01 | 3.56-30.97 | 3.54-30.92 | 3.54-30.99 | 3.54-30.96 | 3.55-30.90 |
| $\mu$ (mm$^{-1}$) | 39.918 | 39.972 | 39.242 | 39.380 | 39.320 | 39.425 |
| *Data Collection and Refinement* | | | | | | |
| Collected reflections | 710 | 699 | 2160 | 2252 | 2251 | 2598 |
| Unique reflections | 433 | 426 | 244 | 244 | 244 | 243 |
| $R_{int}$ | 0.0179 | 0.0155 | 0.0133 | 0.0128 | 0.0234 | 0.0203 |
| *h* | $-8 \le h \le 8$ | | $-10 \le h \le 10$ | | $-10 \le h \le 10$ | |
| *k* | $-16 \le k \le 16$ | | $-13 \le k \le 13$ | | $-13 \le k \le 13$ | |
| *l* | $-5 \le l \le 5$ | $-4 \le l \le 5$ | $-5 \le l \le 5$ | | $-4 \le l \le 5$ | |
| $\Delta\rho_{max}$ (e Å$^{-3}$) | 3.068 | 2.999 | 2.611 | 2.474 | 5.223 | 4.764 |
| $\Delta\rho_{min}$ (e Å$^{-3}$) | -1.862 | -1.768 | -2.607 | -2.758 | -4.680 | -3.777 |
| GoF | 1.149 | 1.294 | 1.149 | 1.159 | 1.183 | 1.159 |
| Extinction coefficient | 0.0121(10) | 0.0119(10) | 0.0166(11) | 0.0144(10) | 0.018(3) | 0.014(3) |
| [a] $R_1(F)$ for $F_o^2 > 2\sigma(F_o^2)$ | 0.0209 | 0.0237 | 0.0177 | 0.0186 | 0.0388 | 0.0424 |
| [b] $R_w(F_o^2)$ | 0.0553 | 0.0603 | 0.0459 | 0.0462 | 0.1016 | 0.1116 |

[a] $R_1 = \Sigma||F_0| - |F_c||/\Sigma|F_0|$
[b] $wR_2 = [\Sigma w(F_o^2 - F_c^2)^2/\Sigma w(F_0^2)^2]^{1/2}$; $P = (F_o^2 + 2F_c^2)/3$; $w = 1/[\sigma^2(F_o^2) + (0.0261P)^2 + 3.2341P]$, $w = 1/[\sigma^2(F_o^2) + (0.0258P)^2 + 4.5691P]$, $w = 1/[\sigma^2(F_o^2) + (0.0663P)^2]$, and $w = 1/[\sigma^2(F_o^2) + (0.0559P)^2]$ for α-$YbAl_{0.93}Fe_{0.07}B_4$ at 295K and 100 K and β-$YbAl_{0.97}Fe_{0.03}B_4$ at 295 K and 100 K, respectively

†Reproduced with permission from Kuga, K.; Morrison, G.; Treadwell, L.; Chan, J. Y.; Nakatsuji, S., *Phys. Rev. B* **2012,** *86*, 224413. Copyright 2012 American Physical Society.

## 7.2 Experimental

The synthesis of single crystals of α-$YbAl_{1-x}Fe_xB_4$ ($0 \le x \le 0.07$) and β-$YbAl_{1-x}Fe_xB_4$ ($0 \le x \le 0.06$) has previously been reported.[7.1, 8] The Fe concentration in the crystals was determined using ICP data for the α-phase and EDX data for the β-phase.[7.8] Single crystal X-ray diffraction

data were collected using a Nonius KappaCCD diffractometer equipped with a Mo $K_\alpha$ source ($\lambda$ = 0.70930 Å) at room temperature, 295(3) K, and at 100(1) K. Direct methods using SIR92[7.9] was performed in order to obtain an initial structural model which was then refined using SHELXL-97.[7.10] Crystallographic data and atomic coordinates for α-$YbAl_{1-x}Fe_xB_4$ ($x$ = 0.07) and β-$YbAl_{1-x}Fe_xB_4$ ($x$ = 0.03, 0.05) can be found in Tables 7.1-3.

**Table 7.2**† Atomic Coordinates and Atomic Displacement Parameters for α-$YbAl_{0.93}Fe_{0.07}B_4$

| Atom | Wyckoff site | $x$ | $y$ | $z$ | $U_{eq}$ (Å$^2$)[a] | Occ. |
|---|---|---|---|---|---|---|
| **295(3) K** | | | | | | |
| Yb(1) | 4*g* | 0.12859(5) | 0.15052(3) | 0 | 0.00344(17) | 1 |
| Al(1) | 4*g* | 0.1365(4) | 0.4109(2) | 0 | 0.0042(8) | 0.929(15) |
| Fe(1) | 4*g* | 0.1365(4) | 0.4109(2) | 0 | 0.0042(8) | 0.071(15) |
| B(1) | 4*h* | 0.2921(16) | 0.3135(8) | ½ | 0.0056(16) | 1 |
| B(2) | 4*h* | 0.3654(15) | 0.4695(8) | ½ | 0.0054(16) | 1 |
| B(3) | 4*h* | 0.3850(16) | 0.0479(8) | ½ | 0.0063(15) | 1 |
| B(4) | 4*h* | 0.4725(16) | 0.1939(8) | ½ | 0.0042(16) | 1 |
| **100(1) K** | | | | | | |
| Yb(1) | 4*g* | 0.12862(6) | 0.15052(3) | 0 | 0.00166(19) | 1 |
| Al(1) | 4*g* | 0.1361(4) | 0.4109(2) | 0 | 0.0023(9) | 0.935(17) |
| Fe(1) | 4*g* | 0.1361(4) | 0.4109(2) | 0 | 0.0023(9) | 0.065(17) |
| B(1) | 4*h* | 0.2915(19) | 0.3138(9) | ½ | 0.0047(18) | 1 |
| B(2) | 4*h* | 0.3651(17) | 0.4686(8) | ½ | 0.0032(17) | 1 |
| B(3) | 4*h* | 0.3875(17) | 0.0482(9) | ½ | 0.0023(16) | 1 |
| B(4) | 4*h* | 0.4751(18) | 0.1929(9) | ½ | 0.0037(18) | 1 |

[a] $U_{eq}$ is defined as one-third of the trace of the orthogonalized $U_{ij}$ tensor.

## 7.3 Results and Discussion

### 7.3.1 α-$YbAl_{1-x}Fe_xB_4$

Table 7.2 shows the atomic coordinates for α-$YbAl_{0.93}Fe_{0.07}B_4$. When the Fe substitution was not accounted for, the Al site (4*g*) had an anomalously small atomic displacement parameter as compared to the undoped α-$YbAlB_4$. Therefore, the Fe was partially substituted on the Al site and the occupancies of the two elements were freely refined. This resulted in a mixed occupancy of 7.1(15)% Fe and 92.9(15)% Al at 295(3) K and is in good agreement with the composition as obtained from the elemental analysis using the ICP method. Furthermore, no evidence for a structural transition was observed with substitution, and likewise, no structural transition was observed for any Fe concentration upon cooling from room temperature down to 100(1) K.[7.8]

Figure 7.1 shows the effect that the Fe dopant concentration has on the lattice parameters and volume of α-$YbAl_{1-x}Fe_xB_4$. For both temperatures studied, the *a* and *b* lattice parameters show an initial increase upon doping from $YbAlB_4$ to $YbAl_{1-x}Fe_xB_4$ (x = 0.005) after which, a steady decrease occurs with increased Fe concentration. The *c* lattice parameter does not show this initial increase, only steadily decreasing with increased Fe concentration at both temperatures. The *c* lattice parameter was found to have a much greater dependence on the dopant concentration than the *a* and *b* lattice parameters. Substitution of the smaller Fe onto the Al site allows for the boron layers to collapse towards each other leading to the decrease in the *c* direction. On the other hand, while doping Fe onto the Al site affects the YbAl layers, it has little effect on the boron layer, consistent with the greater change in the *c* lattice parameter than the *a* and *b* lattice parameters. Overall, the volume shows a continuous decrease with increasing Fe doping. Compared to the undoped analogue, α-$YbAl_{0.93}Fe_{0.07}B_4$ shows a volume contraction of ~0.8%. This indicates that Fe doping applies chemical pressure to the system.

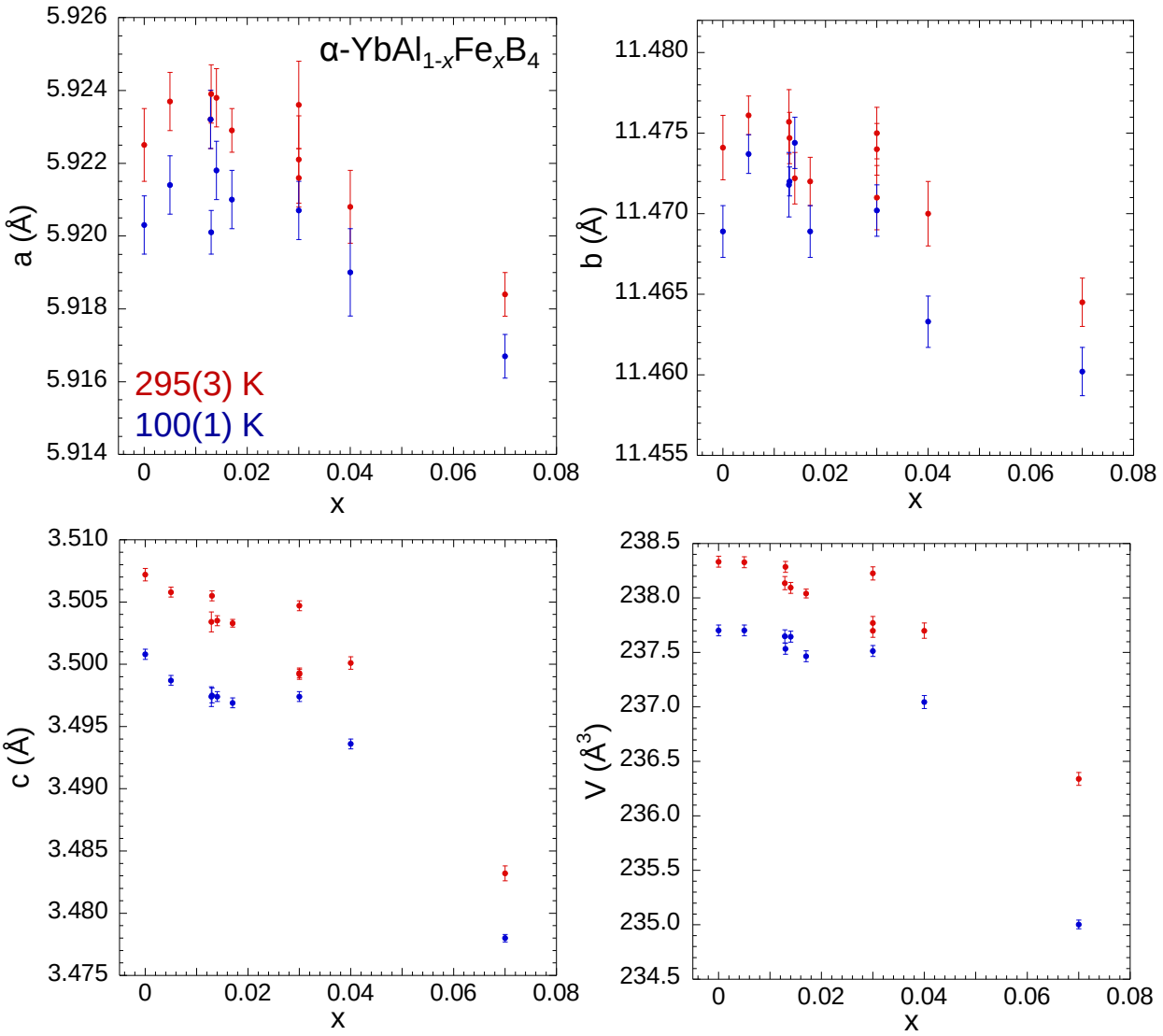


**Figure 7.1** The effect of Fe dopant concentration on the lattice parameters and volume of α-$YbAl_{1-x}Fe_xB_4$.

### 7.3.2 β-$YbAl_{1-x}Fe_xB_4$

Tables 7.3 and 7.4 provide atomic coordinates for β-$YbAl_{1-x}Fe_xB_4$ (x = 0.03, 0.05). When the Fe substitution was not included in the model, the Al site (4*g*) had a similar atomic displacement parameter to the Yb site (4*i*) suggesting that the Fe occupies the Al site. For β-$YbAl_{0.97}Fe_{0.03}B_4$, Fe was partially substituted onto the Al site and the occupancies were freely refined. The resulting site occupancy was 1.3(15)% Fe and 98.7(15)% Al at 295(3) K. This is in

**Table 7.3**[†] Atomic Coordinates and Atomic Displacement Parameters for β-$YbAl_{0.97}Fe_{0.03}B_4$

| Atom | Wyckoff site | *x* | *y* | *z* | $U_{eq}$ (Å$^2$)[a] | Occ. |
|---|---|---|---|---|---|---|
| **295(3) K** | | | | | | |
| Yb(1) | 4*i* | 0 | 0.30065(4) | 0 | 0.00388(19) | 1 |
| Al(1) | 4*g* | 0.1808(3) | 0 | 0 | 0.0042(8) | 0.987(15) |
| Fe(1) | 4*g* | 0.1808(3) | 0 | 0 | 0.0042(8) | 0.013(15) |
| B(1) | 4*h* | 0.1219(13) | ½ | ½ | 0.0050(13) | 1 |
| B(2) | 8*q* | 0.2226(8) | 0.1594(14) | ½ | 0.0061(10) | 1 |
| B(3) | 4*j* | 0 | 0.0922(9) | ½ | 0.0044(13) | 1 |
| **100(1) K** | | | | | | |
| Yb(1) | 4*i* | 0 | 0.30066(3) | 0 | 0.00260(19) | 1 |
| Al(1) | 4*g* | 0.1810(3) | 0 | 0 | 0.0031(8) | 0.996(15) |
| Fe(1) | 4*g* | 0.1810(3) | 0 | 0 | 0.0031(8) | 0.004(15) |
| B(1) | 4*h* | 0.1215(13) | ½ | ½ | 0.0046(14) | 1 |
| B(2) | 8*q* | 0.2224(8) | 0.1596(8) | ½ | 0.0046(10) | 1 |
| B(3) | 4*j* | 0 | 0.0921(9) | ½ | 0.0043(14) | 1 |

[a] $U_{eq}$ is defined as one-third of the trace of the orthogonalized $U_{ij}$ tensor.

[†]Reproduced with permission from Kuga, K.; Morrison, G.; Treadwell, L.; Chan, J. Y.; Nakatsuji, S., *Phys. Rev. B* **2012,** *86*, 224413. Copyright 2012 American Physical Society.

agreement with the ICP data which indicated the stoichiometry to be β-$YbAl_{0.98}Fe_{0.02}B_4$. While the atomic displacement parameters also suggested that the Fe occupied the Al site in β-$YbAl_{0.95}Fe_{0.05}B_4$, no Fe could be refined onto this site, or any other site, for the model. The inability to model the Fe doping in β-$YbAl_{0.95}Fe_{0.05}B_4$ can be attributed to the lower quality diffraction data for this analogue compared to the other analogues. β-$YbAl_{0.95}Fe_{0.05}B_4$ grew as thin plates whereas β-$YbAl_{0.97}Fe_{0.03}B_4$ grew as thick plates and α-$YbAl_{0.93}Fe_{0.07}B_4$ grew as rods. The thinner plates for β-$YbAl_{0.95}Fe_{0.05}B_4$ led to lower quality X-ray diffraction data which is apparent in both the increased $R_1$ and residual electron densities for this analogue. Due to the increased $\Delta\rho_{min/max}$, the Fe substitution could not be modeled. As with α-$YbAl_{1-x}Fe_xB_4$, no

**Table 7.4**[†] Atomic Coordinates and Atomic Displacement Parameters for β-$YbAl_{0.95}Fe_{0.05}B_4$

| Atom | Wyckoff site | *x* | *y* | *z* | $U_{eq}$ (Å$^2$)[a] | Occ. |
|---|---|---|---|---|---|---|
| **295(3) K** | | | | | | |
| Yb(1) | 4*i* | 0 | 0.30070(4) | 0 | 0.0054(4) | 1 |
| Al(1) | 4*g* | 0.1799(6) | 0 | 0 | 0.0049(8) | 1 |
| B(1) | 4*h* | 0.122(3) | ½ | ½ | 0.005(2) | 1 |
| B(2) | 8*q* | 0.2225(8) | 0.1607(15) | ½ | 0.0067(17) | 1 |
| B(3) | 4*j* | 0 | 0.0917(15) | ½ | 0.006(2) | 1 |
| **100(1) K** | | | | | | |
| Yb(1) | 4*i* | 0 | 0.30072(5) | 0 | 0.0042(4) | 1 |
| Al(1) | 4*g* | 0.1802(6) | 0 | 0 | 0.0031(8) | 1 |
| B(1) | 4*h* | 0.124(3) | ½ | ½ | 0.009(3) | 1 |
| B(2) | 8*q* | 0.2227(15) | 0.1598(18) | ½ | 0.009(2) | 1 |
| B(3) | 4*j* | 0 | 0.0913(12) | ½ | 0.004(3) | 1 |

[a] $U_{eq}$ is defined as one-third of the trace of the orthogonalized $U_{ij}$ tensor.

[†]Reproduced with permission from Kuga, K.; Morrison, G.; Treadwell, L.; Chan, J. Y.; Nakatsuji, S., *Phys. Rev. B* **2012,** *86*, 224413. Copyright 2012 American Physical Society.

structural transition was observed in β-$YbAl_{1-x}Fe_xB_4$ upon doping or cooling down to 100 K.[7,8]

Single crystal X-ray diffraction data was also collected on a sample of β-$YbAl_{0.94}Fe_{0.06}B_4$. Although the mosaicity of the single crystal was suitable for data collection at 295(3) K, upon cooling in 50 K intervals down to 100(1) K, a continuous decrease in crystal quality, indicated by increased $\chi^2$s and mosaicity, was observed. For example, the mosaicity of the crystal increased from 0.45 degrees at 295(3) K to 0.87 degrees at 100(1) K. When the crystal was warmed back to room temperature, the crystal quality returned to its original state. Diffraction data of β-$YbAl_{0.94}Fe_xB_4$ was collected at both 295(3) K and 100(1) K and no evidence for a structural transition was observed. In α-$YbAl_{0.93}Fe_{0.07}B_4$ and β-$YbAl_{1-x}Fe_xB_4$ ($x$ = 0.03, 0.05), on the other hand, the degradation of crystal quality on cooling was not observed. Synthesis experiments

suggest that the concentration $x = 0.06$ is close to the edge of the stability of the Fe doped β-phase, and this may be the origin of the increase in the mosaicity on cooling.

Figure 2 shows the effect that the Fe dopant concentration has on the lattice parameters and volume of β-$YbAl_{1-x}Fe_xB_4$. The *a* and *c* lattice parameters decrease with increased Fe concentration while the *b* direction increases slightly. Like with α-$YbAl_{1-x}Fe_xB_4$, the change in

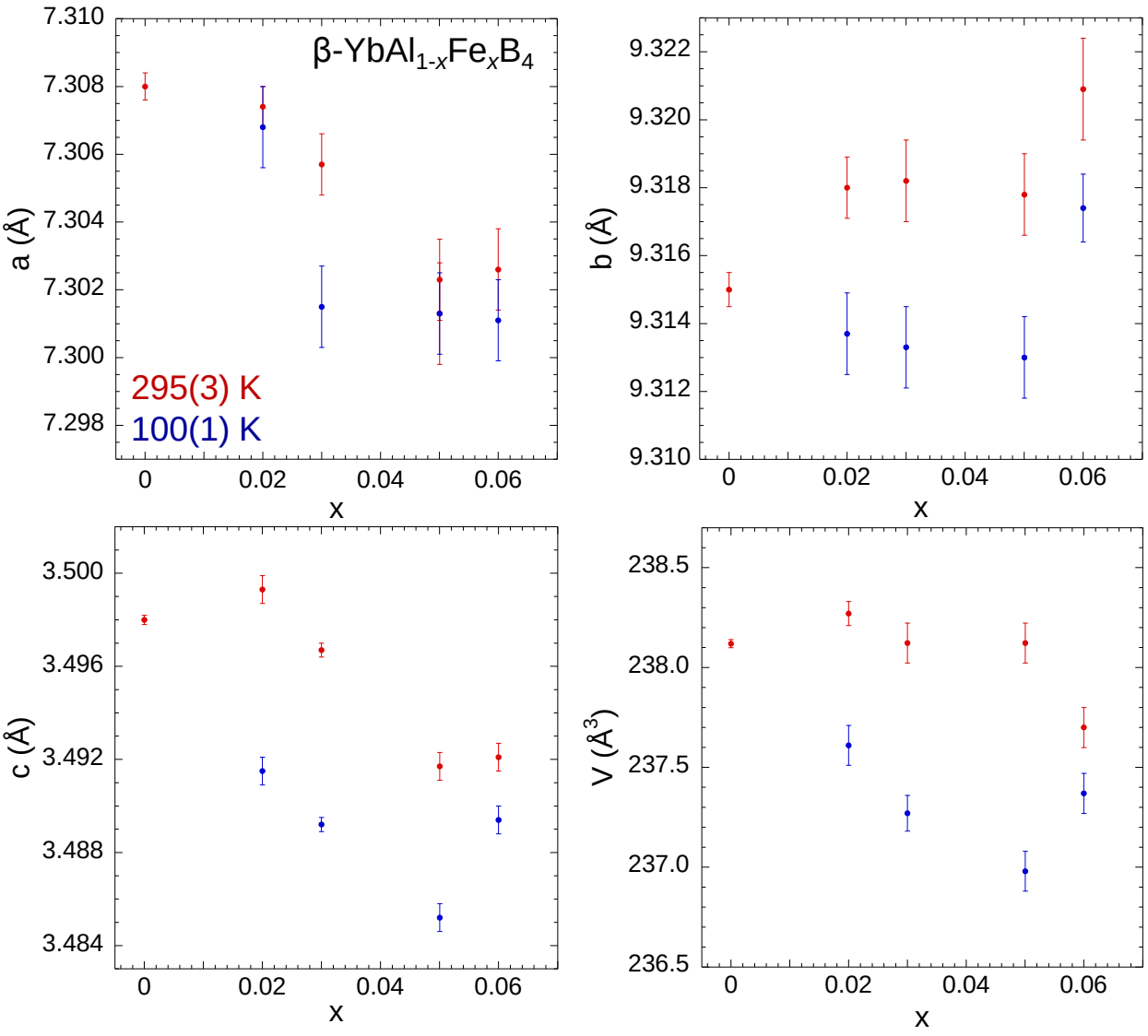


**Figure 7.2** The effect of Fe dopant concentration on the lattice parameters and volume of β-$YbAl_{1-x}Fe_xB_4$.

the *c*-direction is more pronounced than in the other two directions, consistent with the structure. Overall, the volume of the unit cell decreases with increasing Fe concentration, indicating that the Fe doping applies chemical pressure to the system. At $x = 0.05$, the volume has contracted 0.2% compared to the undoped analogue.

## 7.4 Conclusion

Single crystal X-ray diffraction data were collected on crystals of α-$YbAl_{1-x}Fe_xB_4$ ($0 \leq x \leq 0.07$) and β-$YbAl_{1-x}Fe_xB_4$ ($0 \leq x \leq 0.06$). The Fe was found to dope onto the Al site in both polymorphs. No structural transition was observed upon doping Fe into the systems or upon cooling from 295 K to 100 K in any analogue. However, in both analogues, a continuous decrease in unit cell volume was observed with increasing Fe concentration and was most pronounced in the *c* direction. This indicates that Fe doping applies chemical pressure to the systems. In this way, a thorough understanding of the structural effects of Fe doping helps explain the properties of the two polymorphs of $YbAl_{1-x}Fe_xB_4$ and to shed light on the normal state of the quantum critical β-$YbAl_{1-x}Fe_xB_4$.[7.8]

## 7.5 References


7.1. Macaluso, R. T.; Nakatsuji, S.; Kuga, K.; Thomas, E. L.; Machida, Y.; Maeno, Y.; Fisk, Z.; Chan, J. Y., *Chem. Mater.* **2007,** *19*, 1918-1922.

7.2. Okawa, M.; Matsunami, M.; Ishizaka, K.; Eguchi, R.; Taguchi, M.; Chainani, A.; Takata, Y.; Yabashi, M.; Tamasaku, K.; Nishino, Y.; Ishikawa, T.; Kuga, K.; Horie, N.; Nakatsuji, S.; Shin, S., *Phys. Rev. Lett.* **2010,** *104*, 247201.

7.3. Matsumoto, Y.; Kuga, K.; Horie, N.; Nakatsuji, S., *J. Phys. Conf. Ser.* **2011,** *273*, 012006.

7.4. Matsumoto, Y.; Nakatsuji, S.; Kuga, K.; Karaki, Y.; Horie, N.; Shimura, Y.; Sakakibara, T.; Nevidomskyy, A. H.; Coleman, P., *Science* **2011,** *331*, 316-319.

7.5. Gegenwart, P.; Custers, J.; Geibel, C.; Neumaier, K.; Tayama, T.; Tenya, K.; Trovarelli, O.; Steglich, F., *Phys. Rev. Lett.* **2002,** *89*, 056402.

7.6. Jiang, S.; Xing, H.; Xuan, G.; Wang, C.; Ren, Z.; Feng, C.; Dai, J.; Xu, Z. a.; Cao, G., *J. Phys. Condens. Matter* **2009,** *21*, 382203.

7.7. Park, K.; Wu, L. S.; Janssen, Y.; Kim, M. S.; Marques, C.; Aronson, M. C., *Phys. Rev. B* **2011,** *84*, 094425.

7.8. Kuga, K.; Morrison, G.; Treadwell, L.; Chan, J. Y.; Nakatsuji, S., *Phys. Rev. B* **2012,** *86*, 224413.

7.9. Altomare, A.; Burla, M. C.; Camalli, M.; Cascarano, G.; Giacovazzo, C.; Guagliardi, A.; Polidori, G., *J. Appl. Crystallogr.* **1994,** *27*, 435.

7.10. Sheldrick, G. M., *Acta Crystallogr. Sect. A* **2008,** *64*, 112-122.

# Chapter 8. Synthesis, Characterization, and Surface Patterning of $FeNi_3$ and $Ln_2O_3$ Nanoparticles

## 8.1 Nanointermetallic $FeNi_3$

Magnetic sample modulation, MSM, is an enhanced atomic force microscopy, AFM, technique which can provide magnetic information about individual nanoparticles. In MSM, an alternating current electromagnetic field is applied beneath the AFM sample stage. The magnetic field causes magnetic nanoparticles to oscillate which can be detected by a non-magnetic tip in contact mode. Using MSM, surface topography and magnetic mapping can be concurrently obtained.[8.1]

To further explore the capabilities of MSM, A. Kelley *et al.* synthesized $FeNi_3$ nanoparticles.[8.2] The samples used in these studies consisted of $FeNi_3$ and $Fe_3O_4$ nanoparticles. While this allowed for the investigation of whether MSM can distinguish between two types of nanoparticles,[8.2] for further studies of MSM, phase pure $FeNi_3$ nanoparticles are desired.

$FeNi_3$ crystallizes in the face-centered cubic structure ($AuCu_3$ type) with cubic space group *Pm*3*m* and lattice parameter $a$ = 3.525 Å.[8.3] $FeNi_3$ can either crystallize as an intermetallic with Ni on the corners of the unit cell and Fe in the face centers, or as an alloy with a mix on each site. Typically, the intermetallic forms in low temperature growth conditions, under 500 °C, such as those used in most nanoparticle syntheses.[8.3] However, it can be difficult to distinguish between the two forms.[8.4] $FeNi_3$ is a room temperature ferromagnet and for this reason, $FeNi_3$ nanoparticles are of interest for purposes such as magnetic memory, sensors, and biomedical applications.[8.5-7]

### 8.1.1 Synthesis

The co-reduction method[8.8] was used for the synthesis of $FeNi_3$. In all reactions, 2.64 x $10^{-4}$ moles of an Fe source and three times that of $Ni(NO_3)_2 \cdot 6H_2O$ were added to water along with

a reducing agent. Heating of the reaction was carried out either in a Parr Bomb which was heated to 180 °C for 15 h or in microwave vessel which was heated to 180 °C for 1 h.

Initially, two reactions were carried out using the previously reported procedure.[8.2] These reactions used $Fe(NO_3)_3 \cdot 9H_2O$ as the Fe source and hydrazine, $N_2H_4 \cdot H_2O$, as the reducing agent. For hydrazine to act as a reducing agent, a basic environment is required and was obtained by the addition of NaOH to the reaction. Both reactions were degassed by bubbling with nitrogen before heating. The first reaction was heated in a Parr Bomb and resulted in a mixture of $FeNi_3$ and magnetite, $Fe_3O_4$. The second reaction, was heated in the microwave and did not yield the desired product, $FeNi_3$. Instead, only $Ni(OH)_2$ and an unknown product formed. This can be explained by Reaction 8.1. Hydrazine can undergo two competing reactions. The desired reaction, the reduction of a metal center, produces one equivalent of nitrogen gas. The second reaction, which is more energetically favorable at standard conditions, is the decomposition of hydrazine into one equivalent of nitrogen gas and four equivalents of ammonia gas. Therefore, in order to carry out the desired reduction, hydrazine requires high pressure. This was achieved in the Parr Bomb which was about 75 % full but was not achieved in the microwave vessel, which was approximately 25 % full.

**Reaction 8.1** Standard reaction potentials for pertinent hydrazine reactions.[8.5]

$$2Fe^{2+} + 4OH^- + N_2H_4 \rightarrow 2Fe + N_2 + 4H_2O \quad E_0 = 0.44 \text{ V}$$
$$2Ni^{2+} + 4OH^- + N_2H_4 \rightarrow 2Ni + N_2 + 4H_2O \quad E_0 = 0.49 \text{ V}$$

$$3N_2H_4 \rightarrow N_2 + 4NH_3 \quad E_0 = 1.05 \text{ V}$$

In an attempt to purify the synthesis of $FeNi_3$, several further reactions were carried out. As shown in Reaction 8.2, for magnetite to form, $Fe^{+2}$, $Fe^{+3}$ and a basic environment are required. Initially, it was attempted to remove the basic environment by using a reducing agent that did not require hydroxide ions. For this reason, a reaction using potassium oxalate was attempted. This

reaction was split in half and one half was heated in a Parr Bomb and the other half in a microwave. These reactions did not yield any $FeNi_3$ but instead only yielded Ni(II) oxalate. This suggests that the oxalate ion preferred to be a ligand instead of a reducing agent. Instead of removing the basic environment, it then became of interest to remove one of the iron cations. As an Fe(III) source was being used, some of the Fe(III) must have been reduced to Fe(II) during the reaction process.

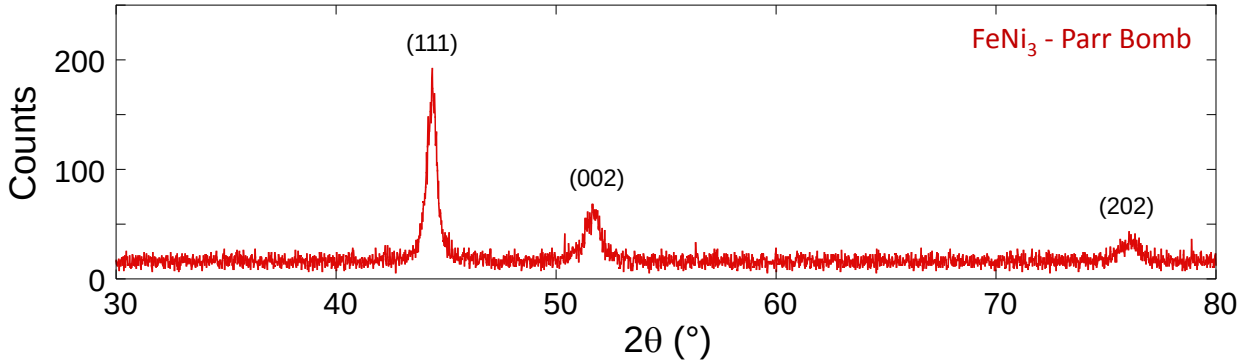


**Figure 8.1** Powder diffraction pattern of $FeNi_3$ nanoparticles heated in a Parr Bomb

To avoid the presence of both cations, an Fe(II) source, $FeCl_2$, was used. This reaction was degassed before heating in a Parr Bomb and resulted in a mixture of $FeNi_3$ and $Fe_3O_4$. In order for magnetite to form, an oxidizing agent must have been present to oxidize some of the Fe(II). As this oxidizing agent was believed to be oxygen, another reaction was carried out using a glovebox to prepare the reaction. This reaction was heated in a Parr Bomb and the powder XRD, shown in Figure 8.1, indicated that only $FeNi_3$ was produced.

**Reaction 8.2** Formation of magnetite.[8.9]

$$Fe^{2+} + 2Fe^{3+} + 8OH^- \rightarrow Fe_3O_4 + 4H_2O$$

After the successful synthesis of $FeNi_3$ using a Parr Bomb, it was of interest to produce it using a microwave. In order to increase the pressure within the microwave vessel and thereby favor the reduction of the metal centers over the decomposition of hydrazine, an excess of hydrazine was added to the reaction. In this way, some hydrazine would initially decompose,

increasing the pressure enough to allow for the remaining hydrazine to act as a reducing agent. As shown in Figure 8.2, this reaction yielded phase pure $FeNi_3$.

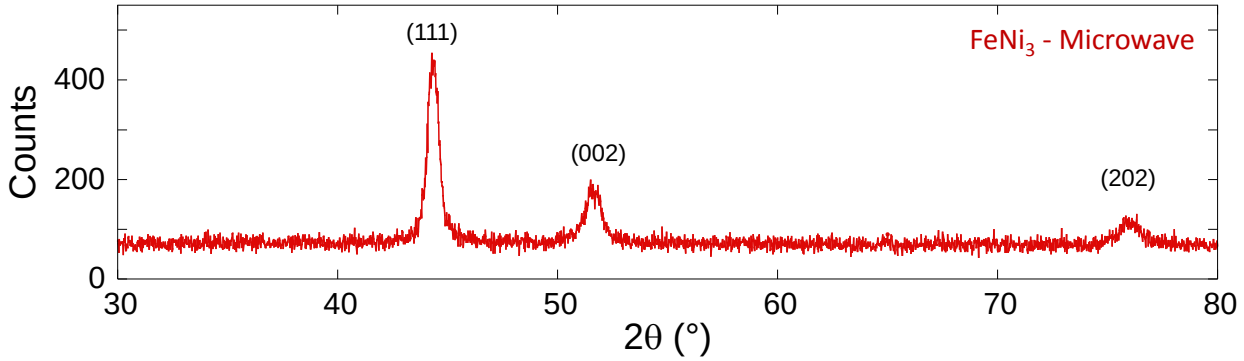


**Figure 8.2** Powder diffraction pattern of $FeNi_3$ nanoparticles produced using microwave heating

## 8.2 Spatially Separated $Y_2O_3$ Arrays

Due to the two valence states available to cerium, $CeO_2$ has the ability to release oxygen. This ability makes cerium oxide a useful oxidative catalyst for a variety of applications such as three-way automotive catalysts,[8.10, 11] gas sensors,[8.12] fine chemical synthesis,[8.13-15] and solid oxide fuel cells.[8.16] For many of these applications, the ceria catalysts is coupled with a noble metal, such as Pt or Pd.[8.17] These catalytic properties can be enhanced by using ceria nanoparticles.[8.16]

Two processes occur which decrease the efficiency of nanoparticles for catalysis: agglomeration and Ostwald ripening. Agglomeration is the adhesion of particles which are in contact with each other while Ostwald ripening is the dissolution of smaller particles in order to provide monomer for the growth of larger particles. Both of these processes lead to larger particle sizes and smaller surface areas thereby reducing particle efficiency.[8.18, 19]

In order to prevent agglomeration and to limit Ostwald ripening, we have proposed to produce ordered arrays of spatially separated ceria nanoparticles using nanolithography techniques. Due to the difficulty of ceria synthesis compared to other lanthanide oxides, namely the need for hydrofluoric acid, we have selected $Y_2O_3$ to evaluate synthetic variables.

### 8.2.1 Synthesis

Yttrium trichloroacetate was prepared according to a previously published procedure.[8.20] Yttria powder (15 mmol) was dissolved in concentrated nitric acid (100 mL) heated to 80 °C. The dissolved $Y_2O_3$ solution was cooled to room temperature, and yttrium hydroxide was precipitated from the solution by adding $NH_4OH$ until the solution registered as basic. The precipitate was separated via vacuum filtration and washed several times with deionized water. A solution of yttrium trichloroacetate was prepared by dissolving the hydroxide precipitate in a 25% trichloroacetic acid solution.

Microchannels of $Y_2O_3$ were patterned on a UV-ozone cleaned silicon wafer. A PDMS mold of 3 μm triangular channels was placed on the clean silicon wafer. A drop of the yttrium trichloroacetate solution was placed next to the PDMS mold. Capillary action at the opening of the stamp draws liquid into the microchannels. The solution was dried overnight and the stamp was removed leaving behind patterned yttrium trichloroacetate. The sample was heated to 150 °C for 3 h in order to decompose the acid and form $Y_2(CO_3)_3$. The carbonate was further decomposed to $Y_2O_3$ by heating to 800 °C overnight.

Nanoparticles of $Y_2O_3$ were patterned in hexagonal close packed arrays of pores in an octadecyltrichlorosilane (OTS) surface assembled monolayer (SAM) on silicon made using two particle lithography. Yttrium trichloroacetate solution was filled into the pores using discontinuous dewetting, a process in which a polar solution selectively adheres to a hydrophilic pore over a hydrophobic SAM by removing the sample from the solution on an angle. After the pores are filled, the sample was air dried and then heated using the same profile as for the microchannels. The 800 °C dwell temperature was sufficient to both decompose the carbonate and to burn off the OTS monolayer, leaving only the yttria nanoparticles on the quartz surface.

## 8.3 References


8.1. Daniels, S. L.; Ngunjiri, J. N.; Garno, J. C., *Anal. Bioanal. Chem.* **2009,** *394*, 215-223.

8.2. Kelly, A. T.; Daniels, S. L.; Englade, L. E.; Morrison, G.; Serem, W. K.; Flurry, N.; Chan, J. Y.; Garno, J. C., *In Preparation* **2013**.

8.3. Lu, X.; Liang, G.; Zhang, Y., *Mater. Sci. Eng., B* **2007,** *139*, 124-127.

8.4. Drijver, J. W.; van der Woude, F.; Radelaar, S., *Phys. Rev. B* **1977,** *16*, 985-992.

8.5. Liao, Q.; Tannenbaum, R.; Wang, Z. L., *J. Phys. Chem. B* **2006,** *110*, 14262-14265.

8.6. Zhou, X.-M.; Wei, X.-W., *Cryst. Growth Des.* **2008,** *9*, 7-12.

8.7. Jia, J.; Yu, J. C.; Wang, Y.-X. J.; Chan, K. M., *ACS Appl. Mater. Interfaces* **2010,** *2*, 2579-2584.

8.8. Ferrando, R.; Jellinek, J.; Johnston, R. L., *Chem. Rev.* **2008,** *108*, 845-910.

8.9. Kim, D. K.; Mikhaylova, M.; Zhang, Y.; Muhammed, M., *Chem. Mater.* **2003,** *15*, 1617-1627.

8.10. Kumar, P. A.; Tanwar, M. D.; Bensaid, S.; Russo, N.; Fino, D., *Chem. Eng. J.* **2012,** *207*, 258-266.

8.11. Kaspar, J.; Fornasiero, P.; Graziani, M., *Catal. Today* **1999,** *50*, 285-298.

8.12. Izu, N.; Shin, W.; Murayama, N.; Kanzaki, S., *Sens. Actuators, B* **2002,** *87*, 95-98.

8.13. Sutradhar, N.; Sinhamahapatra, A.; Pahari, S.; Jayachandran, M.; Subramanian, B.; Bajaj, H. C.; Panda, A. B., *J. Phys. Chem. C* **2011,** *115*, 7628-7637.

8.14. Jacobs, G.; Chenu, E.; Patterson, P. M.; Williams, L.; Sparks, D.; Thomas, G.; Davis, B. H., *Appl. Catal., A* **2004,** *258*, 203-214.

8.15. Trovarelli, A.; de Leitenburg, C.; Boaro, M.; Dolcetti, G., *Catal. Today* **1999,** *50*, 353-367.

8.16. Feng, X.; Shi, Y.; Zhou, H., *J. Rare Earths* **2012,** *30*, 29-33.

8.17. Vilé, G.; Bridier, B.; Wichert, J.; Pérez-Ramírez, J., *Angew. Chem. Int. Ed.* **2012,** *51*, 8620-8623.

8.18. Ouyang, R.; Liu, J.-X.; Li, W.-X., *J. Am. Chem. Soc.* **2012,** *135*, 1760-1771.

8.19. Li, D.; Kaner, R. B., *J. Am. Chem. Soc.* **2005,** *128*, 968-975.

8.20. Dragoo, A. L.; Domingues, L. P., *J. Am. Ceram. Soc.* **1982,** *65*, 253-259.

## Chapter 9. Conclusions

The research in this document focused on three structurally related sets of compounds: $Ln Ru_2Al_{10}$, $CeRu_4(Al,Si)_{15.58}$ and $Ln_2Ru_3Al_{15}$. These studies were initially motivated by the anomalous properties observed in $CeRu_2Al_{10}$, namely the higher ordering temperature than expected from de Gennes scaling[9.1] and the metal to insulator transition near this ordering temperature.[9.2]

$PrRu_2Al_{10}$ enters a non-magnetic ground state at 13.2 K due to crystalline electric field effects, $GdRu_2Al_{10}$ orders antiferromagnetically at 15.5 K, and $YbRu_2Al_{10}$ is a Pauli paramagnetic. All three analogues display metallic resistivity for all T with the Yb analogue exhibiting a $T^3$ dependence at low temperatures, believed to be the result of scattering due to *s*-*d* transitions. $CeRu_4(Al,Si)_{15.58}$ follows Curie-Weiss behavior with $\theta$ = -21.9(14) K but does not order down to 3 K, and the resistivity displays a negative temperature coefficient. Finally $Ce_2Ru_3Al_{15.08}$ and $Gd_2Ru_{3.08}Al_{15}$ order antiferromagnetically at 3.7 K and 21.0 K, respectively.

Despite the similar *Ln* environments, none of the compounds studied displayed similar behavior to those of $CeRu_2Al_{10}$. It has been suggested from computational studies that the Ce polyhedra play a large role in the properties of $CeRu_2Al_{10}$.[9.3] For this reason, structurally related $Ce_2Ru_3Al_{15}$ can serve as a good comparison structure for further studies of $CeRu_2Al_{10}$.

While the initial goal of this research was to look for properties resembling those of $CeRu_2Al_{10}$, these studies also highlighted the difficulties and benefits of single crystal flux growth and the large effect that crystalline electric fields can have on compounds. $Ln Ru_2Al_{10}$ compounds are very robust and easily grow from melts with a variety of compositions dwelled at a broad range of temperatures. As a result, growing other compounds in the Al rich portion of the *Ln*-Ru-Al phase space can be challenging. Similarly, the growth of $CeRu_4(Al,Si)_{15.58}$ was made difficult due

to the high stability of $Ru_{23}(Al,Si)_{97}$. The growth of $Ln_2Ru_3Al_{15}$ was found to be favored over the growth of $LnRu_2Al_{10}$ at high temperatures and in Ru poor conditions. The prior allowed for the growth of polycrystalline $Ln_2Ru_3Al_{15}$ (*Ln* = Ce, Gd) via arc melting while the latter allowed for the flux growth of large single crystals of $Ln_2Ru_3Al_{15}$ (*Ln* = Y, Gd, Tb).

Single crystalline $Gd_2Ru_3Al_{15.09}$ and polycrystalline $Gd_2Ru_{3.08}Al_{15}$ demonstrate the advantages of single crystals for materials characterization. The availability of high quality single crystals allowed for the measurement of the intrinsic magnetization and magnetoresistance unaffected by grain boundaries and impurities. Furthermore, the ability to measure anisotropic properties provided insight into the arrangement of moments in the antiferromagnetic ordering. Finally, the structure of $Gd_2Ru_3Al_{15}$ was found to be synthesis method dependent, with the resulting change in Gd-Gd contact lengths leading to different Neel temperatures in the polycrystalline and single crystalline analogues.

One of the advantages of studying multiple structurally related compounds within a phase space is that it allows for the study of structure-property relationships. For example, in both the $GdM_2Al_{10}$ (M = Fe, Ru, Os) and the $Gd_2Ru_3Al_{15}$ analogues, it was found that increased Gd-Gd interactions led to lower ordering temperatures. This suggests that the cosine dependence of the RKKY interaction is on an upturn at these distances leading to increased interaction strengths with increased distance.

A second structure-property relationship can be drawn between the *Ln* polyhedra and crystalline electric field effects. As CEF effects are important to the properties of $CeRu_2Al_{10}$, it was expected that CEF effects would be observed in the structurally related compounds. Indeed, crystalline electric field splitting led to a non-magnetic ground state in $PrRu_2Al_{10}$ and were observed below 100 K in $Ce_2Ru_3Al_{15.04}$. Anisotropic magnetization can be a powerful tool for

studying CEF effects. The ability to grow large single crystals of $Ln_2Ru_3Al_{15}$ for latter rare earths combined with the CEF effects observed in the structurally related compounds made it of interest to further study CEF effects in $Ln_2Ru_3Al_{15}$. As the *f*-electrons in $Gd^{3+}$ are spherically symmetric and therefore not susceptible to CEF effects, these studies were carried out on single crystals of $Tb_2Ru_3Al_{15.05}$. The highly anisotropic properties observed in $Tb_2Ru_3Al_{15.05}$, show the strong CEF effects that the 20 coordinate polyhedra found in $LnRu_2Al_{10}$, $CeRu_4(Al,Si)_{15.58}$ and $Ln_2Ru_3Al_{15}$ have on the *f*-electrons.

Along with the study of structure-property relationships within the *Ln*-Ru-Al phase space, this work also provides insights into methods to grow competing phases. It is not uncommon for a system to contain a highly stable binary. However, these are often easily avoided in flux-growths with the aid of binary phase diagrams by spinning the reaction above their formation temperature or using more flux rich conditions. Avoiding stable ternaries can be more challenging, as ternary phase diagrams are typically less studied or non-existent, and the undesired ternary often prefer more flux rich melts than their competing phases. This was the case with both $Ru_{23}(Al,Si)_{97}$ and $CeRu_2Al_{10}$.

The two methods that can often easily favor the desired ternary over the competing ternary, using high temperature conditions, such as in arc melting, and flux poor reactions, typically result in polycrystalline products. Throughout the course of this dissertation, several strategies have been devised for growing single crystals of competing phases which may be applied to other systems.

First, flux rich conditions can sometimes be used by sufficiently decreasing the concentration of another reactant. For $Ln_2Ru_3Al_{15}$, it was found that flux rich growths favored the formation of the undesired $LnRu_2Al_{10}$. Relatedly, *Ln* rich conditions help stabilize $Ln_2Ru_3Al_{15}$ but lead to the melt freezing at too high a temperature to facilitate single crystal growth. Reactions

which were both *Ln* and flux rich were achieved by using a Ru poor melt. In this was, large single crystals of $Ln_2Ru_3Al_{15}$ were grown while avoiding the growth of $LnRu_2Al_{10}$.

Second, the synthesis of different *Ln* analogues should be considered. While a phase may form for all *Ln*, the growth of single crystals may be easier for some rare earth analogues than others. This may be the case when a competing binary or ternary only grows for certain *Ln*. For example, the synthesis of $Ce_2Ru_3Al_{15.04}$ was more challenging than that of $Gd_2Ru_3Al_{15.09}$ because the stable $Ln_3Al_{11}$ binary only forms for *Ln* = La - Sm. This is also the case when one analogue is near the edge of stability. The mixed valence of $Ce_2Ru_3Al_{15.04}$ suggests that the $Ln_2Ru_3Al_{15}$ structure is more stable for smaller rare earths. Indeed, the latter rare earth analogues were found to more readily grow as single crystals.

Finally, special consideration should be given to the temperature profile used. Often, reactions are heated to an arbitrarily high temperature, such as 1150 °C, to achieve homogeneity before slow cooling. As was shown with $Ln_2Ru_3Al_{15}$, changing dwell temperatures can have a large effect on the resulting products. When dealing with competing phases, a temperature profile similar to that used for the growth of $Gd_2Ru_3Al_{15}$, with a slow cool at high temperatures and a faster cool at lower temperatures, is likely ideal for growing thermodynamically stable ternaries, i.e. phases that can be grown via arc melting.

Ultimately, the single crystal growth of competing phases requires careful study of the stability of the phases. Only through the systematic study of the competition between the phases by varying the temperature profile and reaction ratio can single crystals of the less robust phase be grown. While the growth of single crystals can be challenging and time consuming, the power of single crystals for physical properties studies makes such research rewarding.

## 9.2 References


9.1. Nishioka, T.; Kawamura, Y.; Takesaka, T.; Kobayashi, R.; Kato, H.; Matsumura, M.; Kodama, K.; Matsubayashi, K.; Uwatoko, Y., *J. Phys. Soc. Jpn.* **2009,** *78*, 123705.

9.2. Strydom, A. M., *Physica B* **2009,** *404*, 2981-2984.

9.3. Goraus, J.; Ślebarski, A., *J. Phys. Condens. Matter* **2012,** *24*, 095503.

# Appendix. Consent Policies

## A.1 Taylor and Francis (Blanket Approval for Chapters 1 and 3)

Our Ref: KP/TPHM/P8398

1st May 2013

Dear Gregory Morrison,

Thank you for your correspondence requesting permission to reproduce the following material from our Journal in your thesis.

**'Serendipitous growth of single crystals with silicon incorporation' by Gregory W. Morrison, Melissa C. Menard, LaRico J. Treadwell, Neel Haldolaarachchige, Kristin C. Kendrick, David P. Young & Julia Y. Chan from Philosophical Magazine, Volume 92, Issue 19-21 (2012) Special Issue: Symposium on Design, Discovery and Growth of Novel Materials: pp. 2524-2540.**

We will be pleased to grant entirely free permission on the condition that you acknowledge the original source of publication and insert a reference to the Journal's web site:
http://www.tandfonline.com/doi/full/10.1080/14786435.2012.669063

Thank you for your interest in our Journal.

Yours sincerely

**Kim Price** – Permissions Assistant, Journals.
Routledge, Taylor & Francis Group.
4 Park Square, Milton Park, Abingdon, Oxon, OX14 4RN, UK.
Web: www.tandfonline.com
e-mail: KimPaul.Price@informa.com

## A.2 American Chemical Society (Blanket Approval for Chapters 1 and 4)

### American Chemical Society's Policy on Theses and Dissertations

**If your university requires you to obtain permission, you must use the RightsLink permission system.**
**See RightsLink instructions at http://pubs.acs.org/page/copyright/permissions.html.**

This is regarding request for permission to include **your** paper(s) or portions of text from **your** paper(s) in your thesis. Permission is now automatically granted; please pay special attention to the **implications** paragraph below. The Copyright Subcommittee of the Joint Board/Council Committees on Publications approved the following:

Copyright permission for published and submitted material from theses and dissertations
ACS extends blanket permission to students to include in their theses and dissertations their own articles, or portions thereof, that have been published in ACS journals or submitted to ACS journals for publication, provided that the ACS copyright credit line is noted on the appropriate page(s).

Publishing **implications** of electronic publication of theses and dissertation material
Students and their mentors should be aware that posting of theses and dissertation material on the Web prior to submission of material from that thesis or dissertation to an ACS journal may affect publication in that journal. Whether Web posting is considered prior publication may be evaluated on a case-by-case basis by the journal's editor. If an ACS journal editor considers Web posting to be "prior publication", the paper will not be accepted for publication in that journal. If you intend to submit your unpublished paper to ACS for publication, check with the appropriate editor prior to posting your manuscript electronically.

**Reuse/Republication of the Entire Work in Theses or Collections**: Authors may reuse all or part of the Submitted, Accepted or Published Work in a thesis or dissertation that the author writes and is required to submit to satisfy the criteria of degree-granting institutions. Such reuse is permitted subject to the ACS' "Ethical Guidelines to Publication of Chemical Research" (http://pubs.acs.org/page/policy/ethics/index.html); the author should secure written confirmation (via letter or email) from the respective ACS journal editor(s) to avoid potential conflicts with journal prior publication*/embargo policies. Appropriate citation of the Published Work must be made. If the thesis or dissertation to be published is in electronic format, a direct link to the Published Work must also be included using the ACS Articles on Request author-directed link − see http://pubs.acs.org/page/policy/articlesonrequest/index.html

* Prior publication policies of ACS journals are posted on the ACS website at
http://pubs.acs.org/page/policy/prior/index.html

If your paper has **not** yet been published by ACS, please print the following credit line on the first page of your article: "Reproduced (or 'Reproduced in part') with permission from [JOURNAL NAME], in press (or 'submitted for publication'). Unpublished work copyright [CURRENT YEAR] American Chemical Society." Include appropriate information.

If your paper has already been published by ACS and you want to include the text or portions of the text in your thesis/dissertation, please print the ACS copyright credit line on the first page of your article: "Reproduced (or 'Reproduced in part') with permission from [FULL REFERENCE CITATION.] Copyright [YEAR] American Chemical Society." Include appropriate information.

**Submission to a Dissertation Distributor**: If you plan to submit your thesis to UMI or to another dissertation distributor, you should not include the unpublished ACS paper in your thesis if the thesis will be disseminated electronically, until ACS has published your paper. After publication of the paper by ACS, you may release the entire thesis (**not the individual ACS article by itself**) for electronic dissemination through the distributor; ACS's copyright credit line should be printed on the first page of the ACS paper.

10/10/03, 01/15/04, 06/07/06, 04/07/10, 08/24/10, 02/28/11

## A.3 IOP Publishing Limited (Approval for Chapter 2)

Ref: : CM/428020/PAP/184936

### Assignment of copyright - IOP Publishing Limited

1. IOP Publishing Limited ("IOP") agrees to publish:

**Manuscript Title:** Magnetic and transport properties of single crystal LnRu2Al10 (Ln = Pr, Gd, Yb) ("**the Article**") written by

**Names of all Authors:** Gregory W Morrison, Neel Haldolaarachchige, D P Young, Julia Y Chan ("**the Named Authors**")

in the following journal: Journal of Physics: Condensed Matter ("**the Journal**")

2. Transfer of Copyright Agreement

2.1 On acceptance for publication the undersigned author(s) ("Author") of the Article assigns exclusively to IOP worldwide copyright in the Article for the full term and for all media and formats in all material published as part of the Article, which expression includes but is not limited to the text, abstract, tables, figures, graphs, video abstracts and other multimedia content but excludes any other item referred to as supplementary material.

2.2 If any of the Named Authors are Government employees, on acceptance for publication the Author shall grant IOP a royalty free exclusive licence for the full term of copyright for all media and formats to do in relation to the Article all acts restricted by copyright worldwide.

2.3 On acceptance for publication the Author shall grant IOP a royalty free non-exclusive licence for the full term of copyright for all media and formats to do in relation to any supplementary material deemed to be part of the Article all acts restricted by copyright worldwide.

3. Author Rights

3.1 IOP grants the Named Authors the rights specified in 3.2 and 3.3. All such rights must be exercised for non-commercial purposes, if possible should display citation information and IOP's copyright notice, and for electronic use best efforts must be made to include a link to the on-line abstract in the Journal. Exercise of the rights in 3.3 additionally must not use the final published IOP format but the Named Author's own format (which may include amendments made following peer review).

3.2 The rights are:

3.2.1 To make copies of the Article (all or part) for teaching purposes;

3.2.2 To include the Article (all or part) in a research thesis or dissertation;

3.2.3 To make oral presentation of the Article (all or part) and to include a summary and/or highlights of it in papers distributed at such presentations or in conference proceedings; and

3.2.4 All proprietary rights other than copyright.

3.3 The additional rights are to:

3.3.1 Use the Article (all or part) without modification in personal compilations or publications of a Named Author's own works (provided not created by third party publisher);

3.3.2 Include the Article (all or part) on a Named Author's own personal web site;

3.3.3 Include the Article (all or part) on web sites of the institution (including its repository) where a Named Author worked when research for the Article was carried out; and

3.3.4 No sooner than 12 months after publication to include the Article (all or part) on third party web sites including e-print servers, but not on other publisher's web sites.

**Signature**

In signing this Agreement the Author represents and warrants that the Article is the original work of the Named Authors, it has not been published previously in any form (other than as permitted under clause 3.2.2 which fact has been notified to IOP Publishing Ltd in writing), all Named Authors have participated sufficiently in the conception and writing of the Article, have received the final version of the Article, agree to its submission and take responsibility for it, and submission has been approved as necessary by the authorities at the establishment where the research was carried out.

The Author warrants that he/she signs this Agreement as authorised agent for all Named Authors and has the full power to enter into this Agreement and to make the grants it contains, that the Article has not been and will not be submitted to another publisher prior to withdrawal or rejection, it does not infringe any third party rights, it contains nothing libellous or unlawful, all factual statements are to the best of the Author's knowledge true or based on valid research conducted according to accepted norms, and all required permissions have been obtained in writing.

All Named Authors assert their moral rights.

**Author's signature**.....Julia Chan..... **Date**.....4/11/2012.....

**Signature on behalf of Institution**.....**Date**.....

**Note that if the Article was prepared as part of a Named Author's duties for their institution this Agreement must be signed by their institution as Author. Further, if there are several Named Authors it should be signed by one author in a representative capacity. If all Named Authors are employees of the US Government and the Article was prepared as part of their duties the Article is not eligible for copyright and one of the Named Authors should sign below to confirm this fact. If at least one of the Named Authors is not a US Government employee the above should be signed.**

I .....Julia Chan..... **(print name**.....Julia Chan.....**)** **confirm that all Named Authors are employees of the US Government and the Article was prepared as part of their duties and consequently the Article is not eligible for copyright.**

**Please return ALL of this form as soon as possible to IOP Publishing Ltd, Temple Circus, Temple Way, BRISTOL BS1 6BE, UK. (Journal fax: +44 (0) 117 9200661)**

## A.4 American Physical Society (Approval for Chapter 7)

Dear Mr. Morrison,

As the author of the APS paper, you have the right to use figures, tables, graphs, etc. in subsequent publications using files prepared and formatted by you or the APS-prepared versions. The appropriate bibliographic citation must be included.

Best wishes,

Jamie Casey
Circulation and Fulfillment Assistant
American Physical Society
http://librarians.aps.org/

**Vita**

Gregory Morrison grew up in Tillson, NY and graduated as valedictorian from Kingston High School in June 2005. During this time, he was a member of the Boy Scouts of America, where he earned the rank of Eagle Scout, and became a member of the Catskill 3500 Club, an organization for people who have hiked all 35 Catskill Mountains which are taller than 3,500 feet.

Gregory graduated with a Bachelor's of Science in chemistry from the University at Buffalo in May 2009. During his time at UB, he worked as a resident advisor in Roosevelt Hall and was an active member of the Governors' Hall Council and the Resident Hall Association.

In the Fall of 2009, Gregory entered Graduate School at Louisiana State University, where he worked under Prof. Julia Y. Chan. He will be receiving his Doctor of Philosophy in August 2013.